

NET ECOSYSTEM CARBON BALANCE OF A HETEROGENEOUS  
POLYGONAL TUNDRA LANDSCAPE IN THE LENA RIVER  
DELTA, RUSSIA

Dissertation  
with the aim of achieving a doctoral degree  
at the Faculty of Mathematics, Informatics, and Natural Sciences  
Department of Earth Sciences  
at Universität Hamburg

submitted by  
LUTZ BECKEBANZE

Hamburg, 2022

DEPARTMENT OF EARTH SCIENCES

Date of Oral Defense: 17. February 2023

Reviewers: Prof. Dr. Lars Kutzbach  
Dr. David Holl

Members of the examination commission: Prof. Dr. Lars Kutzbach (Chair)  
Dr. David Holl  
Prof. Dr. Felix Ament  
Prof. Dr. Philipp Porada  
Prof. i.R. Dr. Eva-Maria Pfeiffer

Chair of the Subject Doctoral Committee  
Earth System Sciences: Prof. Dr. Hermann Held  
Dean of Faculty MIN: Prof. Dr.-Ing. Norbert Ritter

## EIDESSTATTLICHE VERSICHERUNG

---

Hiermit erkläre ich an Eides statt, dass ich die vorliegende Dissertationsschrift selbst verfasst und keine anderen als die angegebenen Quellen und Hilfsmittel benutzt habe.

*Hamburg, den 25. November 2022*



---

Lutz Beckebanze





Artistic interpretation of this thesis made by my niece Louisa Kruseman (4 years old). It represents the polygonal tundra with the eddy covariance tower (small red line). Two lemmings (orange) as well as a fox (red) roam around in the tundra. The fox' favorite food is also shown in the bottom right corner — a fried egg with cucumber.



## ABSTRACT

---

Arctic permafrost landscapes contain substantial amounts of soil organic carbon that is potentially subject to decomposition. Warming climates likely accelerate this decomposition in permafrost regions. However, future soil organic carbon decomposition projections still remain uncertain due to limited process understanding and few observation data. This uncertainty in future projections is also the case for the polygonal tundra, a permafrost landscape in the Arctic with complex land–atmosphere carbon (C) flux processes due to the high spatial variability of the landscape components. Although these land–atmosphere C fluxes have been observed on the landscape-level, observations of C fluxes from different landscape components (such as open water and vegetated areas) of the polygonal tundra remain scarce.

In this thesis, I investigate vertical and lateral C flux dynamics in a polygonal tundra site in the Lena River Delta, Russia. First, I present two methodological approaches for source-partitioning the vertical landscape C flux of the heterogeneous polygonal tundra site into the C flux from two landscape components. For these approaches, I used observational data from one, respectively two eddy covariance towers. The results suggested that the source-partitioning approaches effectively separated the C fluxes from the landscape components, namely waterbodies and vegetated tundra. However, the uncertainty of source-partitioning increased drastically when two landscape components shared multiple characteristics (e.g., vegetation and elevation, such as dry and wet tundra) because classifying these similar landscape components with high precision is challenging.

Second, I investigate the relationship between lateral and vertical C fluxes from the polygonal tundra study site and combine the flux components to the net ecosystem carbon balance (NECB). This analysis identified the C flux most relevant to the ecosystem's C balance in the polygonal tundra. To estimate the vertical C flux, I used the eddy covariance method, while I used discharge observations combined with aquatic C concentration to estimate the lateral C flux. The results showed that lateral C export represented about 2 % of the net ecosystem exchange (NEE) of carbon dioxide (CO<sub>2</sub>). I also analyzed the resulting C fluxes from different landscape components using the source-partitioning approaches and determined the effect of waterbody C emission on the landscape C balance. These results from one source-partitioning approach suggested that the estimated summer net CO<sub>2</sub> uptake of the vegetated polygonal tundra was 11 % lower when the waterbody C emission was considered.

This thesis highlights the significance of representative C flux observation in the heterogeneous polygonal tundra since a non-representative C flux observation could lead to a biased C balance. It also shows that vertical C fluxes represent the most relevant C fluxes of the NECB in this landscape.

## ZUSAMMENFASSUNG

---

Arktische Permafrostlandschaften enthalten beträchtliche Mengen an organischem Kohlenstoff (C) im Boden, der potenziell abgebaut werden kann. Durch die Erwärmung des Klimas wird dieser Abbau in Permafrostregionen wahrscheinlich beschleunigt, doch die Prognosen für den künftigen Abbau des organischen Kohlenstoffs im Boden sind aufgrund des begrenzten Verständnisses der Prozesse und der wenigen Beobachtungsdaten nach wie vor unsicher. Diese Ungewissheit in Bezug auf künftige Prognosen gilt auch für die polygonale Tundra, eine Permafrostlandschaft in der Arktis, die aufgrund der großen räumlichen Variabilität der Landschaftskomponenten komplexe Land-Atmosphären-Kohlenstoffflüsse aufweist. Obwohl diese Land-Atmosphäre-Kohlenstoffflüsse auf Landschaftsebene beobachtet wurden, gibt es nur wenige Beobachtungen von Kohlenstoffflüssen aus verschiedenen Landschaftskomponenten (z. B. offene Gewässer und bewachsene Flächen) der polygonalen Tundra.

In dieser Arbeit untersuche ich die vertikale und laterale C-Flussdynamik in einem polygonalen Tundragebiet im Lena-Flussdelta, Russland. Im ersten Teil stelle ich zwei methodische Ansätze zur Aufteilung des vertikalen Landschafts-C-Flusses der heterogenen polygonalen Tundra in den C-Fluss aus zwei Landschaftskomponenten vor. Für diese Ansätze habe ich Beobachtungsdaten von einem bzw. zwei Eddy-Kovarianz-Türmen verwendet. Die Ergebnisse deuten darauf hin, dass die Ansätze zur Quellenaufteilung die C-Flüsse aus den Landschaftskomponenten, d. h. den Gewässern und der bewachsenen Tundra, wirksam trennen. Die Unsicherheit der Quellenaufteilung nahm jedoch drastisch zu, wenn zwei Landschaftskomponenten mehrere Merkmale gemeinsam hatten (z. B. Vegetation und Höhe, wie trockene und feuchte Tundra), da die Klassifizierung dieser ähnlichen Landschaftskomponenten mit hoher Präzision schwierig ist.

Im zweiten Teil untersuchte ich die Beziehung zwischen lateralen und vertikalen C-Flüssen aus dem polygonalen Tundra-Studienggebiet und kombinierte die Flusskomponenten zur Netto-Ökosystem-Kohlenstoffbilanz (NECB). Durch diese Analyse konnte ich den C-Fluss identifizieren, der für die C-Bilanz des Ökosystems in der polygonalen Tundra am wichtigsten ist. Zur Schätzung des vertikalen C-Flusses verwendete ich die Eddy-Kovarianz-Methode, während ich zur Schätzung des

lateralen C-Flusses Abflussbeobachtungen in Kombination mit der C-Konzentration im Abflusswasser verwendete. Die Ergebnisse zeigten, dass der laterale C-Export etwa 2% des Netto-Ökosystemaustauschs (NEE) von Kohlenstoffdioxid (CO<sub>2</sub>) ausmacht. Außerdem analysierte ich die sich ergebenden C-Flüsse aus den verschiedenen Landschaftskomponenten unter Verwendung von Ansätzen zur Quellenaufteilung und ermittelte die Auswirkung der C-Emissionen der Wasserkörper auf die C-Bilanz der Landschaft. Die Ergebnisse eines Quellenaufteilungsansatzes ergaben, dass die geschätzte sommerliche Netto-CO<sub>2</sub>-Aufnahme der bewachsenen polygonalen Tundra um 11% niedriger war, wenn die C-Emissionen der Gewässer berücksichtigt wurden.

Diese Arbeit unterstreicht die Bedeutung einer repräsentativen C-Fluss-Beobachtung in der heterogenen polygonalen Tundra, da eine nicht repräsentative C-Fluss-Beobachtung zu einer verzerrten C-Bilanz führen könnte. Sie zeigt auch, dass die vertikalen C-Flüsse die wichtigsten C-Flüsse der NECB in dieser Landschaft darstellen.



## PUBLICATIONS RELATED TO THIS DISSERTATION

---

### Appendix A:

Beckebanze, L., Runkle, B. R. K., Walz, J., Wille, C., Holl, D., Helbig, M., Boike, J., Sachs, T., and Kutzbach, L. (2022). Lateral carbon export has low impact on the net ecosystem carbon balance of a polygonal tundra catchment. In *Biogeosciences*, 19(16), 3863-3876. DOI: [10.5194/bg-19-3863-2022](https://doi.org/10.5194/bg-19-3863-2022)

Authors contribution: BRKR, CW, and LK designed the experiments, and BRKR, CW, DH, and LK carried out the fieldwork. BRKR, JW, LB, and LK developed the idea for the analysis, and CW provided processed eddy covariance data. The formal analysis and data visualization were done by LB. DH and LK supervised this. LK, JB, and TS provided resources for the instrumentation. LB prepared the manuscript with contributions from all co-authors.

### Appendix B:

Beckebanze, L.\*, Rehder, Z.\*, Holl, D., Wille, C., Mirbach, C., and Kutzbach, L. (2022). Ignoring carbon emissions from thermokarst ponds results in overestimation of tundra net carbon uptake. In *Biogeosciences*, 19(4), 1225-1244. DOI: [10.5194/bg-19-1225-2022](https://doi.org/10.5194/bg-19-1225-2022)

\*These authors contributed equally to this work.

Authors contribution: ZR and LK designed the experiments; ZR and LB carried out the fieldwork. ZR, LB, and LK developed the idea for the analysis, and CW and LB prepared the data. The formal analysis and data visualization were performed by LB and ZR with supervision by DH and LK. Resources (land-cover classification) have been provided by CM. LB and ZR prepared the manuscript with contributions from all co-authors.

### Appendix C:

Beckebanze, L., Rehder, Z., Holl, D., and Kutzbach, L. (2022). Partitioning carbon fluxes from a landscape with small scale heterogeneity using parallel observations from two eddy covariance towers. Manuscript in preparation.

Authors contribution: ZR and LK designed the experiments; ZR and LB carried out the fieldwork. LB, DH, and LK developed the idea for the analysis, and LB prepared the data. The formal analysis and data visualization were performed by LB with supervision by DH and LK. LB prepared the manuscript with contributions from all co-authors.



## ACKNOWLEDGMENTS

---

It was November 2014, a young bachelor student knocked on the office door of Prof. Lars Kutzbach and asked if he could join an expedition to the Siberian Arctic — that’s how my journey in this working group started. Eight years, six expeditions, and three theses later, a great journey comes to an end. First, thank you, Lars, for giving me the great opportunity to research in the Arctic and being a very motivating and helpful supervisor, especially during my less motivated times during my PhD. A great thank you also goes to David for being my second supervisor. You helped me so much with programming and especially writing. Your support was a crucial part of my PhD. A big thanks to Norman for your remote support with the eddy covariance tower on Samoylov island and for all the useful discussion on the balcony.

The two published papers in this thesis were only possible with the co-authors. Many thanks to all of them! A special thank goes to Zoé — it was a great pleasure working with you. Answering and solving all the difficult reviewers’ comments with you was even fun!

Going on an expedition to the Siberian Arctic was not always easy, but always fun! A great thanks to all colleagues involved in the expeditions, especially the colleagues from AWI and GfZ Potsdam and all Russian partners in St Petersburg. Also, thank you to the station crew on Samoylov island and Stepan for guiding me through Tiksi.

I also want to thank the SICSS office for supporting me during my PhD and Sarah for being a great panel chair!

I also want to thank all the other PhDs in the institute and in SICSS who made my PhD phase much more enjoyable. Especially, I want to thank Leo for becoming such a great friend during the PhD. I’m very grateful for meeting you. I’m so happy we went through this together in 506. Next time I will manage to get you to Siberia, I promise! Also, thank you, Fay and Leo, for being my office mates. It was a lot of fun with you. And I also want to thank all the other people who have been on the fifth floor throughout the last years for going for lunch together and for all the useful balcony discussions (most already mentioned above, but also Olli, Jamil, and Janina).

A special thank goes to the Schlump-gang for being such a great support, especially during the lockdowns. Thank you, Andi, for distracting me from work with all our coffee breaks and bike rides! I also want to thank Luisa for the helpful discussion on possible future career paths, mostly on the phone and sometimes in Bremen. Thanks also to my Ultimate Frisbee team for being such a fun group and all my flatmates throughout the last three years for being a great sup-

port. And also, thanks a lot to that one person I most likely forgot to mention!

Last but not least, I would like to thank my family for being there for me! I clearly would not have made it through the PhD without you!

## CONTENTS

---

1	Introduction	1
1.1	Background	3
1.1.1	Permafrost-affected Soils	3
1.1.2	Permafrost carbon feedback	4
1.1.3	Carbon fluxes	5
1.2	The Study Site	7
1.2.1	The Lena River Delta	7
1.3	Measurement technique	8
1.3.1	Eddy Covariance	8
2	Results and discussion	11
2.1	Source-partitioning of CO <sub>2</sub> fluxes using the eddy covariance method	11
2.1.1	Approach using one eddy covariance tower	12
2.1.2	Approach using two eddy covariance towers	13
2.2	Where does the carbon go? The net ecosystem carbon balance of a polygonal tundra landscape	14
3	Conclusion and outlook	17
3.1	Take Home Messages	19
I	Appendix	
A	Lateral carbon export has low impact on the net ecosystem carbon balance of a polygonal tundra catchment	23
A.1	Abstract	23
A.2	Introduction	24
A.3	Methods	26
A.3.1	Study site	26
A.3.2	Catchment characteristics	26
A.3.3	Water discharge	26
A.3.4	Dissolved inorganic carbon (DIC)	27
A.3.5	Dissolved organic carbon (DOC)	28
A.3.6	DOC and DIC flux	28
A.3.7	Environmental conditions	29
A.3.8	Eddy covariance flux	29
A.3.9	Cumulative fluxes	29
A.3.10	Uncertainty estimation	29
A.4	Results	31
A.4.1	Environmental conditions	31
A.4.2	Lateral carbon flux dynamics	33
A.4.3	Net ecosystem carbon balance	33
A.5	Discussion	34
A.5.1	Comparison of DOC and DIC dynamics	34
A.5.2	Net ecosystem carbon balance	35

A.6	Conclusions	40
A.7	Appendix	40
	A.7.1 DOC concentration from a spectrometer probe	40
A.8	Manuscript information	44
B	Ignoring carbon emissions from thermokarst ponds results in overestimation of tundra net carbon uptake	47
B.1	Abstract	47
B.2	Introduction	48
B.3	Methods	50
	B.3.1 Study site	50
	B.3.2 Instruments	50
	B.3.3 Data processing	52
	B.3.4 Data analysis	53
B.4	Results	58
	B.4.1 Meteorological conditions	58
	B.4.2 CO <sub>2</sub> fluxes	58
	B.4.3 CH <sub>4</sub> fluxes	59
	B.4.4 Upscaled CO <sub>2</sub> flux	61
B.5	Discussion	63
	B.5.1 CO <sub>2</sub> flux	63
	B.5.2 CH <sub>4</sub> flux	66
B.6	Upscaling the CO <sub>2</sub> flux	69
B.7	Conclusions	70
B.8	Appendix	71
B.9	Manuscript information	75
C	Partitioning carbon fluxes from a landscape with small scale heterogeneity using parallel observations from two eddy covariance towers	77
C.1	Abstract	77
C.2	Introduction	78
C.3	Methods	79
	C.3.1 Study site and instruments	79
	C.3.2 Data Analysis	80
C.4	Results and Discussion	83
	Bibliography	89

## ACRONYMS

---

C	Carbon
CO <sub>2</sub>	Carbon dioxide
CH <sub>4</sub>	Methane
DIC	Dissolved inorganic carbon
DOC	Dissolved organic carbon
EC	Eddy Covariance
GHG	Greenhouse gas
GPP	Gross primary production
H <sub>2</sub> O	Water
NECB	Net ecosystem carbon balance
NEE	Net ecosystem exchange
PAR	Photosynthetically active radiation
R <sub>eco</sub>	Ecosystem respiration
RCP	Representative concentration pathway
SOC	Soil organic carbon



## INTRODUCTION

---

Climate change, including globally rising air temperatures, has been caused by human activity, mostly through the emission of greenhouse gases (GHGs; IPCC 2021). These GHGs, such as carbon dioxide (CO<sub>2</sub>) and methane (CH<sub>4</sub>), increase the natural greenhouse effect of the atmosphere and thus increase the average near-surface air temperature. Besides anthropogenic GHG emissions, natural processes of ecosystem respiration and photosynthesis play important roles in exchanging GHGs between the earth's surface and the atmosphere. Furthermore, ecosystem's responses to climate change can increase the GHG concentration in the atmosphere due to the mineralization of carbon (C) stored in soils, especially in wetlands and permafrost soils (IPCC, 2021).

Specifically, Arctic permafrost regions have historically acted as sinks for atmospheric C, accumulating a soil organic carbon (SOC) content of  $1014_{-175}^{+194}$  Pg in the upper 3 meters of the soil (Mishra et al., 2021). As global air temperatures continue to rise, permafrost soils will increasingly thaw, and part of the SOC will likely decompose aerobically or anaerobically. This decomposition will lead to the production of CO<sub>2</sub> and CH<sub>4</sub>, respectively, contributing to a greater greenhouse effect and, thereby, continued warming. However, the extent of this permafrost C feedback remains uncertain and depends, among other factors, on future global warming (Meredith et al., 2019). These uncertainties regarding future GHG emissions are partially due to limited observational data and process understanding of the permafrost C feedback (Schuur et al., 2015).

The permafrost regions, especially the polygonal tundra, feature high spatial variability with different landscape components, such as dry tundra, wet tundra, and open water. These landscape components show significantly different land-atmosphere C flux dynamics (Eckhardt et al., 2019; Kuhn et al., 2018; Lara et al., 2020; de Aro Galera et al., 2022). For example, whether the landscape of the tundra will become drier or wetter or will feature more ponds due to changing climate is a matter of research. The enhanced evaporation of a warmer climate and ice-wedge degradation in the polygonal tundra could lead to a drier tundra landscape (Nitzbon et al., 2019; Zhang et al., 2018). In contrast, abrupt thaw could also expand open water areas (Magnússon et al., 2021). The latest projections suggest that CH<sub>4</sub> emission would rise under a dry arctic scenario (Vrese et al., 2022). Therefore, a change in the distribution of landscape components would likely cause a change in the land-atmosphere fluxes of that landscape. Hence,

*Relevance of  
permafrost research*

observing and analyzing land-atmosphere fluxes from different landscape components of the tundra is important, especially regarding observation data with high temporal resolution (Vonk et al., 2015). To improve the understanding of land-atmosphere C fluxes in the spatially heterogeneous polygonal tundra landscape, I present and analyze observational data for vertical and lateral C fluxes from different landscape components in this thesis using the eddy covariance (EC) method and hydrological catchment observations.

The study site for this thesis is located in the Lena River delta and is covered by polygonal tundra, a common landscape type in Arctic permafrost regions. Within the polygonal tundra, long-term growth of under-ground ice wedges due to thermal contraction and expansion causes a micro-topography of a few decimeters and a polygonal pattern (Kutzbach et al., 2007). The micro-topography results in a small-scale variability of landscape components within a few meters with dry and wet areas (covered with low vegetation), ponds, and lakes. The polygonal tundra represents an important C reservoir with an estimated C stock in the Lena River delta of  $29 \pm 10 \text{ kg m}^{-2}$  in the upper 1 meter (Zubrzycki et al., 2014). The vertical C fluxes from the polygonal tundra landscape show a high spatial variability; Eckhardt et al. (2019) showed that wet tundra has a higher net  $\text{CO}_2$  uptake compared to dry tundra during the growing season. Furthermore,  $\text{CH}_4$  emissions also represent an important C flux in the polygonal tundra landscape.  $\text{CH}_4$  can be produced under oxygen-deficient conditions in water-saturated soils, from which it emits to the atmosphere through diffusion, ebullition, or plant-mediated transport (Knoblauch et al., 2015; Walter Anthony and Anthony, 2013). Previous research at the study site has shown that half-hourly landscape  $\text{CH}_4$  fluxes depended on the soil temperature and near-surface turbulence (Rößger et al., 2022; Wille et al., 2008). Moreover, the surface  $\text{CH}_4$  concentrations from small ponds in this area show a high spatial variability (Rehder et al., 2021), which likely results in spatially heterogeneous aquatic  $\text{CH}_4$  emissions.

The lateral C flux represents another potentially relevant C flux component of the ecosystem's C balance. In two subarctic catchments in northern Sweden, lateral C fluxes represented 4–35% of the net ecosystem carbon balance (NECB; Chi et al. 2020; Lundin et al. 2016; Öquist et al. 2014). However, a comparison of lateral and vertical C fluxes and the extent to which they compose the NECB has not yet been performed in an Arctic landscape.

To study the vertical fluxes of  $\text{CO}_2$  and  $\text{CH}_4$  from the polygonal tundra, I used observations from two EC towers, both located on Samoylov island in the Lena River delta, Russia. Additionally, hydrological observations of water C content and water runoff rate were performed to address questions related to lateral C export. The observations of vertical C fluxes using the EC instruments were conducted

between June and September 2014 and July and September 2019, respectively, while lateral C fluxes were observed between June and September 2014.

*Research questions*

In the first section of this thesis, I present and discuss methodological approaches for partitioning C fluxes from a heterogeneous polygonal tundra landscape into the landscape components' C fluxes using the EC method. I show two different approaches, the first with a single EC observation tower and the second with two parallel, nearby EC towers. In the second section, I summarize the findings of this thesis regarding the NECB of the polygonal tundra landscape and aim to answer the question: where does the carbon go? I present C fluxes from different landscape components, namely open water and semi-terrestrial tundra, and discuss the implications of these findings for up-scaling approaches. I also present lateral C flux observations, compare the resulting lateral C fluxes to vertical C flux observations, and discuss the relevance of lateral C fluxes to the ecosystem's C balance.

## 1.1 BACKGROUND

### 1.1.1 Permafrost-affected Soils

Permafrost soils exist in the cold regions of the world, namely the Arctic, alpine regions, and partially Antarctica. Over previous millennia, the cold temperatures of winter cooled the ground in these regions more than the warm temperatures in summer heated it. While *permafrost* suggests that this soil is permanently frozen, it neither needs to be frozen nor permanently remains below 0 °C (Van Huissteden, 2020). By definition, permafrost is ground at or below 0 °C for at least two consecutive years (Harris et al., 1988). Soils containing water can remain unfrozen at sub-zero temperatures, for example, when salts are solved in the pore water.

*Definition of permafrost*

Permafrost occurs mostly in the Northern Hemisphere, covering about 15% of the hemisphere's land area (Obu 2021; see Fig. 1). In Russia, the permafrost regions reach from the Siberian Arctic far south into China and Mongolia. However, in western Russia and the European continent, permafrost only occurs north of ~60° and in alpine regions. This lack of permafrost in the northern European continent is partially due to the presence of glaciers during the last glaciation (Clark et al., 2009). These glaciers prevented the cold temperatures during winter from reaching the ground and thus insulated the ground.

*Introducing the active layer*

In permafrost regions, not the entire ground is always frozen. A top layer above the permafrost table, called the *active layer*, thaws in summer. This layer can have a depth of a few centimeters in the cold climate of the high Arctic to tens of meters in the southern part of the Russian permafrost regions. Air and surface temperature play

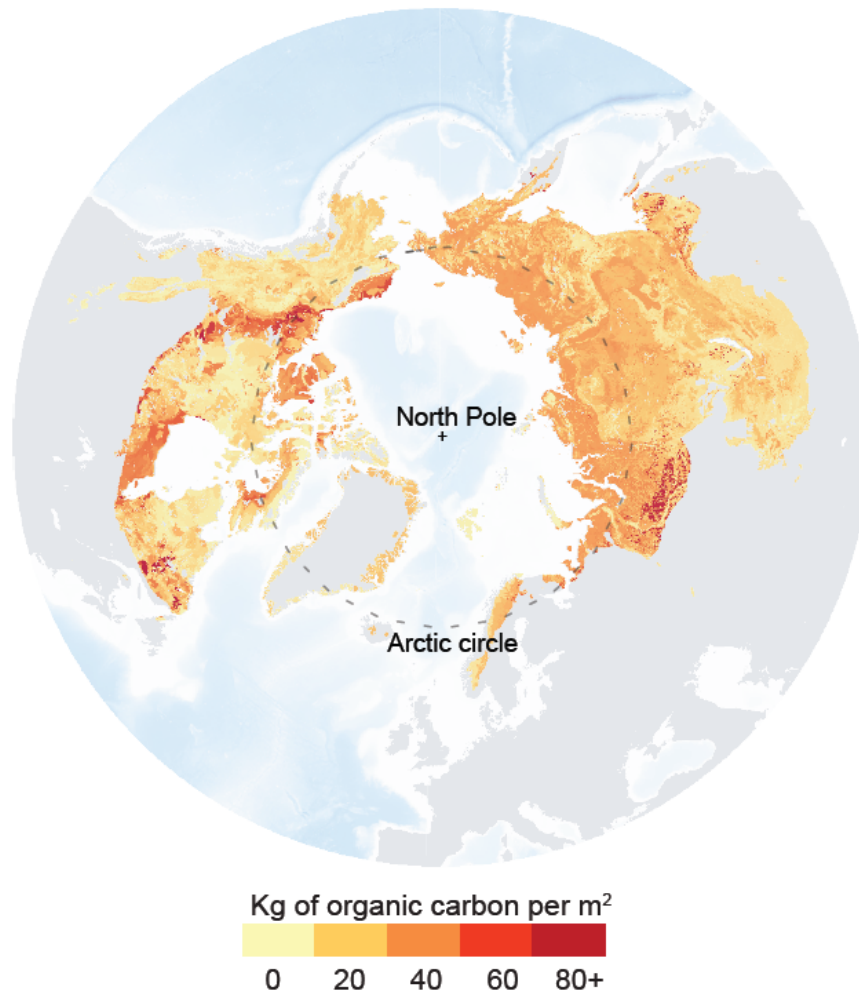


Figure 1: Area of permafrost regions in the Northern Hemisphere with the C content in the upper 3 meters. Figure from Canadell et al. (2021, p. 774).

important roles in the active layer depths, as well as other factors, including soil moisture, soil structure, vegetation, and snow cover. These factors influence the thermal transfer properties of the soil. For example, an intact moss cover insulates the soil, limiting temperature fluctuations from affecting deeper ground layers (Van Huissteden, 2020).

#### 1.1.2 Permafrost carbon feedback

Mishra et al. (2021) estimated the SOC to be  $1014_{-175}^{+194}$  Pg<sup>1</sup> in the upper 3 meters of the Northern Hemisphere permafrost region. In a warming climate, microbial decomposition processes are likely to intensify, and deeper soil layers will likely thaw, leading to a potential acceleration of GHG emissions from the permafrost. Alternately, higher temperatures

*The current state of permafrost carbon*

<sup>1</sup> 1 Pg  $\hat{=}$   $10^{15}$  g

could enhance vegetation productivity in the Arctic regions, thereby potentially enhancing plants' C uptake during the growing season (Mekonnen et al., 2021).

According to the sixth assessment report by the intergovernmental panel on climate change (IPCC), the temperature increase due to GHG emissions from permafrost regions will be “enough to be important, but not enough to lead to a ‘runaway warming’ situation, where permafrost thaw leads to a dramatic, self-reinforcing acceleration of global warming” (Canadell et al., 2021). In a special report regarding the ocean and cryosphere in a changing climate, the authors state a *high confidence* that the “thaw depth will increase and the areal extent of near-surface permafrost will decrease substantially” (Meredith et al., 2019). However, the magnitude of this near-surface permafrost loss ranges widely, from 2–66 % for representative concentration pathway (RCP) 2.6 to 30–99 % for RCP 8.5. Thawing permafrost can also partially mobilize the organic C in the permafrost regions. The latest projection stated a permafrost CO<sub>2</sub> feedback of 18 (3.1–41) PgC °C<sup>-1</sup> and a permafrost CH<sub>4</sub> feedback of 2.8 (0.78–7.3) PgC<sub>eq</sub> °C<sup>-1</sup> (Canadell et al., 2021). The estimations for the accumulated permafrost C loss until the year 2100 range from 37–174 PgC for RCP 8.5 with a model ensemble average of 92 ± 17 PgC. For RCP 2.6, an accumulated permafrost C loss of 28–92 PgC is projected until 2100 (Canadell et al., 2021).

For comparison, the cumulative annual global fossil fuel CO<sub>2</sub> emission in 2021 was 10.1 ± 0.5 PgC (Friedlingstein et al., 2022). Therefore, the accumulated permafrost C loss until 2100 will account for 3 to 9 times the annual global fossil fuel CO<sub>2</sub> emission from 2021, and the atmosphere may receive a substantial amount of C from the permafrost region, even if CO<sub>2</sub> emission from fossil fuels is eliminated.

### 1.1.3 Carbon fluxes

#### 1.1.3.1 Carbon Dioxide

Net CO<sub>2</sub> flux consists of two major components: (1) the uptake of CO<sub>2</sub> by photosynthesis, also called gross primary production (GPP), and (2) the respiration of CO<sub>2</sub> by the soil and plants called ecosystem respiration (R<sub>eco</sub>). During daytime in a vegetated area, both GPP and R<sub>eco</sub> occur simultaneously. Thus, the observed NEE represents the sum of the two opposing flux components R<sub>eco</sub> and GPP. At nighttime or in low-light situations, photosynthesis stops, and GPP drops to zero. As photosynthetically active radiation (PAR) increases, plants increasingly take up CO<sub>2</sub> until they reach a maximum, at which point increased PAR does not lead to higher CO<sub>2</sub> uptake. This relationship between CO<sub>2</sub> uptake and PAR is commonly used to model and gap-fill the CO<sub>2</sub> uptake (Runkle et al., 2013). However, this simple modeling approach neglects the complexity of photosynthesis. Each

*The future of permafrost carbon*

*Comparison to global CO<sub>2</sub> emission*

*CO<sub>2</sub> flux components*

plant has a plant-specific optimum temperature for photosynthesis, and plants close their stomata in dry air to prevent wilting. Therefore, plants perform less photosynthesis in a meteorological situation with extremely high temperatures or extremely dry air, and the CO<sub>2</sub> flux decreases, even under favorable PAR conditions.

*Ecosystem  
respiration*

Ecosystem respiration consists of two parts: (1) autotrophic respiration and (2) heterotrophic respiration. Autotrophic respiration is the CO<sub>2</sub> emission of living plant components (above ground and roots, Van Huissteden 2020). Heterotrophic respiration is the CO<sub>2</sub> emission of the entire population of organic matter-decomposing bacteria, fungus, and fauna breathing (Van Huissteden, 2020). Although it also depends on other factors, including nutrient availability and the chemical condition of the soil, heterotrophic respiration is mostly temperature-dependent. Therefore, the soil temperature functions as a driver for models of ecosystem respiration used for gap-filling (Holl et al., 2019a; Rößger et al., 2019a; Runkle et al., 2013).

#### 1.1.3.2 Methane

*Relevance of methane*

Methane is a relevant greenhouse gas in the earth's atmosphere with a comparative impact of non-fossil and fossil methane being  $27.0 \pm 11$  and  $29.8 \pm 11$  times greater than CO<sub>2</sub> over 100 years, respectively (Forster et al., 2021). Wetlands act as the largest natural source of methane, while agriculture, waste, and gas production act as the main anthropogenic source of methane (Saunois et al., 2020). The atmosphere represents the main sink of methane due to oxidation (Cicerone and Oremland, 1988; Saunois et al., 2020) leading to net production of atmospheric CO<sub>2</sub> (Boucher et al., 2009). In the soil of wetlands, the production and consumption of methane can occur simultaneously in the same soil column. Production begins in the water-saturated soil layer. There, organic matter is decomposed to methane under anoxic conditions. This methane can reach the surface through three pathways:

*Methane transport  
processes*

- Diffusion: slow transport of methane through air-filled pores of the soil toward the surface
- Ebullition: quick movement of methane-filled bubbles in water-logged soil or water columns
- Plant-mediated transport: quick movement of methane through hollow stems and roots of specific plants from deeper soil layers to the atmosphere

In the slow diffusion process, methane can be oxidized to CO<sub>2</sub> in upper aerobic soil layers. Therefore, strong methane production in deeper soil layers can lead to higher CO<sub>2</sub> emissions. During the quicker transport processes of ebullition and plant-mediated transport, oxidation of methane plays a minor role.

## 1.2 THE STUDY SITE

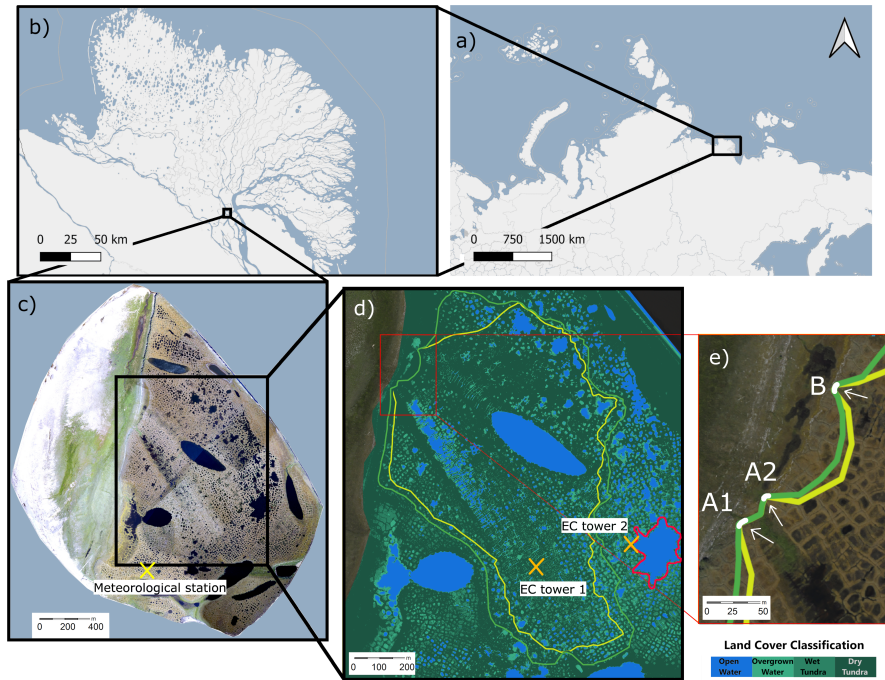
1.2.1 *The Lena River Delta*

Figure 2: Top: map of northern Russia (a) and the Lena River delta (b). Bottom: map of Samoylov Island (c) with the maximum (green) and minimum (yellow) catchment size (studied in chapter A) and the land cover classification by Mirbach et al. (2022) (d). The orange crosses in (d) mark the locations of eddy covariance tower 1 (used in chapters A and C) and tower 2 (used in chapters B and C). In panel (d), the merged polygonal pond studied in chapters B and C is outlined in red. The yellow cross in (c) denotes the location of the meteorological station with the active layer depth observations. Panel (e) shows the locations of outflows A<sub>1</sub>, A<sub>2</sub>, and B studied in chapter A. Map data from © OpenStreetMap contributors 2020, distributed under the Open Data Commons Open Database License (ODbL) v1.0 (a, b) and modified after Boike et al. (2012b) (c, d, e).

With an area of 32,000 km<sup>2</sup>, the Lena River delta is the largest in the Arctic and one of the largest river deltas in the world. The delta consists of more than 1500 islands, separated from each other by smaller and larger river arms (Are and Reimnitz, 2000). The geomorphological classification of the river delta indicates three main river terraces of different ages and a floodplain (Schwamborn et al., 2002). The first terrace, which is also the youngest, was formed in the late Holocene and covers about two-thirds of the river delta along with active floodplains. This terrace is characterized by polygonal tundra and thermokarst lakes (Schwamborn et al., 2002). The second terrace formed between the late Pleistocene and the early Holocene covers about 23% of the

*Classification of the  
Lena River delta*

river delta. It consists of sandy sediment with relatively low ice content (Schneider et al., 2009). The third terrace, the oldest terrace, is a remnant of a late Pleistocene plain. Its sediments are rich in ice and organic material, and the soil of the terrace is characterized by polygonal soils and thermokarst processes (Boike et al., 2013).

In this thesis, I focus on observational data from Samoylov Island, an island in the center of the Lena River delta. My study site on the island includes the first river terrace with polygonal tundra. The polygonal tundra represents a landscape with low vegetation of a few centimeters and a micro-relief with a polygonal structure.

### 1.3 MEASUREMENT TECHNIQUE

#### 1.3.1 *Eddy Covariance*

The EC method is a micrometeorological measurement technique used to estimate land–atmosphere fluxes of momentum, heat, water vapor, and trace gases within the atmospheric boundary layer (ABL). This method allows researchers to observe vertical land-atmosphere fluxes from areas of a few hundred to a few million square meters. Recently, the EC method became the state-of-the-art method for vertical flux observations and networks of flux observations (ICOS, 2022; Pastorello et al., 2020). A typical setup of an EC observation tower is shown in figure 3; data from this EC tower was used in appendices B and C.

Within the ABL, turbulent eddies dominate the vertical transport processes (Lee et al., 2006). The instruments of an EC observation tower measure the parameters of eddies within the ABL, including 3D wind speed, temperature, and the gas concentration of interest, with a high measurement frequency, typically 20 Hz. The high-frequency observation of vertical wind speed and the concentration of the gas of interest represent the most relevant observations for vertical gas flux estimations. When, for example, in time step  $t_1$  a downwind with a relatively low concentration of  $\text{CO}_2$  is observed and a short time later in time step  $t_2$  an upwind with a relatively high concentration of  $\text{CO}_2$  is observed, a net transport of  $\text{CO}_2$  must have occurred from the ground to the atmosphere. In other words, the net vertical land-atmosphere flux can be expressed as the covariance between the vertical velocity of the air and the concentration of the gas of interest.

Calculating the covariance requires post-processing the raw data. Traditionally, this post-processing is performed after the measurement campaign using specific programs or scripts (e.g., EddyPro or EddyRe). However, newer instruments perform the post-processing in the logging device of the EC instruments (e.g., Licor SmartFlux System). During post-processing, numerous corrections are applied to compensate, for example, for pressure fluctuations or instrument-related limitations.

*Principle of the EC  
method*

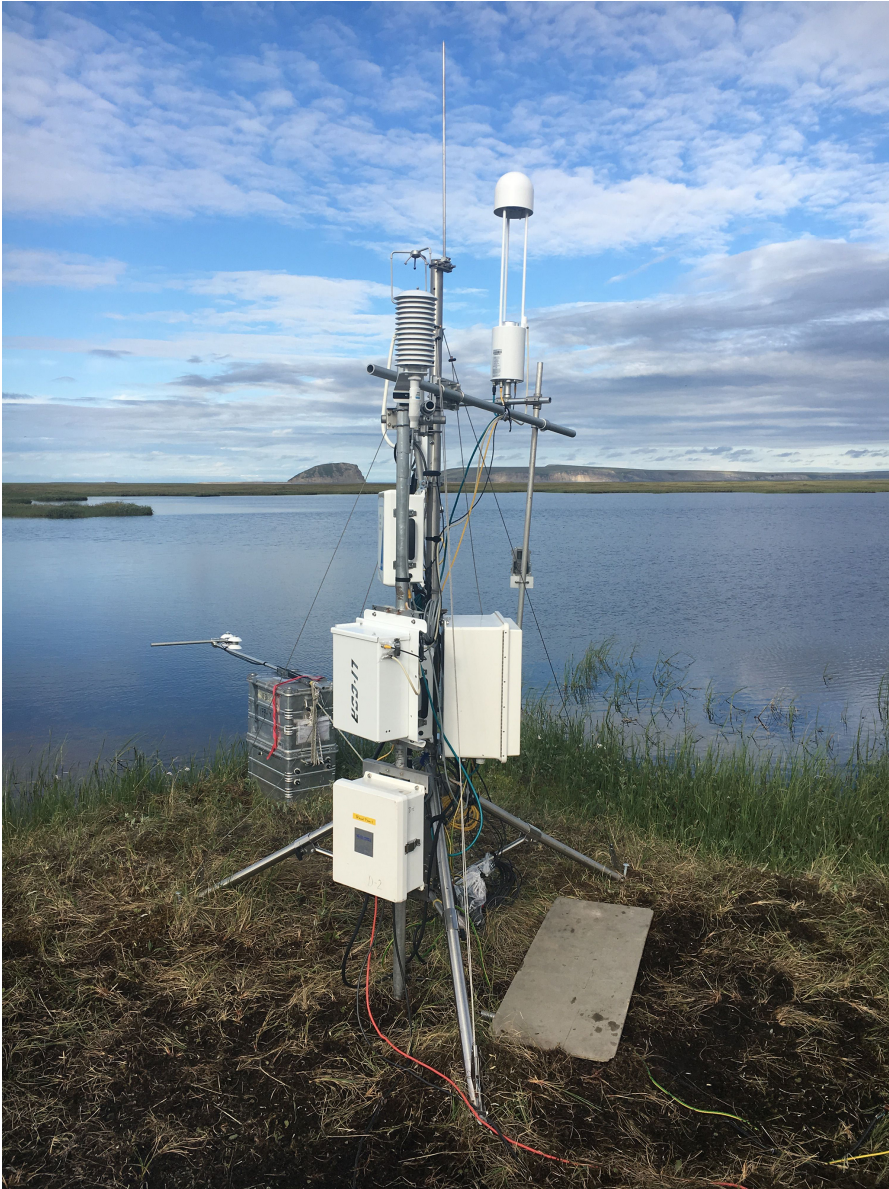


Figure 3: Picture of the eddy covariance tower (*EC Tower 2* in Fig. 2) with the  $\text{CH}_4$  analyzer in the top-right part. The background shows a merged polygonal pond which is outlined in red in Fig. 2. Picture taken on 11 July 2019 by Zoé Rehder.

Further information about the EC method and the theory behind the EC method can be found in Burba (2021) and Lee et al. (2006).



## RESULTS AND DISCUSSION

---

### 2.1 SOURCE-PARTITIONING OF CO<sub>2</sub> FLUXES USING THE EDDY COVARIANCE METHOD

In this thesis, I show two approaches for source-partitioning land-atmosphere CO<sub>2</sub> fluxes into fluxes from different landscape components. Here, I define landscape components as areas within the landscape that share many characteristics (such as moisture content, elevation, and vegetation) and can therefore be grouped into one class. I focus on the landscape of the polygonal tundra, which is characterized by a polygonal structure with a micro-topography of about 50 cm (Kutzbach, 2006). However, this landscape can also differ among locations. Even at the study site on Samoylov island, Kartoziia (2019) defined ten different types of polygonal tundra, including less degraded, low-centered polygons and more degraded, high-centered polygons. Other landcover classifications separate the polygonal tundra surface of Samoylov island into four classes: dry tundra, wet tundra, overgrown water, and open water (Mirbach et al., 2022; Muster et al., 2012).

In the first part of this section, I separate the CO<sub>2</sub> fluxes into fluxes from ponds and those from semi-terrestrial tundra using observational data from one EC tower (*one-tower-approach*). I define ponds as land surface classified as *open water* while semi-terrestrial tundra includes the classes *dry tundra*, *wet tundra* and *overgrown water*. In the second part of this section, I present an alternative method for estimating gas fluxes for the same individual surface classes using observational data from two EC towers in relatively proximity (~500 m) of each other (*two-tower-approach*). Additionally, I further separate semi-terrestrial tundra into the components of dry tundra and wet tundra in this analysis.

To source-partition CO<sub>2</sub> fluxes for both approaches, I used two models and one land cover classification. The first model was the gap-filling model for NEE fluxes of CO<sub>2</sub>, which was proposed by Runkle et al. (2013; from now on referred to as the *bulk-NEE model*). Details about this model can be found in section B.3.4.3. The second model was the footprint model, which was used to estimate the source area of the flux signal observed at the EC tower (Kormann and Meixner, 2001). Each grid cell of this model was combined with the land cover classification to determine the contribution of each land cover component with respect to each 30-minute flux. I refer to the contribution of each land-cover component as the *weighted footprint fraction*. The land-cover

*Definition of  
landscape  
components*

*Methods used in both  
source-partitioning  
approaches*

classification used in the *one-tower-approach* was provided by Mirbach et al. (2022). In the *two-tower-approach*, additionally the land-cover classification by Muster et al. (2012) was utilized. Both land-cover classifications agree in classifying the surface into open water and semi-terrestrial tundra. However, they show substantial differences in classifying the tundra surface into dry and wet tundra. Therefore, I compared the resulting CO<sub>2</sub> fluxes using each land-cover classification. Details on the method used to combine the footprint model with the land cover classifications can be found in B.3.4.2.

### 2.1.1 Approach using one eddy covariance tower

In the *one-tower-approach*, I used data from an EC tower located within the polygonal tundra next to a merged polygonal pond (*EC Tower 2* in Fig. 2). I first estimated a gap-filled dataset of CO<sub>2</sub> fluxes, which were mostly influenced by semi-terrestrial tundra. Second, I combined the *weighted footprint fraction* with the observed CO<sub>2</sub> flux and the previously estimated CO<sub>2</sub> flux dominated by semi-terrestrial tundra. By assuming that the total observed flux was the sum of the fluxes from land-cover types weighted with their respective *weighted footprint fraction*, I could estimate the average pond CO<sub>2</sub> flux. Finally, I use the previously mentioned sum of fluxes to estimate half-hourly CO<sub>2</sub> fluxes from the semi-terrestrial tundra that was not influenced by polygonal ponds. A detailed description of this approach can be found in section B.3.4.4.

*Assumptions in  
one-tower-approach*

This approach included substantial assumptions about CO<sub>2</sub> fluxes in the polygonal tundra. To estimate the CO<sub>2</sub> flux from semi-terrestrial tundra (step 3), I used the median of the pond CO<sub>2</sub> flux, thereby assuming a pond CO<sub>2</sub> flux without a diurnal cycle and large variations. This condition was shown to be true in this specific case after step 2 (see Fig. 14). However, this assumption may be invalid at sites with more varying water CO<sub>2</sub> fluxes (e.g., the water CO<sub>2</sub> flux reported by Jansen et al. 2019). In addition, the *one-tower-approach* works well when clear optical boundaries exist between different landscape components surrounding the EC tower. Observing CO<sub>2</sub> fluxes from smaller ponds as the one chosen in this study would likely have resulted in larger uncertainty of the estimated CO<sub>2</sub> flux.

*Possible application  
of one-tower  
-approach*

As a benefit, the *one-tower-approach* of source-partitioning CO<sub>2</sub> fluxes into the CO<sub>2</sub> fluxes from different landscape components that one only requires to have the financial resources for one EC observation tower and its instruments. Nevertheless, with common costs of around 100.000 €, financing a single EC tower can be challenging. To source-partition CO<sub>2</sub> fluxes using just one tower, a clear boundary of landscape components surrounding the EC tower must exist, as was the case at the study site, with open water to the east and semi-terrestrial tundra to the west.

### 2.1.2 Approach using two eddy covariance towers

For the *two-tower-approach*, I used data from two EC towers located approximately 500 meters apart (*EC Tower 1* and *EC Tower 2* in Fig. 2). Both towers are surrounded by polygonal tundra. As was required in the *one-tower-approach*, I assumed that a mixed signal of EC measurement was a linear combination of each flux type in the footprint-weighted by its respective contribution to the footprint. Based on this assumption, a set of two equations (one for each EC tower, Eq. 6 and 7) described the observed CO<sub>2</sub> flux as a sum of flux components, each multiplied with their footprint-weighted fraction. By rearranging these two equations, I estimated two time series of two landscape components' CO<sub>2</sub> fluxes (Eq. 8 and 9). These two different landscape components were semi-terrestrial tundra and thermokarst ponds.

Source-partitioning  
CO<sub>2</sub> fluxes from  
pond and semi-  
terrestrial tundra

In the *two-tower-approach*, I also source-partitioned the CO<sub>2</sub> fluxes from the semi-terrestrial tundra into the CO<sub>2</sub> fluxes from dry and wet tundra. As previously mentioned regarding the one-tower approach, I assumed a pond CO<sub>2</sub> flux without a diurnal cycle and large variations. Therefore, I subtracted the median of the pond CO<sub>2</sub> flux (multiplied with the *footprint-weighted fraction*) from the observed CO<sub>2</sub> flux to determine two CO<sub>2</sub> flux time series purely from semi-terrestrial tundra (Eq. 10 and 11). From these two time series of semi-terrestrial tundra, I estimated the CO<sub>2</sub> fluxes from dry and wet tundra, respectively (Eq. 12 and 13).

Source-partitioning  
CO<sub>2</sub> fluxes from dry  
and wet tundra

A benefit of the *two-tower-approach* is that CO<sub>2</sub> flux time series for two landscape components from a heterogeneous landscape can be estimated as early as step 1. In the *one-tower-approach*, low-varying pond CO<sub>2</sub> flux was necessary to receive a similar result. The results from both approaches showed good agreement regarding pond CO<sub>2</sub> fluxes. In the *one-tower-approach*, a pond CO<sub>2</sub> flux between 11 July and 10 September of  $0.13_{0.00}^{0.24} \text{ g m}^{-2} \text{ d}^{-1}$  was found, and in the *two-tower-approach*, pond CO<sub>2</sub> fluxes of  $0.10_{0.02}^{0.19} - 0.11_{-0.01}^{0.26} \text{ g m}^{-2} \text{ d}^{-1}$  (median<sub>25th percentile</sub><sup>75th percentile</sup>) were found. Based on these results, both source-partitioning approaches showed good results for pond CO<sub>2</sub> flux.

Results from both  
source-partitioning  
approaches

In the *two-tower-approach* I also aimed to source-partition the semi-terrestrial tundra into the landscape components of dry and wet tundra. I estimated the two landscape components' CO<sub>2</sub> flux based on two available land-cover classifications, and the results highly depended on the chosen classification (Fig. 27a and 27b). Both land-cover classifications include dry and wet tundra. However, the distribution of these two classes differs between the land cover classifications, especially to the west of EC tower 2, as shown in the diverging footprint-weighted land surface contribution in figures 23a and 23b. The classification of these two components (dry and wet tundra) highly depends on the moisture content and vegetation of the tundra. As these parameters can change over time, the land cover classifications

can produce different results for the same location over time. Although the *two-tower-approach* showed reliable results for pond CO<sub>2</sub> fluxes, the diverging result of dry and wet tundra CO<sub>2</sub> fluxes showed that source-partitioning two surface components that are highly similar and challenging to differentiate using land-cover classifications is difficult.

Comparison to other  
source-partitioning  
approaches

Similar approaches of source-partitioning EC fluxes from heterogeneous landscapes have been performed by Holl et al. (2020), Jammet et al. (2017), Rößger et al. (2019a,b), and Tuovinen et al. (2019). In most studies, the authors have separated fluxes from different vegetation types. In the study by Jammet et al. (2017), fluxes from a lake and a fen in a subarctic environment were source-partitioned, thus, representing a similar approach to this thesis. In general, flux estimations from Arctic waterbodies are still rare, especially using the EC method (Vonk et al., 2015). Therefore, the results from the *one-* and *two-tower-approach* represent useful additions to the knowledge on CO<sub>2</sub> fluxes from small waterbodies in the Arctic.

## 2.2 WHERE DOES THE CARBON GO? THE NET ECOSYSTEM CARBON BALANCE OF A POLYGONAL TUNDRA LANDSCAPE

Setting the stage on  
Samoylov island

The polygonal tundra represents a heterogeneous landscape in the Arctic. It is covered by semi-terrestrial tundra of drier and wetter areas and open water areas of different sizes. At the research site, the river terrace of Samoylov island, dry tundra accounts for 65% of the landscape area, while wet tundra accounts for 12%, open water accounts for 16% and overgrown water accounts for 7% (Muster et al., 2012). In this thesis, I focus on C fluxes from smaller thermokarst ponds, which compose about 8% of the river terrace area. Larger thermokarst lakes (outlined in yellow in Fig. 11 b) represent the other 8% of open water areas, though these lakes are not part of the research in this thesis.

Results from aquatic  
CO<sub>2</sub> and CH<sub>4</sub> fluxes

The C fluxes of various landscape components in this heterogeneous area differ greatly. For example, thermokarst ponds continuously emitted CO<sub>2</sub> during the observation period with a CO<sub>2</sub>-C rate of  $+0.13_{0.00}^{0.24} \text{ g m}^{-2} \text{ d}^{-1}$  (median<sub>25th percentile</sub><sup>75th percentile</sup>). Meanwhile, neighboring areas of semi-terrestrial tundra showed an average net CO<sub>2</sub>-C uptake of about  $-0.27 \pm 0.007 \text{ g m}^{-2} \text{ d}^{-1}$ . Due to the spatial prevalence of semi-terrestrial tundra in this landscape, the net CO<sub>2</sub> flux of the polygonal tundra landscape was dominated by the CO<sub>2</sub> flux of the semi-terrestrial tundra. However, although thermokarst ponds only cover about 8% of this landscape, their low but constant CO<sub>2</sub> emission held an important implication for the CO<sub>2</sub> balance of the landscape: the landscape CO<sub>2</sub> uptake decreased by 11% when CO<sub>2</sub> emissions from thermokarst ponds are included compared to the uptake of a landscape that is completely covered by semi-terrestrial tundra.

CH<sub>4</sub> fluxes from the polygonal tundra showed a more complex spatial variability compared to CO<sub>2</sub> fluxes. My results suggested that CH<sub>4</sub> fluxes cannot be classified into fluxes from waterbodies and semi-terrestrial tundra, as it has been the case for CO<sub>2</sub> fluxes. Even within one pond, CH<sub>4</sub> fluxes are spatially variable: one shore of a thermokarst pond emitted significantly higher rates of CH<sub>4</sub> compared to the other shore of the same pond, even though the shores had similar vegetation cover and water depths close to the shore. Furthermore, the open water area of the pond and the semi-terrestrial tundra had similar CH<sub>4</sub> emissions without significant differences (Fig. 16). This result was surprising, as the emission pathways of CH<sub>4</sub> in the pond and the semi-terrestrial tundra are likely different, and CO<sub>2</sub> fluxes from these two landscape components show significant differences.

The estimation of pond CO<sub>2</sub>-C flux from this thesis is mostly consistent with previous estimates of aquatic CO<sub>2</sub>-C fluxes in other permafrost-affected regions, ranging from 0.059 (Jammet et al., 2017) to 0.11 (Eugster et al., 2003) to 0.22 g m<sup>-2</sup> d<sup>-1</sup> (Jonsson et al., 2008). Surprisingly, the results from this thesis are 12–18 fold smaller compared to a previous study conducted at the same study site (Abnizova et al., 2012). The indirect measurement technique used by the authors to estimate aquatic CO<sub>2</sub> fluxes (thin boundary layer method by Liss and Slater 1974) could partially explain the strong diverging observations; however, the main cause for these differences remains unknown.

From the merged polygonal pond, we estimated a CH<sub>4</sub>-C flux of 13.90<sup>18.46</sup><sub>11.02</sub> mg m<sup>-2</sup> d<sup>-1</sup> (median<sup>75th percentile</sup><sub>25th percentile</sub>). This is more than the fluxes from a subarctic lake that Jammet et al. (2017) measured; they reported an average yearly CH<sub>4</sub>-C flux of 13.42 ± 1.64 mg m<sup>-2</sup> per day and an average CH<sub>4</sub>-C flux during the ice-free season of 7.58 ± 0.69 mg m<sup>-2</sup> per day. Similar to our findings, CH<sub>4</sub>-C emissions were reported in 32 non-Yedoma thermokarst lakes in Alaska (16.80 ± 8.61 mg m<sup>-2</sup> d<sup>-1</sup>; Sepulveda-Jauregui et al., 2015). The same order of magnitude of CH<sub>4</sub>-C emissions are also reported in a synthesis of 149 thermokarst water bodies north of ~ 50° N (27.57 ± 14.77 mg m<sup>-2</sup> d<sup>-1</sup>; Wik et al., 2016). The CH<sub>4</sub>-C fluxes from semi-terrestrial tundra are consistent with other literature focusing on the same study site. A recent study by Rößger et al. (2022) has reported mean thaw season CH<sub>4</sub>-C emissions of about ~9.33 mg m<sup>-2</sup> d<sup>-1</sup>, being in the same range compared to the estimates from this thesis (12.55<sup>16.07</sup><sub>9.65</sub> mg m<sup>-2</sup> d<sup>-1</sup>, median<sup>75th percentile</sup><sub>25th percentile</sub>, Fig. 16). A similar study by Sachs et al., 2008 reported mean daily CH<sub>4</sub>-C emissions of 14 mg m<sup>-2</sup> d<sup>-1</sup> during the thaw season.

Whether the vertical C fluxes represent the majority of C fluxes from this landscape remained unclear prior to the study in appendix A; carbon fluxes can potentially also occur laterally with the water runoff. To my knowledge, no study has combined vertical and lateral C fluxes to estimate the NECB for a polygonal tundra site. My results

*Discussion on aquatic CO<sub>2</sub> and CH<sub>4</sub> fluxes*

*Results from lateral C flux estimation*

in appendix A showed that during the 93-day observation period (June 8 – September 8, 2014), the NECB accumulated to  $-17.6$  to  $-17.5$  ( $\pm 1.2$ )  $\text{g m}^{-2}$  (see Fig. 6). The vertical fluxes of  $\text{CO}_2$  and  $\text{CH}_4$  had cumulative sums of  $-19.0 \pm 1.2$  and  $1.0 \pm 0.02$   $\text{g m}^{-2}$ , respectively, and the lateral C fluxes of dissolved inorganic carbon (DIC) and dissolved organic carbon (DOC) accumulated to  $0.31$ – $0.38$  and  $0.06$ – $0.08$   $\text{g m}^{-2}$ , respectively. Overall, the vertical  $\text{CO}_2$  flux dominated in the NECB, while the  $\text{CH}_4$  flux and the lateral C fluxes played only a minor role on the timescale of the observation period. However, the relationship between the vertical and the lateral fluxes changes: following the spring melt, meltwater and water from a previous flood resulted in the highest lateral C fluxes of the observation period. In this first week of observation, the  $\text{CO}_2$  flux was negative, indicating a  $\text{CO}_2$  uptake, whereas the NECB was positive, indicating a carbon release. With the progressing vegetation period, high levels of  $\text{CO}_2$  uptake dominated the NECB.

## CONCLUSION AND OUTLOOK

---

In the first part, I present two approaches for source-partitioning CO<sub>2</sub> fluxes from a heterogeneous landscape using the EC method. The two presented methods worked well for my first application, source-partitioning CO<sub>2</sub> fluxes from thermokarst ponds and semi-terrestrial tundra. However, the application area of the *one-tower-approach* remains relatively narrow. Even though I found interesting and relevant results of C fluxes at this study site, this method might not be universally applicable. The fundamental requirement of "no diurnal cycle for water CO<sub>2</sub> flux" limits this method to specific landscapes. When this requirement is not fulfilled, and researchers still aim to source-partition C fluxes, a tower setup at the edge between two landscape components could be useful, as shown by Holl et al., 2020; Rößger et al., 2019a,b. Or alternatively, a combination of EC with chamber flux observation could be helpful to source-partition C fluxes from different landscape components (Eckhardt et al., 2019; Tuovinen et al., 2019).

*Limitations of  
one-tower-approach*

For heterogeneous landscapes, such as the polygonal tundra, the *two-tower-approach* could represent a useful tool to source-partition the CO<sub>2</sub> or other GHGs fluxes from any given two landscape components. The only requirement for the *two-tower-approach* is that the two landscape components can be accurately classified in a land cover classification. The second step of the *two-tower-approach* has shown that a precise land cover classification represents a crucial requirement for successful source-partitioning. A useful application would be a case where a long-term EC observatory would be supported by a temporary EC tower, as I have presented in this thesis.

In the second part, I show different C fluxes from the polygonal tundra landscape and aim to determine where the carbon goes. Arctic permafrost soils are likely to thaw more deeply in a warming climate, and abrupt thaw could occur widely. Due to abrupt thaw, more thermokarst ponds are likely to be created within the tundra and thereby shift the landscape C flux (Rodenhizer et al., 2022; Schuur et al., 2022; Turetsky et al., 2020). In a hypothetical case of doubling the land area of thermokarst ponds on Samoylov island, with all thermokarst ponds having a CO<sub>2</sub> flux comparable to my estimations, the current CO<sub>2</sub> uptake of the landscape on Samoylov island would decrease by ~25% instead of 11%, as I estimated in this thesis. Thus, the landscape C flux could significantly change when the areal extent of landscape components changes, even if the area-specific C fluxes of each landscape component remain the same.

*Possible future  
scenarios of  
Samoylov C fluxes*

In the analysis of polygonal tundra CH<sub>4</sub> flux dynamics, I found that CH<sub>4</sub> fluxes significantly differ between two shores of the same thermokarst pond. Coastal erosion of the shores, meteorological conditions, differences in vegetation cover and local ebullition were excluded from possible drivers of these significant differences and thus revealed the need for additional research in this field. Researchers could focus on more in-depth process modeling for aquatic CH<sub>4</sub> emissions, as begun by Rehder (2022). However, the underlying processes are likely highly complex to model adequately, so a larger measurement campaign on aquatic CH<sub>4</sub> emissions would also be useful, especially one that includes bubble traps on the water surface. Areas of high ebullition could be located by visual inspection of bubbles trapped in winter ice. In such a measurement campaign, the EC method could also be used to capture the landscape CH<sub>4</sub> fluxes from a larger region.

The NECB estimation for the polygonal tundra site suggested that lateral C fluxes play a minor role in the ecosystem's C balance during the summer period. Even with potentially high lateral C fluxes directly following the beginning of the snow melt, lateral C fluxes at this site still play a less important role in the ecosystem's C balance. However, the relevance of lateral C fluxes may become more important in the future if erosion of the polygonal tundra site were to occur. Two studies have found substantial organic C transport from eroding cliffs Arctic rivers: Kanevskiy et al. (2016) reported an annual organic C loss of 880,000 kg from a 650 m long cliff in Alaska, and Fuchs et al. (2020) found an annual organic C loss of 5,200,000 kg from a 1,600 m long cliff in the Lena River delta. If these erosion events were to occur at this thesis's study site, lateral dissolved fluxes, especially particulate carbon, would most likely counteract the ecosystem's sink of C at this site.

*Potential relevance of lateral C fluxes at other sites*

This thesis has shown interesting results of C fluxes from the polygonal tundra. However, there are still research questions open that could be addressed in future field campaigns:

*Perspective for future research*

- Land-atmosphere C fluxes from the Lena river and the bare sand of floodplains could be studied by setting up an EC tower at the shore of the Lena river. The *one-tower-approach* could be used for source-partitioning the C fluxes from the two surfaces.
- A temporary EC tower could be relocated throughout the season to capture the potential spatial variability of C fluxes in the heterogeneous polygonal tundra landscape.
- Observation of lateral C fluxes could be conducted at a site with erosion of polygonal tundra and, therefore at a site with potential relevant flux contribution of particulate C.

### 3.1 TAKE HOME MESSAGES

This thesis focuses on lateral and vertical C fluxes from the heterogeneous polygonal tundra. The most relevant results from this thesis are summarized here:

- Lateral C fluxes of DIC and DOC likely do not represent relevant C fluxes in the thaw season NECB budget of a non-eroding polygonal tundra site.
- Aquatic CO<sub>2</sub> emissions from a thermokarst pond within the polygonal tundra are low but constant. This low emission from thermokarst ponds still considerably decreases the net CO<sub>2</sub> uptake of the polygonal tundra landscape.
- Aquatic CH<sub>4</sub> emissions are highly variable from a single thermokarst pond within the polygonal tundra, and the processes understanding behind the variability remains challenging.
- A method using data from two EC towers revealed no additional information on aquatic CO<sub>2</sub> emissions compared to a method using data from one EC tower, though the method with two EC towers can be useful in future applications where precise land cover classifications are available.



Part I

APPENDIX



## LATERAL CARBON EXPORT HAS LOW IMPACT ON THE NET ECOSYSTEM CARBON BALANCE OF A POLYGONAL TUNDRA CATCHMENT

---

Lutz Beckebanze<sup>1</sup>, Benjamin R. K. Runkle<sup>1,2</sup>, Josefine Walz<sup>1,3</sup>, Christian Wille<sup>4</sup>, David Holl<sup>1</sup>, Manuel Helbig<sup>5</sup>, Julia Boike<sup>6,7</sup>, Torsten Sachs<sup>4</sup>, Lars Kutzbach<sup>1</sup>,

<sup>1</sup>Institute of Soil Science, Center for Earth System Research and Sustainability (CEN), Universität Hamburg, Hamburg, Germany

<sup>2</sup>Department of Biological and Agricultural Engineering, University of Arkansas, Fayetteville, AR, USA

<sup>3</sup>Climate Impacts Research Centre, Department of Ecology and Environmental Science, Umeå University, 98107 Abisko, Sweden

<sup>4</sup>Helmholtz-Zentrum Potsdam – Deutsches GeoForschungsZentrum (GFZ), Potsdam, Germany

<sup>5</sup>Department of Physics & Atmospheric Science, Dalhousie University, Halifax, Canada

<sup>6</sup>Alfred Wegener Institute Helmholtz Centre for Polar and Marine Research, Potsdam, Germany

<sup>7</sup>Department of Geography, Humboldt-Universität zu Berlin, Berlin, Germany

This chapter is published in Biogeosciences under the DOI <https://doi.org/10.5194/bg-19-3863-2022>

### A.1 ABSTRACT

Permafrost-affected soils contain large quantities of soil organic carbon (SOC). Changes in the SOC pool of a particular ecosystem can be related to its net ecosystem carbon balance (NECB) in which the balance of carbon (C) influxes and effluxes is expressed. For polygonal tundra landscapes, accounts of ecosystem carbon balances in the literature are often solely based on estimates of vertical carbon fluxes. To fill this gap, we present data regarding the lateral export rates of dissolved inorganic carbon (DIC) and dissolved organic carbon (DOC) from a polygonal tundra site in the north Siberian Lena River delta, Russia. We use water discharge observations in combination with concentration measurements of waterborne carbon to derive the lateral carbon fluxes from one growing season (2 June–8 September 2014 for DOC, 8 June–8 September 2014 for DIC). To put the lateral C fluxes into context, we furthermore present the surface–atmosphere

eddy covariance fluxes of carbon dioxide (CO<sub>2</sub>) and methane (CH<sub>4</sub>) from this study site.

The results show cumulative lateral DIC and DOC fluxes of 0.31–0.38 and 0.06–0.08 g m<sup>-2</sup>, respectively, during the 93 d observation period (8 June–8 September 2014). Vertical turbulent fluxes of CO<sub>2</sub>-C and CH<sub>4</sub>-C accumulated to  $-19.0 \pm 1.2$  and  $1.0 \pm 0.02$  g m<sup>-2</sup> in the same period. Thus, the lateral C export represented about 2 % of the net ecosystem exchange of (NEE) CO<sub>2</sub>. However, the relationship between lateral and surface–atmosphere fluxes changed over the observation period. At the beginning of the growing season (early June), the lateral C flux outpaced the surface-directed net vertical turbulent CO<sub>2</sub> flux, causing the polygonal tundra landscape to be a net carbon source during this time of the year. Later in the growing season, the vertical turbulent CO<sub>2</sub> flux dominated the NECB.

## A.2 INTRODUCTION

Permafrost regions have accumulated  $1300 \pm 200$  Pg of soil organic carbon (SOC), of which  $472 \pm 27$  Pg is stored within the top 1 m of soil (Hugelius et al., 2014). In a warming climate, previously frozen SOC can be mobilized and lost from the permafrost-affected ecosystems through vertical and lateral carbon fluxes. Many studies (e.g., Koven et al., 2015; Schuur et al., 2015) focus on vertical gaseous carbon (C) fluxes in the form of the greenhouse gases (GHGs) carbon dioxide (CO<sub>2</sub>) and methane (CH<sub>4</sub>). However, C loss can also occur laterally as dissolved organic carbon (DOC) and dissolved inorganic carbon (DIC), which are exported through runoff of meltwater and rainwater (e.g., Fouché et al., 2017; Olefeldt and Roulet, 2014) and may be emitted in the form of GHGs to the atmosphere outside of the spatial observation range (such as in coastal regions as shown by Lougheed et al., 2020). Thus, to estimate the net ecosystem carbon balance (NECB), both vertical and lateral C fluxes must be considered (Chapin et al., 2006). Although scholars have identified lateral C transport as an important mechanism of C losses from terrestrial ecosystems in the Arctic (Zhang et al., 2017), little is known about the contribution of lateral C fluxes to the NECB. So far, lateral C fluxes have only been included in NECB estimations in two subarctic catchments in northern Sweden. In the first catchment, lateral C fluxes contribute 6%–15% (Chi et al., 2020) and 4%–28% to the annual NECB (Öquist et al., 2014), and in the second catchment, lateral C fluxes represent 35% of the NECB (Lundin et al., 2016). To our knowledge, there has been no attempt yet to combine the lateral and vertical C fluxes in an Arctic ecosystem. Here, we estimate the NECB for a Siberian Arctic tundra ecosystem and present the individual flux contributions during one growing season. Since 2002, the vertical C fluxes of CO<sub>2</sub> and CH<sub>4</sub> have been observed at our study site (Holl et al., 2019b) using the

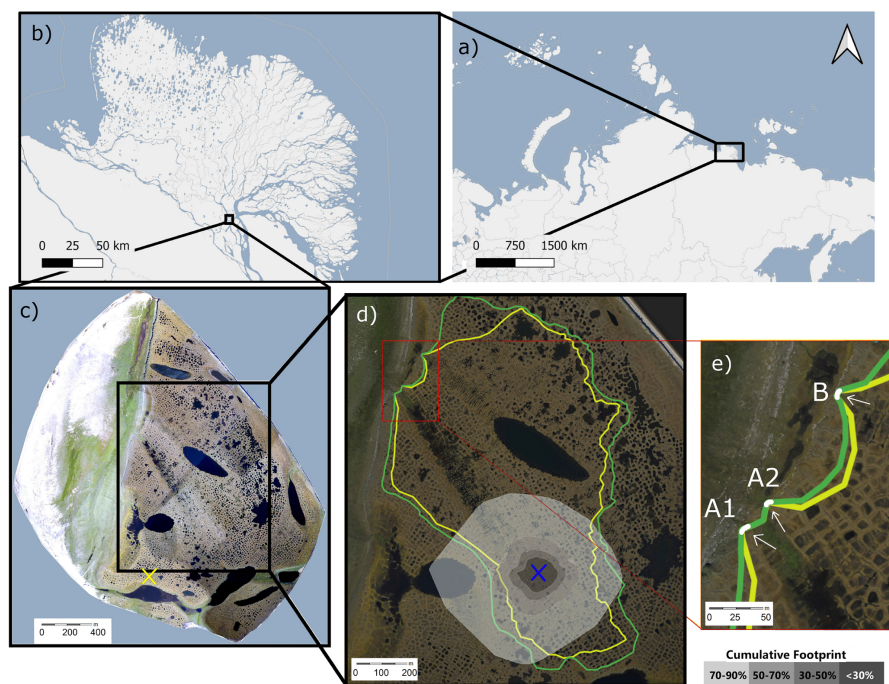


Figure 4: Top: map of northern Russia (a) and the Lena River delta (b). Bottom: map of Samoylov Island (c) with the maximum (green) and minimum (yellow) catchment size (d). The blue cross in (d) marks the eddy covariance tower's location, and the cumulative footprint is shown in gray shades. Of the flux, 30% likely originated from within the dark gray area, 50% from within the medium dark gray area, 70% from within the medium light gray area, and 90% from within the light gray area. The yellow cross in (c) denotes the location of the meteorological station with the active layer depth observations. Panel (e) shows the locations of outflows A<sub>1</sub>, A<sub>2</sub>, and B. Map data from © OpenStreetMap contributors 2020, distributed under the Open Data Commons Open Database License (ODbL) v1.0 (a, b) and modified after Boike et al. (2012b) (c, d, e).

eddy covariance method (Baldocchi, 2003). The study site, located in the north Siberian Lena River delta, is characterized by polygonal lowland tundra landscape. In this study, we combine the vertical C fluxes ( $F_{\text{CO}_2}$  and  $F_{\text{CH}_4}$ ) with the lateral C fluxes ( $F_{\text{DOC}}$  and  $F_{\text{DIC}}$ ) to derive the NECB for one growing season in 2014. We also compare the temporal dynamics of DIC and DOC concentrations with respect to the water discharge rate to find a potential driver for the concentrations of dissolved carbon. In summary, this study examines two research questions: (1) what is the influence of the lateral waterborne C fluxes on the NECB of the polygonal tundra landscape? (2) How do DOC and DIC concentrations and fluxes develop over the growing season?

### A.3 METHODS

#### A.3.1 *Study site*

The study site, Samoylov Island (Fig. 22), which is located in the southern part of the Russian Lena River delta, consists of two geomorphological units: a modern floodplain in the west ( $\sim 1.5 \text{ km}^2$ ) and a Late Holocene river terrace in the east ( $\sim 3 \text{ km}^2$ ; Boike et al., 2013). The floodplain and river terrace are at elevations of 0–8 and 8–13 m, respectively, above the water level of the Lena River (Boike et al., 2012a). Rain and meltwater from the river terrace drain towards the Lena River and the lower-lying floodplain. Polygonal tundra with a shallow active layer (less than 1 m) and wet to moist tundra vegetation (sedges, mosses, dwarf shrubs) characterizes the river terrace. Following the World Reference Base for Soil Resources (WRB, 2014), the main soil types include Histic Cryosols in polygon centers and Turbic Glacic Cryosols at elevated polygon rims on the river terrace (Boike et al., 2013; Pfeiffer and Grigoriev, 2002; Zubrzycki et al., 2014).

#### A.3.2 *Catchment characteristics*

We estimated the catchment size by analyzing a digital elevation model (DEM) of Samoylov Island (Boike et al., 2012a) in ArcMap 10.1 (Environmental Systems Research Institute (ESRI), 2012). This DEM has a vertical and horizontal accuracy of less than 1 m. Due to the low elevation gradient in some catchment areas, we also used field observations from 2019 and shoreline measurements during different stages of the spring flood in 2014 to validate our estimations of the catchment size. To distinguish flow paths, we furthermore used the orthomosaic of Samoylov Island produced by Boike et al. (2012b) with an average horizontal resolution of 0.33 m. Based on this methodology, we estimated a larger catchment size than Helbig et al. (2013) did. This catchment drains through three outflows ( $A_1$ ,  $A_2$ , and B). We estimated a catchment size of 0.69–0.84  $\text{km}^2$  (Fig. 22d; green denotes the maximum estimate, while yellow denotes the minimum estimate).

The polygonal tundra in this catchment is characterized by intact and degraded ice-wedge polygons with water-filled centers as well as polygons with dry centers. Water-filled troughs between the polygons are also present (Kartozia, 2019). A low-lying and largely inundated area stretches from the center of the catchment towards the outflows  $A_1$  and  $A_2$  (Fig. 22d).

#### A.3.3 *Water discharge*

Between 2 June and 8 September 2014, we measured the water level at outflows  $A_1$ ,  $A_2$ , and B using pressure sensors (Mini-Diver, Schlum-

berger Water Services, the Netherlands) placed within 10 cm of the weir wall outside of the zone of fast-flowing water. To calculate the water level above the diver, we subtracted the barometric pressure from the diver pressure. We measured the barometric pressure at the eddy covariance tower (CS100, Campbell Scientific, USA). Prior to the water discharge rate calculation, we corrected the water level estimations with a linear relationship with manual water level measurements (obtained using a ruler). The water discharge rates at outflows A<sub>1</sub> and A<sub>2</sub> were observed with V-notch weirs as described by Helbig et al. (2013). To calculate the water discharge rates, we used the Kulin and Compton (1975) method for calculating V-notch weirs:  $Q_a = \frac{8}{15} C_{\text{weir}} \sqrt{2g} \tan\left(\frac{1}{2}\alpha\right) h^{\frac{3}{2}}$ , where  $Q_a$  is the discharge rate in  $\text{L s}^{-1}$ ,  $h$  is the water level above the notch determined from the pressure sensor in feet (ft),  $C_{\text{weir}} = 0.58$  is the dimensionless weir constant,  $g = 9.81 \text{ m s}^{-2}$  is the gravitational acceleration, and ( $\alpha = 60^\circ$ ) is the angle of the V notch. After performing the water discharge rate calculations, we validated the estimated water discharge rates with manual bucket measurements (with a stopwatch and a defined bucket volume).

Outflow B was located about 150 m north of the A outflows, and the discharge rate was measured using a long-throated flume (RBC flume, 13.17.02, Eijkelkamp Agrisearch Equipment, the Netherlands). We calculated  $Q_b$  using the manufacturer's equation for this RBC flume:  $Q_b = -0.066 + 0.016 h + 0.00063 h^2 + 7 \times 10^{-7} h^3$ , where ( $h$ ) is the water level above the notch in millimeters and  $Q_b$  is the water discharge rate in  $\text{L s}^{-1}$ .

#### A.3.4 Dissolved inorganic carbon (DIC)

Between 8 June and 8 September 2014, we deployed a  $\text{CO}_2$  sensor in the water column at outflow A<sub>1</sub> ( $\text{CO}_2$  measurement system with multisensor module MSM-S2, UIT GmbH, Germany). This sensor measured the concentration of dissolved  $\text{CO}_2$  ( $C_{\text{dCO}_2}$ ) every 5 min (each measurement 15 s long).

DIC consists of dissolved  $\text{CO}_2$  (as free  $\text{CO}_2$  and carbonic acid;  $\text{H}_2\text{CO}_3$ ), bicarbonate ions ( $\text{HCO}_3^-$ ), and carbonate ions ( $\text{CO}_3^{2-}$ ). In a freshwater system, each component's contribution to the DIC concentration depends on water temperature and pH; the bicarbonate equilibrium describes this relationship. More details on the bicarbonate equilibrium can be found in the book by Dodds and Whiles (2010). We calculated the carbonic acid concentration ( $C_{\text{HCO}_3^-}$ ) from  $C_{\text{dCO}_2}$ , water temperature, and pH:  $C_{\text{HCO}_3^-} = \frac{K_1 \cdot C_{\text{dCO}_2}}{a(\text{H}^+)}$ , where  $a(\text{H}^+) = 10^{-\text{pH}}$ . The dimensionless value of  $K_1$  is temperature-dependent and, following Wong and Hsu (1991), is described as  $K_1 = 10^{15.11 - 0.034 \cdot T - 3406.12 \cdot T^{-1}}$ , where  $T$  describes the water temperature in the unit kelvins (K).

The pH value was frequently but not continuously measured throughout the 2014 growing season ( $N = 40$ ). To fill the gaps in the pH time series, we applied a running mean. The pH values varied between 6.60 and 6.99; therefore, the contribution of carbonate to  $C_{\text{DIC}}$  was not relevant. Due to the negligible amount of carbonate, we calculated  $C_{\text{DIC}}$  as the sum of  $C_{\text{HCO}_3^-}$  and  $C_{\text{dCO}_2}$ .

The  $C_{\text{dCO}_2}$  sensor failed to record accurate measurements between 18 and 30 July, and thus we excluded the recorded values during this period. To fill this data gap, we applied an artificial neural network (ANN), targeting  $C_{\text{dCO}_2}$  and using four input parameters (air temperature, relative air humidity, vertical  $\text{CO}_2$  flux, and DOC concentration). We set up the ANN as a multilayer perceptron with 10 hidden neurons in MATLAB's Deep Learning Toolbox (*MATLAB Deep Learning Toolbox 2019b*) using Levenberg–Marquardt backpropagation as an optimization algorithm. We divided the datasets into training (70%), validation (15%), and testing (15%) subsets.

#### A.3.5 Dissolved organic carbon (DOC)

We routinely analyzed unfiltered water samples ( $N = 126$ ) from all three outflows using a portable UV–Vis spectrometer probe (spectro::lyser, s::can Messtechnik GmbH, Austria). The measurements were supported by lab analyses to calibrate the spectrometer probe observations and increase data availability ( $N = 41$ ). Water samples for calibration were collected in acid-washed glass bottles, acidified to a pH value of 2, cooled to 4 °C for transport, and filtered (40—m) prior to analysis. Analysis was conducted using a total organic carbon (TOC) analyzer (TOC-L, Shimadzu, Japan). We estimated  $C_{\text{DOC}}$  from unfiltered water samples following the workflow presented by Avagyan et al. (2014). This approach is based on the finding that different absorbance bands of a spectrometer probe can be suitable for the description of the DOC concentration, depending on the types of organic compounds in the sample water. We found a good agreement of  $R_{\text{adj}}^2 = 0.82$  between  $C_{\text{DOC}}$  from the spectrometer probe and  $C_{\text{DOC}}$  from the TOC analyzer (Fig. 10). Details of the method can be found in Appendix A.7.1.

#### A.3.6 DOC and DIC flux

The catchment-area-normalized lateral carbon fluxes of DOC ( $F_{\text{DOC}}$ ) and DIC ( $F_{\text{DIC}}$ ) are the product of water discharge rate  $Q$  and  $C_{\text{DOC}}$  and  $C_{\text{DIC}}$ , respectively, divided by the area of the catchment:  $F_{\text{DOC}} = Q \cdot C_{\text{DOC}}/a$  and  $F_{\text{DIC}} = Q \cdot C_{\text{DIC}}/a$ , where  $a$  describes either the minimum or the maximum estimated catchment size.

### A.3.7 *Environmental conditions*

Precipitation and air temperature were recorded throughout the study period at the meteorological station in the southern part of the island in 1 h intervals; Boike et al. (2019) published these measurements (data obtained from Boike et al., 2019). The growing degree days ( $GDD_{10}$ ) were calculated as the sum of all positive differences between the daily mean air temperature and the reference temperature (defined as 10 °C). The thaw depth was measured at a 150-grid-point array next to the meteorological station by pushing a metal rod vertically into the ground (Boike et al., 2019) and was obtained from the GTN-P database (GTNP Database, 2019).

### A.3.8 *Eddy covariance flux*

We estimated the net vertical fluxes of  $CO_2$  ( $F_{CO_2}$ ),  $CH_4$  ( $F_{CH_4}$ ), and evapotranspiration (ET) using an eddy covariance (EC) measurement system. Holl et al. (2019b) described raw data processing of  $CO_2$  fluxes; and the gap-filled time series were obtained from Holl et al. (2018). High-frequency fluctuations in  $CH_4$  concentration were observed with a LI-7700 gas analyzer (LI-COR Biosciences, USA). Data processing of  $CH_4$  fluxes followed the same method as described in Holl et al. (2019b) for open-path  $CO_2$  fluxes. Gap filling of  $CH_4$  fluxes was performed by applying a running mean of 48 h. ET fluxes were observed using a LI-7500A gas analyzer (LI-COR Biosciences, USA), and the data processing followed Helbig et al. (2013).

### A.3.9 *Cumulative fluxes*

To quantify the impact carbon losses due to lateral transport have on the carbon balance of the catchment, we calculated the cumulative carbon fluxes of  $CO_2$ ,  $CH_4$ , DIC, and DOC for the period between 8 June and 8 September 2014 in 30 min intervals. Other flux components of the lateral C flux, e.g., particulate organic carbon or particulate inorganic carbon, are not accounted for in this study. Between 2 and 7 June 2014, the component of  $C_{DIC}$  had not been obtained yet; therefore, this period is not included in the sums of carbon fluxes. However, this period is still part of the study period since the spring flood had a great influence on the DOC flux dynamics.

### A.3.10 *Uncertainty estimation*

In this study, uncertainties from random errors are indicated by the  $\pm$  symbol, and the ranges of uncertainties from systematic errors are indicated with an en dash (–).

We calibrated the observed water discharge rate  $Q$  against manual height measurements. Therefore, we assumed random errors from both pressure sensors to dominate the uncertainty in  $Q$ . According to the manuals, the diver pressure sensor we used has a typical accuracy of 0.05 % at full scale (however, the error is not further specified). The atmospheric pressure sensor has an accuracy of  $\pm 1$  hPa (1 standard deviation). We used the Gaussian error propagation to estimate the resulting uncertainty  $u_Q$  following two steps. First, we estimated the resulting error in the height measurement  $u_{pH} = \sqrt{u_{p_d}^2 + u_{p_a}^2}$ , where  $u_{pH}$  describes the uncertainty in the water level height measurement in hectopascals (hPa) and  $u_{p_d}$  and  $u_{p_a}$  describe the error in the diver and the atmospheric pressure sensor, respectively. We converted  $u_{pH}$  to the unit of millimeters,  $u_h$ , by dividing  $u_{pH}$  by the density of water and the earth's gravitational force. Second, we estimated the resulting uncertainty in  $Q$  as  $u_Q = \frac{\delta Q}{\delta h} \cdot u_h$ , where  $\frac{\delta Q}{\delta h}$  describes the partial derivative from  $Q$  with respect to  $h$ .

The uncertainty in the DOC concentration results from the limits of the TOC analyzer (TOC-L, Shimadzu, Japan). The manufacturer states a maximum error of 1.5 % in repetitive measurements. We used the RMSE between the modeled DOC concentration from the spectrometer and the DOC concentration from the TOC analyzer to estimate DOC concentration's uncertainty,  $u_{C_{DOC}}$ .

For the estimation of the uncertainty in  $C_{DIC}$  ( $u_{DIC}$ ) we needed to consider the uncertainty in  $C_{dCO_2}$ , water temperature, and pH. According to the  $C_{dCO_2}$  sensor's manual, the sensor has an accuracy of 5 % and, after calibration, an offset of up to  $1 \text{ mg L}^{-1}$ . The accuracy of the water temperature probe is given as  $u_{t_w} = 0.2 \text{ K}$ . We estimated the pH uncertainty from the standard deviation of multiple measurements of the same water sample. The overall uncertainty in  $C_{DIC}$  was calculated using Gaussian error propagation as  $u_{DIC} = \sqrt{u_{dCO_2}^2 + u_{HCO_3}^2}$

$$\text{with } u_{HCO_3} = \sqrt{\left(\frac{\delta C_{HCO_3}}{\delta C_{dCO_2}}\right)^2 \cdot u_{dCO_2}^2 + \left(\frac{\delta C_{HCO_3}}{\delta pH}\right)^2 \cdot u_{pH}^2 + \left(\frac{\delta C_{HCO_3}}{\delta T_w}\right)^2 \cdot u_{T_w}^2}.$$

We estimated the systematic and random uncertainty in the lateral C flux separately. Systematic uncertainty, described as  $F_{DOC,sys}$  and  $F_{DIC,sys}$ , occurs due to systematic error in the catchment size and is estimated as  $F_{DOC,sys} = F_{DOC_{amax}} - F_{DOC_{amin}}$ , where  $F_{DOC_{amin}}$  and  $F_{DOC_{amax}}$  denote the DOC flux calculated with the largest and smallest assumed catchment size (resulting in the smallest and the largest DOC flux, respectively).

The random uncertainty in the lateral C flux,  $F_{DOC,rand}$  and  $F_{DIC,rand}$ , resulting from random errors is estimated as

$$F_{DOC,rand} = F_{DOC} \sqrt{\left(\frac{u_Q}{Q}\right)^2 + \left(\frac{u_{C_{DOC}}}{C_{DOC}}\right)^2}.$$

We estimated the systematic uncertainty range of the cumulative lateral C flux ( $\sum F_{DOC,sys}$  and  $\sum F_{DIC,sys}$ ) as the difference between the

cumulative fluxes with the smallest and the largest assumed catchment size:  $\sum F_{\text{DOC,sys}} = \Delta t \sum_{t_1}^{t_n} F_{i_{\text{amax}}} - \Delta t \sum_{t_1}^{t_n} F_{i_{\text{amin}}}$ , where  $\Delta t$  describes the duration of the measurement interval and  $t_1$  and  $t_n$  denote the first and the last time step of the measurement, respectively.

We estimated the random uncertainty in the cumulative lateral C flux ( $\sum F_{\text{DOC,rand}}$  and  $\sum F_{\text{DIC,rand}}$ ) as

$$\sum F_{\text{DOC,rand}} = \Delta t \sqrt{\sum_{t_1}^{t_n} \left( F_{\text{DOC}} \sqrt{\left( \frac{u_Q}{Q} \right)^2 + \left( \frac{u_{C_{\text{DOC}}}}{C_{\text{DOC}}} \right)^2} \right)^2}.$$

For the uncertainty estimation of DIC, we replaced DOC with DIC in the four equations above. In instances in this text where only a range of lateral C flux is provided, we ignored the random uncertainty and focused on the dominant systematic uncertainty.

The uncertainty in the vertical EC fluxes  $u_{F_{\text{CO}_2}}$  and  $u_{F_{\text{CH}_4}}$  was estimated in the flux processing software EddyPro following Finkelstein and Sims (2001). Details on the flux uncertainty estimation of  $F_{\text{CO}_2}$  can be found in Holl et al. (2019b). We estimated the uncertainty in the cumulative vertical fluxes  $u_{\sum F_{\text{CO}_2}}$  using the Gaussian error propagation for random uncertainties, resulting in  $u_{\sum F_{\text{CO}_2}} = \Delta t \sqrt{\sum_{t_1}^{t_n} u_{F_{\text{CO}_2}}^2}$  and  $u_{\sum F_{\text{CH}_4}} = \Delta t \sqrt{\sum_{t_1}^{t_n} u_{F_{\text{CH}_4}}^2}$  for  $F_{\text{CO}_2}$  and  $F_{\text{CH}_4}$ , respectively.

## A.4 RESULTS

### A.4.1 Environmental conditions

To put the observation year of 2014 into perspective, we compared the meteorological conditions at our study site between 8 June and 8 September 2014 to the meteorological conditions during the same 93 d period over 20 years (1998–2018, Fig. 8 in the Appendix). With 87 °C at the end of the 93 d period, the growing degree days (GDDs; Fig. 8a) in 2014 were among the average values, as established by the comparison dataset (67<sub>49</sub><sup>118</sup> °C, median<sub>25th percentile</sub><sup>75th percentile</sup>). The 2014 thaw depths in the center and at the rim of the polygons studied (Fig. 8b and c) in 2014 were among the deepest recorded in a 17-year companion dataset (2002–2018).

The vertical water balance shows the precipitation, evapotranspiration, and water runoff rate between 2 June and 8 September 2014 (Fig. 9). The precipitation accumulation of 94 mm is within the average range for 14 of the available years between 1998–2018 (95<sub>76</sub><sup>138</sup> mm, median<sub>25th percentile</sub><sup>75th percentile</sup>). In the same period, the evapotranspiration accumulated to 161 mm and the lateral water runoff accumulated to 23–38 mm. The 2014 spring flood of the Lena River flooded parts of the catchment (field observation by Benjamin Runkle). Therefore, the

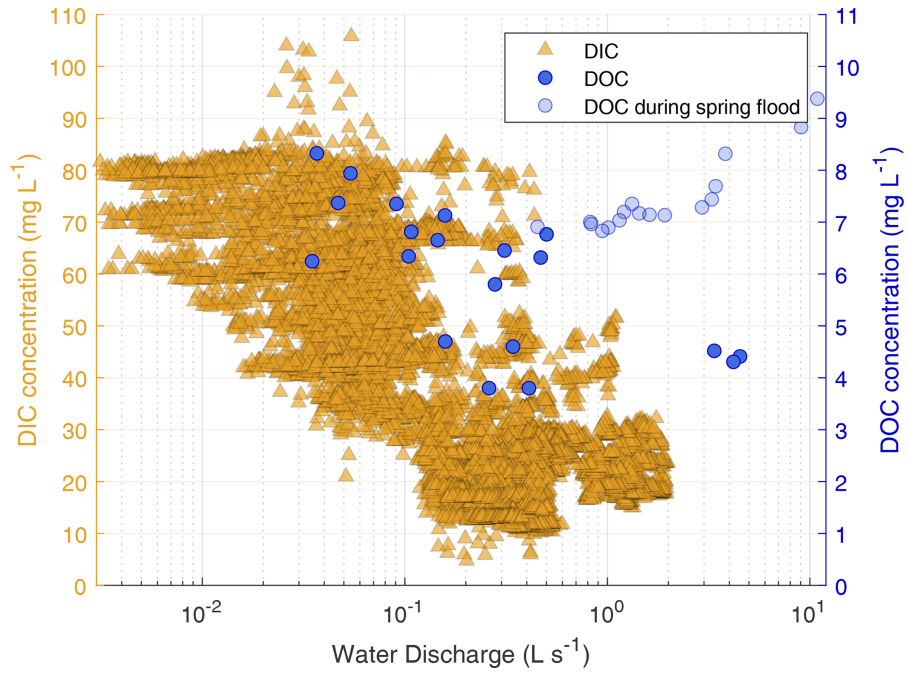


Figure 5: Dissolved inorganic carbon (DIC, triangles) and dissolved organic carbon (DOC, circles) concentrations (note the different scales) against the water discharge rate on a semi-logarithmic scale. DOC concentration is shown on the right y axis, while data after the spring flood (2–8 June) are shown in transparent circles. The DIC concentration was not observed during the spring flood.

lateral water runoff was largely influenced by the out-flowing water of this spring flood, visible at the beginning of the observation period. The larger overall loss of water (183–189 mm) stands out more than the accumulation of water (94 mm) during the observation period. However, one component has been neglected in this water balance: the snow accumulation in winter, which was not observed between 2013 and 2014. However, in the winter of 2008/09, there was a mean snow accumulation of  $65 \pm 35$  mm on Samoylov Island (snow water equivalent; Boike et al., 2013).

#### A.4.2 Lateral carbon flux dynamics

To focus more closely on lateral C flux dynamics, we examine the relationship between water discharge and DIC and DOC concentration (Fig. 5). At outflow A<sub>1</sub>, high DIC concentrations were generally associated with low water discharge. With decreasing water discharge, the DIC concentration rose. A similar effect can be seen with the DOC concentration, which continuously increases as the water discharge rate decreases; data recorded during the river flood are excluded. A comparison of the DIC and DOC concentrations shows that DIC concentrations were  $4.31^{6.41}_{3.28}$  times higher than DOC concentrations (median<sub>25th percentile</sub><sup>75th percentile</sup>).

#### A.4.3 Net ecosystem carbon balance

In this section, we present the NECB for the study period consisting of the lateral ( $F_{\text{DOC}}$  and  $F_{\text{DIC}}$ ) and vertical ( $F_{\text{CO}_2}$  and  $F_{\text{CH}_4}$ ) carbon fluxes. The cumulative fluxes of all NECB components between 8 June and 8 September are summarized in Fig. 6 and Table 1. Values with dominant systematic errors are expressed as ranges with an en-dash symbol, and values with dominant random errors are expressed with a plus-minus symbol.

During the 93 d period in 2014, the NECB accumulated to  $-17.6$  to  $-17.5 (\pm 1.2)$   $\text{g m}^{-2}$ . The vertical fluxes of  $F_{\text{CO}_2}$  and  $F_{\text{CH}_4}$  contributed  $-19.0 \pm 1.2$  and  $1.0 \pm 0.02$   $\text{g m}^{-2}$ , respectively, to the NECB, while the lateral fluxes of  $F_{\text{DIC}}$  and  $F_{\text{DOC}}$  contributed  $0.31$ – $0.38$  and  $0.06$ – $0.08$   $\text{g m}^{-2}$ , respectively, to the NECB. Thus, within the study period, lateral C fluxes exported 1.95%–2.42% of the net ecosystem exchange (lateral C flux / NEE), i.e., the net C uptake due to the balance of photosynthesis and respiration.

We also split these cumulative fluxes into mean weekly fluxes (Fig. 7a and b and Table 1). During the periodic spring flood that occurred in 2014 partially in the first week of June (2–7 June, Fig. 7a), high lateral DOC flux ( $13.0$ – $15.8$   $\text{mg m}^{-2} \text{d}^{-1}$ ) and  $\text{CH}_4$ -C flux ( $3.6 \pm 0.3$   $\text{mg m}^{-2} \text{d}^{-1}$ ) outpaced the  $\text{CO}_2$ -C uptake ( $-7.0 \pm 21.1$   $\text{mg m}^{-2} \text{d}^{-1}$ ) and indicates an ecosystem carbon source (positive NECB). During this period,  $F_{\text{DIC}}$  had not yet been observed. Therefore, the NECB is expected to be a stronger C source than presented in Fig. 7b.

From mid-June until the beginning of August, the negative NECB indicates that the ecosystem served as a carbon sink due to high levels of plant  $\text{CO}_2$  uptake. In August, the  $\text{CO}_2$  sink strength decreased (Fig. 7) and the mean daily  $\text{CO}_2$ -C flux turned from negative to positive. At the same time, vertical  $\text{CH}_4$  fluxes reached their maximum. Lateral DOC and DIC fluxes declined, and the ecosystem acted as a weak carbon sink with an NECB that also turned from negative to positive. During the 8 September days within the study period, all

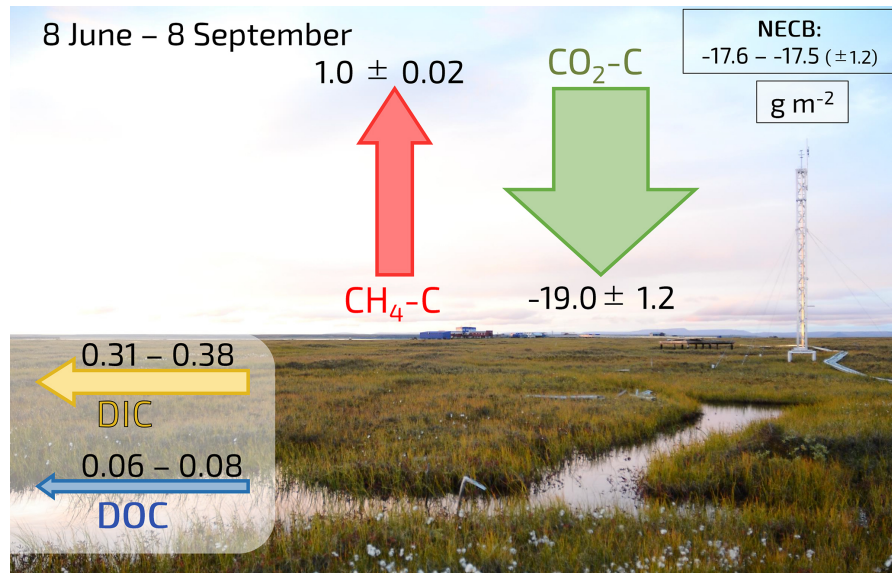


Figure 6: Schematic illustration of all four cumulative flux components of the NECB (DIC, DOC,  $\text{CH}_4\text{-C}$ , and  $\text{CO}_2\text{-C}$ ) in  $\text{g m}^{-2}$  during the study period in 2014. The NECB is shown in the top right corner. Uncertainties from systematic errors are denoted with an en dash (-), while uncertainties from random errors are indicated with the plus-minus symbol ( $\pm$ ). The picture in the background was taken on 30 August 2016 and provided by Jean-Louis Bonne.

fluxes acted as carbon sources. With a relative contribution of 97%, the  $\text{CO}_2\text{-C}$  emission dominated the NECB in September.

## A.5 DISCUSSION

### A.5.1 Comparison of DOC and DIC dynamics

We found a negative correlation between the water discharge rate and the DIC concentration (Fig. 5), meaning that higher water discharge rates dilute and decrease the DIC concentration. This result indicates that in other years, the DIC flux would not increase linearly with greater precipitation. The results by Öquist et al. (2014) show precipitation to be an important driver of interannual variability in lateral C flux dynamics. Our study period had comparatively normal summer precipitation rates. In other years with higher precipitation rates, we would expect to find a higher water discharge rate. However, based on our results, we do not expect a sharp rise in DIC flux to result from a higher water discharge rate. In one study, which focused on a catchment in northern Sweden, a tripling in water discharge rate increased the annual lateral  $^{14}\text{C}$  export by only 2% (Campeau et al., 2017). In contrast, in another study in northern Sweden, annual DIC export increased exponentially with rising water discharge rates (Öquist et al., 2014). Similarly to the DIC concentration, we also found

a negative correlation between the water discharge rate and the DOC concentration when neglecting the period during the spring flood. This finding suggests that higher discharge rates dilute and decrease the DOC concentration. Therefore, in seasons with higher discharge rates, the DOC flux would not rise linearly and the contribution of DOC export to the NECB probably would not rise. A similar correlation between DOC concentration and the water discharge rate has been reported in a tundra in a subarctic catchment (Olefeldt and Roulet, 2012). However, DOC export from polygonal tundra may increase if arctic climate change leads to accelerated degradation of ice wedges, which is expected to enhance drainage of the permafrost landscape (Liljedahl et al., 2016).

One unexpected finding was the relationship between DOC and DIC concentrations with a  $C_{\text{DIC}} / C_{\text{DOC}}$  ratio of  $4.31^{6.41}_{3.28}$  (median<sup>75th percentile</sup>, <sup>25th percentile</sup>). This ratio differs from those in other studies, which report a mean ratio of 0.65 from an Alaskan permafrost-affected watershed (Kling et al., 2000), a ratio of 0.24–1.30 in Canadian boreal biomes (Hutchins et al., 2019), and a ratio of 0.28 in a mixed coniferous forest in northern Sweden (Chi et al., 2020). However, one study reported a  $C_{\text{DIC}} / C_{\text{DOC}}$  ratio of up to 11.6 in an ice-rich permafrost catchment in northern Alaska (O'Donnell et al., 2019). A previous study at our study site found  $C_{\text{DIC}} / C_{\text{DOC}}$  ratios between 6.6 and 15.5 at the island's northern floodplain outlet in September 2008 (Abnizova et al., 2012), which are higher values than we present in this study, with a ratio of  $4.12^{4.42}_{3.82}$  in September 2014 (median<sup>75th percentile</sup>, <sup>25th percentile</sup>, not shown in the results). The high  $C_{\text{DIC}} / C_{\text{DOC}}$  ratio hints at effective degradation and mineralization of dissolved organic matter (DOM) in the surface waters of the studied catchment. Such effective degradation of DOM by photo-oxidation (Cory et al., 2015; Cory et al., 2014), microbial decomposition (e.g., Drake et al., 2015; Mann et al., 2015; Spencer et al., 2015), or both has been found and intensively studied in other arctic catchments. The studied polygonal tundra catchment is characterized by (1) a low relief and (2) mostly shallow waterbodies (depth < 1 m). Both factors enhance decomposition and mineralization of DOM: the low relief leads to long residence times of DOM before export, and the shallowness of the waterbodies allows for intense light exposure and photodegradation of DOM, which, in turn, may promote microbial mineralization (Cory et al., 2015).

#### A.5.2 *Net ecosystem carbon balance*

We estimated the NECB using the lateral C fluxes (DIC and DOC flux) and the vertical fluxes of  $\text{CO}_2$  and  $\text{CH}_4$ . Our results indicate that vertical  $\text{CO}_2$  uptake dominated the NECB during the study period. The lateral C fluxes exported only 1.95%–2.42% of the NEE. During the complete study period, we found the lateral C fluxes' contribution

to the NECB to be smaller than the uncertainty range of the observed CO<sub>2</sub> uptake. Nevertheless, our results also show that lateral carbon loss can exceed vertical carbon uptake at the beginning of the growing season. This finding shows that lateral C fluxes can play an essential role in the NECB during intensive water runoff periods, as we show in Fig. 7a.

The question remains whether the resulting relationship between lateral C fluxes and the NECB would be similar in the previous and following growing seasons. A previous study at the site of the instant study includes a 15-year record of eddy covariance CO<sub>2</sub> fluxes between 19 July and 23 August of each year (Holl et al., 2019b). It shows that CO<sub>2</sub> uptake in 2014 was among the lowest values in the 15-year record. In 12 other years, CO<sub>2</sub> uptake was stronger compared to the 2014 period. According to these data, we assume that the influence of lateral C fluxes on the NECB would have played an even less important role in many other years compared to 2014. In two studies from this site, researchers reported low but varying average CH<sub>4</sub>-C fluxes in two summer seasons: in the first study, the CH<sub>4</sub>-C fluxes vary between 7.5 mg m<sup>-2</sup> d<sup>-1</sup> (28 June–22 July 2004) and 17.3 mg m<sup>-2</sup> d<sup>-1</sup> (18–25 July 2003; Wille et al., 2008). In the second study, Beckebanze et al. (2022a) reported CH<sub>4</sub>-C fluxes of 12.55  $\overset{16.07}{\underset{9.65}{}}$  mg m<sup>-2</sup> d<sup>-1</sup> (median<sub>25th percentile</sub><sup>75th percentile</sup>, 11 July–10 September 2019). Thus, our CH<sub>4</sub>-C flux estimation of 10.6 mg m<sup>-2</sup> d<sup>-1</sup> in July 2014 lies within the range of estimates for other years. A study on DOC flux from a nearby island in the Lena River delta reports a mean daily flux of 1.2 mg m<sup>-2</sup> d<sup>-1</sup> in July and August 2013 (Stolpmann et al., 2022). This estimate is higher than our estimations of 0.42–0.51 mg m<sup>-2</sup> d<sup>-1</sup> in July 2014 but of the same order of magnitude compared to our estimates from June 2014 (1.51–1.83 mg m<sup>-2</sup> d<sup>-1</sup>). We also investigate the question of whether the measured EC flux would be representative of the entire catchment. Instruments at the EC tower were mounted at a height of 4.15 m, and the tower was located approximately 850 m southeast of the A outflows (see Fig. 22). The normalized mean contributions of four surface classes (based on the classification by Muster et al., 2012) within the footprint of the EC flux amounted to 66 % (dry tundra), 18 % (wet tundra), 8 % (overgrown water), and 7 % (water) in 2014 (Holl et al., 2019b). Within the entire catchment (maximum estimated extent), these four surface classes amounted to 63 % (dry tundra), 16 % (wet tundra), 9 % (overgrown water), and 11 % (open water; Muster et al., 2012). Therefore, the distribution of tundra surface classes within the footprint of the EC flux is similar to the distribution of tundra surface classes within the catchment and the observed EC fluxes can be considered representative of vertical fluxes for the entire catchment.

The question remains whether our study period between 8 June and 8 September covers all relevant flux contributions from the catchment.

At our study site, no large methane bursts have been observed during the soil-refreezing period in autumn as described by Mastepanov et al. (2013) for their arctic fen site in Greenland. For a dataset from 2003, Wille et al. (2008) show that mean daily methane emissions gradually go down between September and November. However, some peaks of higher methane emissions occur during stormy days during the refreezing period (probably triggered by turbulence-induced pressure pumping). These higher emissions during very windy conditions are only at maximum about 3 times higher than baseline emissions and, thus, much less than the methane flux peaks observed by Mastepanov et al. (2013). An article analyzing a long-term methane flux dataset from Samoylov Island, which includes data from several autumn refreezing periods and furthermore data from deep winter, is currently under revision (Rößger et al., 2022). This so far unpublished more extensive dataset also shows no large autumn methane bursts. However, the article estimates that about 14 % of the annual methane budget of the polygonal tundra is emitted during the refreezing period. Accounting for this additional emission would likely increase the relevance of CH<sub>4</sub> fluxes in an annual NECB.

In addition, the importance of lateral C fluxes could become more relevant with a longer observation period. Especially at the beginning of the study period, we observe high water discharge rates and high DOC concentration. Most likely, we do not cover the complete melting season with our study period; we clearly see in the data of outgoing shortwave radiation that the snowmelt started on 14 May. Relevant lateral C fluxes could have occurred directly at the beginning of the melting period, as has been observed in a *palsa* and a bog in northern Sweden (Olefeldt and Roulet, 2012). However, one could also argue that the observed high lateral C fluxes at the beginning of the study period should not be included in the NECB. These high lateral C fluxes are likely linked to C-bearing river water which flooded the catchment before the observations started and drained through the catchments' outflows at the beginning of the observation period. In the course of the observation period, the origin of dissolved C in the observed lateral runoff might shift from allochthonous to autochthonous sources. Due to the unknown characteristics of this possible shift in sources for dissolved carbon, we included all available lateral C flux observations in the NECB estimation. This inclusion of lateral C fluxes that are likely not part of the catchments' NECB increases the relevance of lateral C fluxes in the NECB estimation. Because we potentially overestimated the impact of lateral C export on the NECB, our conclusion of a very limited role of dissolved carbon appears to be an understatement – lateral C export likely plays an even smaller role.

If we were to include the lateral C fluxes between 14 May and 2 June and assume that the DOC flux at our site would show a similar pattern to the DOC flux in Olefeldt and Roulet (2012) (74 % of DOC

flux during snowmelt), we would have a max annual DOC flux of  $0.21 \text{ g m}^{-2}$ . From DIC flux we would only expect a low contribution during the snowmelt due to likely high water discharge rates during the snowmelt and the negative correlation between DIC concentration and water discharge rate. Therefore, the inclusion of possible snowmelt DOC flux and DIC flux would change the absolute numbers of these fluxes but likely not change our conclusion regarding the influence of DOC flux or DIC flux on the NECB.

Due to the multitude of flux components, some simplifications were applied and the uncertainty in the NECB was not quantified to its full extent. Most uncertainties have been described in Sect. A.3.9 and have been accounted for; however, more uncertainties might also arise from missing observations or gap-filling approaches. This study, for example, discounts the contributions of particulate organic carbon (POC) since we only found small differences between filtered (average  $6.01 \text{ mg L}^{-1}$ ) and unfiltered water samples (average  $6.07 \text{ mg L}^{-1}$ ) with respect to total carbon content. Thus, we suggest that POC would contribute only very little to the lateral C flux and therefore to the NECB. In this study we also include a gap-filled time series of the DIC concentration in the estimation of the NECB (see Sect. A.3.4). We assessed an agreement between the observed data and the independent testing subset as  $R_{\text{adj}}^2 = 0.79$ . Therefore, this approach could increase the random uncertainty during the gap-filled period. However, the large potential bias of the catchment assessment dominated the uncertainty in  $F_{\text{DIC}}$  and the random uncertainty in the DIC concentration played only a minor role. Overall, we assume that these additional uncertainties do not significantly change the results of the estimated NECB and therefore also not the conclusion of this study.

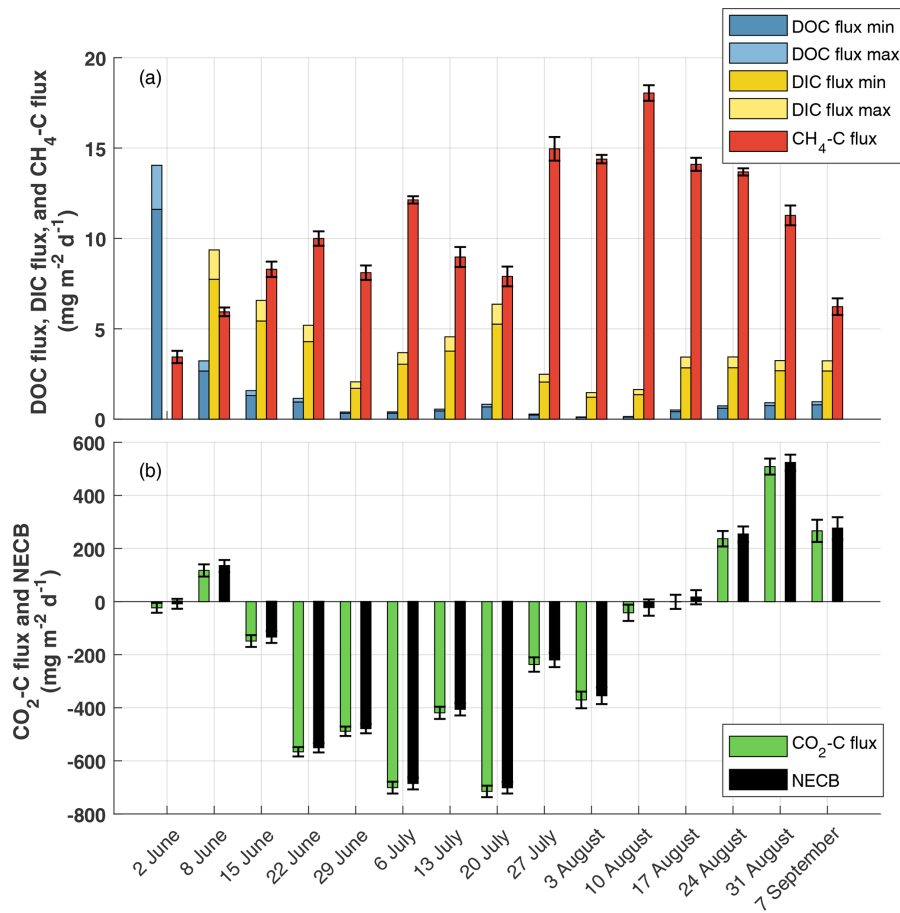


Figure 7: Seasonal development of NECB components as mean daily fluxes from 2 June (week 1) to 8 September (week 15). **(a)** Minor components of NECB: DOC flux (blue), DIC flux (yellow), and CH<sub>4</sub>-C flux (red); **(b)** Major component of NECB: CO<sub>2</sub>-C flux (green) and the resulting NECB (black). Please note the different values of the y axis in **(a)** and **(b)**. Uncertainties from systematic errors are denoted with a second bar in a brighter color, while uncertainties from random errors are indicated with an error bar. The systematic uncertainty in the NECB is shown but not visible due to its small value.

## A.6 CONCLUSIONS

At the polygonal tundra site in the Arctic Lena River delta, which we investigated for this study, the net ecosystem carbon balance was periodically dominated by laterally exported dissolved carbon. The relative impact of these waterborne carbon losses on the total net ecosystem carbon balance was particularly high in the early and late growing season. During the Lena River spring flood, the largest amounts of dissolved organic carbon in absolute and relative terms were exported. In the late vegetation period, the relatively high impact of lateral C fluxes can largely be explained by low net ecosystem exchange rates of carbon dioxide due to generally diminished plant activity. During the seasons when soils are refreezing (October–November) or completely frozen (December–May), water discharge and consequently lateral C export cease. Therefore, we conclude that lateral C export is even less important for the annual NECB than for the growing-season NECB.

The contribution of lateral C fluxes to the cumulative NECB decreased on Samoylov Island over the growing season and was, in contrast to temperate and boreal ecosystems, negligible compared to cumulative vertical growing-season carbon fluxes. We therefore conclude that the NECB of a polygonal tundra landscape is sufficiently described when only vertical flux measurements are performed. Only studies which describe short-term tundra C balances should take lateral C export into account, particularly during or immediately following snowmelt. Furthermore, in regions with rapid landscape degradation, lateral C fluxes could play a different, more relevant role in an ecosystem's carbon balance.

## A.7 APPENDIX

### A.7.1 *DOC concentration from a spectrometer probe*

We used a multiple stepwise regression (MSR) model (following Draper and Smith, 2014) to estimate  $C_{\text{DOC}}$  from a spectrometer probe in order to obtain a longer time series of  $C_{\text{DOC}}$  compared to the time series from the TOC analyzer. We compared the  $C_{\text{DOC}}$  analyzed in the TOC analyzer with the absorbance bands from a spectrometer probe to find suitable absorbance bands to describe the DOC concentration. The spectrometer probe measured the absorbance ( $a_{\lambda}$ ) of the sampled water probe between the 200 and 740 nm wavelength ( $\lambda$ ) in 2.5 nm steps. In this analysis, we focused on the commonly used absorbance values between 250 and 740 nm as well as Ratio 1 ( $a_{465}/a_{665}$ ) and Ratio 2 ( $a_{255}/a_{365}$ ). Absorbance values below 250 nm were neglected due to possible interference with inorganic substances, following Avagyan et al. (2014). For the application of the MSR model, we split the dataset of  $C_{\text{DOC}}$  from the TOC analyzer and the absorbance values

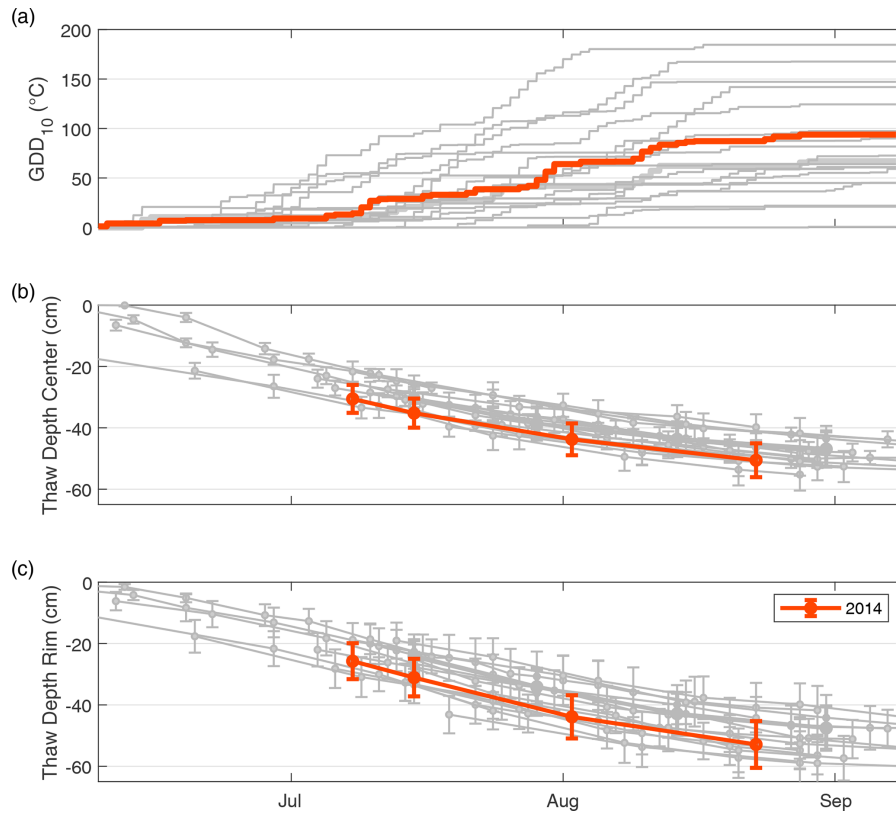


Figure 8: Cumulative growing degree days (GDDs; **a**) and thaw depths in the center (**b**) and the rim (**c**) of a polygon between 8 June and 8 September of 2002–2018. The year 2014 is highlighted in orange. All other years are displayed in gray.

from the spectrometer probe into training (75 %) and validation (25 %) sets. Details on the application of the MSR can be found in Avagyan et al. (2014). We applied the MSR model in MATLAB R2019b using the `stepwisefit` function.

We used the following wavelengths and ratios as predictors for the DOC concentration at the three outflows: 250 nm and Ratio 2 at outflow A<sub>1</sub>; 250, 300, and 722.5 nm at outflow A<sub>2</sub>; and 250, 690, and 712.5 nm at outflow B. In Fig. 10, the validation set of  $C_{\text{DOC}}$  from the TOC analyzer and the spectrometer probe are shown.

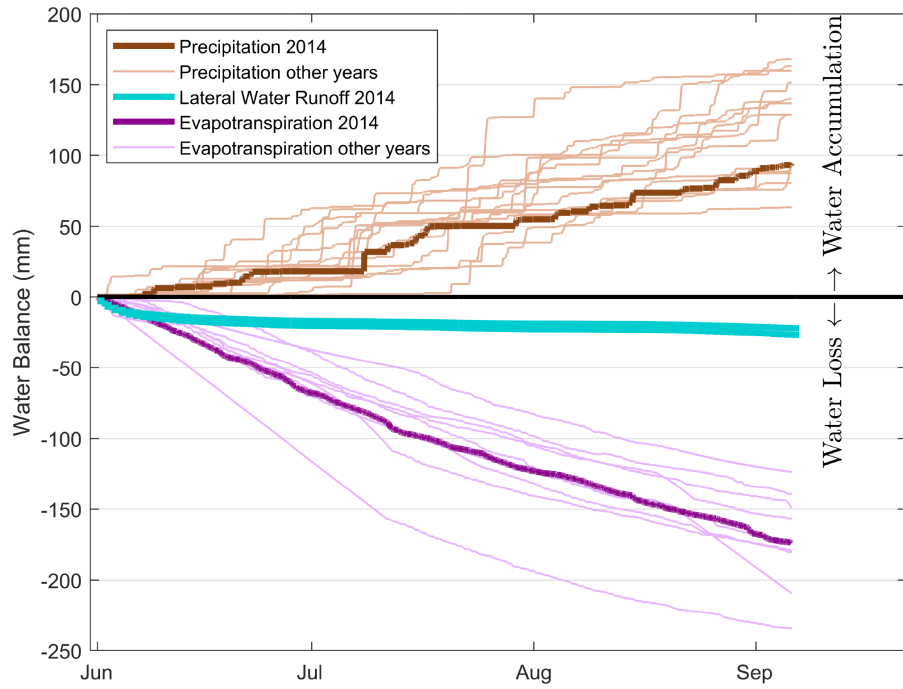


Figure 9: Water balance at the study site between 2 June and 8 September 2014 with cumulative precipitation amounts above zero and cumulative evapotranspiration and the water runoff rate below zero. Cumulative precipitation and evapotranspiration for the years 1998–2018 and 2007–2018, respectively, are shown in lighter colors (with the exception of 2014, which is shown in darker colors).

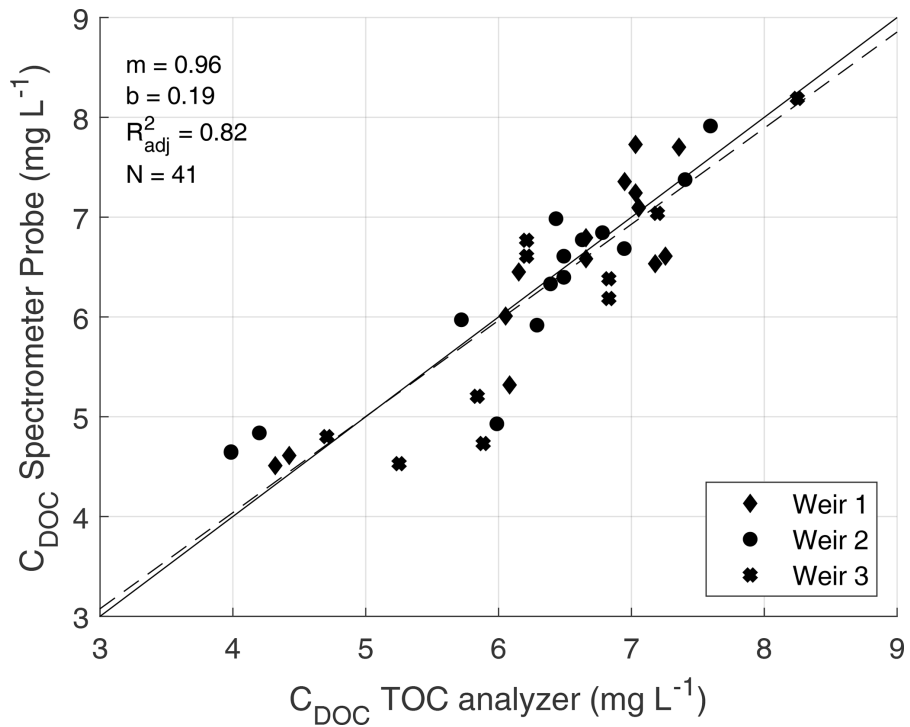


Figure 10: Validation set of  $C_{\text{DOC}}$  from the TOC analyzer and the spectrometer probe with the corresponding linear regression (dashed line). The solid line represents the 1 : 1 line.

Table 1: Mean daily flux components for each week (first 15 rows) and cumulative flux components (last row) of the NECB ( $\text{CO}_2\text{-C}$ ,  $\text{CH}_4\text{-C}$ , DIC, and DOC) during the measurement period in 2014. Uncertainties from systematic errors are shown with an en dash (-), and uncertainties from random errors are denoted by the plus-minus symbol ( $\pm$ ).

	NECB	Vert $\text{CO}_2\text{-C}$ flux	Vert $\text{CH}_4\text{-C}$ flux	DIC flux	DOC flux	Unit
2-7 June	9.6-12.3 ( $\pm 21$ )	-7.0 $\pm$ 21.1	3.6 $\pm$ 0.3	-	13.0-15.8	$\text{mg m}^{-2} \text{d}^{-1}$
8-14 June	134-136 ( $\pm 23$ )	117.3 $\pm$ 23.0	5.94 $\pm$ 0.24	7.74-9.37	2.67-3.23	$\text{mg m}^{-2} \text{d}^{-1}$
15-21 June	-134 to -132 ( $\pm 22$ )	-148.5 $\pm$ 22.2	8.29 $\pm$ 0.43	5.43-6.57	1.31-1.58	$\text{mg m}^{-2} \text{d}^{-1}$
22-28 June	-551 to -550 ( $\pm 18$ )	-565.9 $\pm$ 17.6	10.00 $\pm$ 0.40	4.30-5.20	0.95-1.15	$\text{mg m}^{-2} \text{d}^{-1}$
29 June-5 July	-478 to -478 ( $\pm 18$ )	-488.6 $\pm$ 17.8	8.10 $\pm$ 0.40	1.71-2.07	0.33-0.40	$\text{mg m}^{-2} \text{d}^{-1}$
6-12 July	-685 to -684 ( $\pm 22$ )	-700.8 $\pm$ 22.3	12.13 $\pm$ 0.20	3.04-3.68	0.33-0.40	$\text{mg m}^{-2} \text{d}^{-1}$
13-19 July	-406 to -405 ( $\pm 23$ )	-419.1 $\pm$ 23.0	8.97 $\pm$ 0.55	3.77-4.56	0.46-0.56	$\text{mg m}^{-2} \text{d}^{-1}$
20-26 July	-701 to -700 ( $\pm 22$ )	-715.1 $\pm$ 21.7	7.90 $\pm$ 0.55	5.26-6.36	0.68-0.82	$\text{mg m}^{-2} \text{d}^{-1}$
27 July-2 August	-220 to -219 ( $\pm 27$ )	-237.1 $\pm$ 27.1	14.96 $\pm$ 0.65	2.06-2.49	0.23-0.28	$\text{mg m}^{-2} \text{d}^{-1}$
3-9 August	-355 to -354 ( $\pm 31$ )	-370.5 $\pm$ 31.3	14.39 $\pm$ 0.23	1.22-1.47	0.10-0.13	$\text{mg m}^{-2} \text{d}^{-1}$
10-16 August	-23 to -22 ( $\pm 31$ )	-42.2 $\pm$ 30.7	18.05 $\pm$ 0.43	1.36-1.64	0.12-0.15	$\text{mg m}^{-2} \text{d}^{-1}$
17-23 August	16-17 ( $\pm 27$ )	-1.0 $\pm$ 26.6	14.10 $\pm$ 0.36	2.84-3.44	0.42-0.51	$\text{mg m}^{-2} \text{d}^{-1}$
24-30 August	253-255 ( $\pm 29$ )	236.7 $\pm$ 29.1	13.68 $\pm$ 0.20	2.85-3.44	0.61-0.74	$\text{mg m}^{-2} \text{d}^{-1}$
31 August-6 September	523-524 ( $\pm 30$ )	508.6 $\pm$ 30.2	11.27 $\pm$ 0.55	2.68-3.24	0.75-0.91	$\text{mg m}^{-2} \text{d}^{-1}$
7-8 September	276-277 ( $\pm 42$ )	266.4 $\pm$ 41.8	6.23 $\pm$ 0.46	2.67-3.23	0.80-0.96	$\text{mg m}^{-2} \text{d}^{-1}$
Season sum	-17.6 to -17.5 ( $\pm 1.2$ )	-19.0 $\pm$ 1.2	1.0 $\pm$ 0.02	0.31-0.38	0.06-0.08	$\text{g m}^{-2}$
(8 June-8 September)						

## A.8 MANUSCRIPT INFORMATION

*Code and data availability*

The dataset of this study is published at PANGAEA (<https://doi.org/10.1594/PANGAEA.944186>) (Beckebanze et al., 2022b).

*Authors contribution*

BRKR, CW, and LK designed the experiments, and BRKR, CW, DH, and LK carried out the fieldwork. BRKR, JW, LB, and LK developed the idea for the analysis, and CW provided processed eddy covariance data. The formal analysis and data visualization were done by LB. DH and LK supervised this. LK, JB, and TS provided resources for the instrumentation. LB prepared the manuscript with contributions from all co-authors.

*Competing interests*

The contact author has declared that none of the authors has any competing interests.

*Disclaimer*

Publisher's note: Copernicus Publications remains neutral with regard to jurisdictional claims in published maps and institutional affiliations.

*Acknowledgements*

We would like to thank the members of the Russian–German field campaign LENA 2014, especially Sandra Petersen (Universität Hamburg) for sampling analysis and the crew of the Russian research station Samoylov for logistical as well as technical support. We are grateful to Tim Eckhardt and Leonardo de Aro Galera for valuable discussions about the data analysis and the manuscript and Sarah Wiesner for being a great support as a PhD advisory panel chair (all at the Universität Hamburg). We also thank Jean-Louis Bonne (Université de Reims Champagne-Ardenne) for allowing us to use the picture of the polygonal tundra.

*Financial support*

This study was funded by the Deutsche Forschungsgemeinschaft (DFG, German Research Foundation) under Germany's Excellence Strategy – EXC 2037 “CLICCS – Climate, Climatic Change, and Society” – project

number 390683824, contribution to the Center for Earth System Research and Sustainability (CEN) of Universität Hamburg. Long-term measurements of CO<sub>2</sub> and CH<sub>4</sub> fluxes were supported by the projects “CarboPerm” (grant no. 03G0836A) and “KoPf” (grant no. 03F0764A), both funded by the German Federal Ministry of Education and Research (BMBF). Torsten Sachs and Christian Wille were supported by the Helmholtz Association of German Research Centres through a Helmholtz Young Investigators Group grant to Torsten Sachs (grant no. VH-NG-821).

*Review statement*

This paper was edited by Kees Jan van Groenigen and reviewed by two anonymous referees.



## IGNORING CARBON EMISSIONS FROM THERMOKARST PONDS RESULTS IN OVERESTIMATION OF TUNDRA NET CARBON UPTAKE

---

Lutz Beckebanze<sup>1,2,\*</sup>, Zoé Rehder<sup>3,4,\*</sup>, David Holl<sup>1,2</sup>, Christian Wille<sup>5</sup>, Charlotta Mirbach<sup>1,2</sup>, Lars Kutzbach<sup>1,2</sup>

<sup>1</sup>Institute of Soil Science, Universität Hamburg, Germany

<sup>2</sup>Center for Earth System Research and Sustainability (CEN), Universität Hamburg, Germany

<sup>3</sup>Department of the Land in the Earth System, Max Planck Institute for Meteorology, Hamburg, Germany

<sup>4</sup>International Max Planck Research School on Earth System Modeling, Hamburg, Germany

<sup>5</sup>Helmholtz-Zentrum Potsdam – Deutsches Geo Forschungs Zentrum (GFZ), Potsdam, Germany

\*These authors contributed equally to this work.

This chapter is published in Biogeosciences under the DOI <https://doi.org/10.5194/bg-19-1225-2022>

### B.1 ABSTRACT

Arctic permafrost landscapes have functioned as a global carbon sink for millennia. These landscapes are very heterogeneous, and the omnipresent water bodies within them act as a carbon source. Yet, few studies have focused on the impact of these water bodies on the landscape carbon budget. We deepen our understanding of carbon emissions from thermokarst ponds and constrain their impact by comparing carbon dioxide and methane fluxes from these ponds to fluxes from the surrounding tundra. We use eddy covariance measurements from a tower located at the border between a large pond and semi-terrestrial tundra.

When we take the open-water areas of thermokarst ponds into account, our results show that the estimated summer carbon uptake of the polygonal tundra is 11 % lower. Further, the data show that open-water methane emissions are of a similar magnitude to polygonal tundra emissions. However, some parts of the pond's shoreline exhibit much higher emissions. This finding underlines the high spatial variability in methane emissions. We conclude that gas fluxes from thermokarst ponds can contribute significantly to the carbon budget

of Arctic tundra landscapes. Consequently, changes in the water body distribution of tundra landscapes due to permafrost degradation may substantially impact the overall carbon budget of the Arctic.

## B.2 INTRODUCTION

Water bodies make up a significant part of the Arctic lowlands with an areal coverage of about 17% (Muster et al., 2017) and act as an important carbon source in a landscape that is an overall carbon sink (Kuhn et al., 2018). Intensified permafrost thaw in the warming Arctic will change the distribution of water bodies and thereby change their contribution (Andresen and Loughheed, 2015; Bring et al., 2016) to the landscape carbon budget (Kuhn et al., 2018) of tundra landscapes. However, data on greenhouse gas emissions from Arctic water bodies are still sparse, especially data with a high temporal resolution and from non-Yedoma regions (Vonk et al., 2015).

Our study site in the Lena River delta, Siberia, is located on an island mostly characterized by non-Yedoma polygonal tundra (Fig. 11). This landscape features many ponds; we define ponds as water bodies with an area of less than  $8 \times 10^4 \text{ m}^2$ , following Ramsar Convention Secretariat (2016) and Rehder et al. (2021). Within our area of interest, ponds cover about the same area as lakes (Abnizova et al., 2012; Muster et al., 2012). The ponds on Samoylov Island have formed almost exclusively through thermokarst processes: the soil has a high ice content, so when the ice melts, the ground subsides, and thermokarst ponds form (Ellis et al., 2008). These thermokarst ponds are often only as large as one polygon (polygonal ponds). When several polygons are inundated, this can cause larger shallow thermokarst ponds to form, which we term merged polygonal ponds (Rehder et al., 2021). Holgerson and Raymond (2016) as well as Wik et al. (2016) report that ponds emit more greenhouse gases per unit area than lakes, defined here as water bodies with an area larger than  $8 \times 10^4 \text{ m}^2$ . Thus, in our study area, they have greater potential than lakes to counterbalance the carbon uptake of the surrounding tundra (Jammet et al., 2017; Kuhn et al., 2018; McGuire et al., 2012). To better understand the impact of thermokarst ponds on the landscape carbon flux, we compare carbon dioxide ( $\text{CO}_2$ ) and methane ( $\text{CH}_4$ ) fluxes from thermokarst ponds to fluxes from the semi-terrestrial tundra. The semi-terrestrial tundra consists of wet and dry tundra and overgrown shallow water, which are the terrestrial land-surface types used by Muster et al. (2012) to classify Samoylov Island.

The main geophysical and biochemical processes that drive  $\text{CH}_4$  fluxes are different to the ones that drive  $\text{CO}_2$  fluxes. The microbial decomposition of dissolved organic carbon, which is introduced laterally into the aquatic system through rain and meltwater (Neff and Asner, 2001), dominates aquatic  $\text{CO}_2$  production. When supersaturated with

dissolved CO<sub>2</sub>, ponds emit CO<sub>2</sub> into the atmosphere through diffusion. While photosynthetic CO<sub>2</sub> uptake has been observed in some clear Arctic water bodies (Squires and Lesack, 2003), most Arctic water bodies are net CO<sub>2</sub> sources (Kuhn et al., 2018). Estimates of CO<sub>2</sub> emissions range from close to zero (0.028 g m<sup>2</sup> d<sup>-1</sup> by Treat et al., 2018, and 0.059 g m<sup>2</sup> d<sup>-1</sup> by Jammet et al., 2017) to substantial (1.4–2.2 g m<sup>2</sup> d<sup>-1</sup> by Abnizova et al., 2012).

Within just one site, CH<sub>4</sub> emissions from a water body can vary by up to 5 orders of magnitude: 0.5–6432 mg m<sup>2</sup> d<sup>-1</sup> (Bouchard et al., 2015). The CH<sub>4</sub> that ponds emit is mostly produced in sub-aquatic soils and anoxic bottom waters (Borrel et al., 2011; Conrad, 1999; Hedderich and Whitman, 2006). Additionally, CH<sub>4</sub> might also be produced in the oxic water column (Bogard et al., 2014; Donis et al., 2017), though this location of methanogenesis is only significant in large water bodies (Günthel et al., 2020). Moreover, there is still ongoing debate as to whether methanogenesis occurs in oxic waters at all (Encinas Fernández et al., 2016; Peeters et al., 2019). CO<sub>2</sub> is also formed as a byproduct of the methanogenesis process (Hedderich and Whitman, 2006). Water bodies emit CH<sub>4</sub> produced in their benthic zone through diffusion, ebullition (sudden release of bubbles), or plant-mediated transport. The varying contributions of these three local methane emissions pathways lead to high spatial variability between water bodies and within a single water body (Jansen et al., 2019; Sepulveda-Jauregui et al., 2015). In particular, local seep ebullition causes high spatial variance of CH<sub>4</sub> emissions within one water body (Walter et al., 2006). Variability in the coverage and composition of vascular plant communities in a water body can also increase CH<sub>4</sub> variability because CH<sub>4</sub> transport efficiency can be species-specific (Andresen et al., 2017; Knoblauch et al., 2015).

To study spatial and temporal patterns of carbon emissions from thermokarst ponds, we analyzed land–atmosphere CO<sub>2</sub> and CH<sub>4</sub> flux observations from an eddy covariance (EC) tower on Samoylov Island, Lena River delta, Russia. We set up the EC tower within the polygonal tundra landscape at the border between a large merged polygonal pond and the surrounding semi-terrestrial tundra for 2 months in summer 2019. The polygonal structures were still clearly visible along the shore and underwater, and most of the pond was shallow (Rehder et al., 2021). Due to the tower’s position, fluxes from the merged polygonal pond were the dominant source of the observed EC fluxes under easterly winds. From other wind directions, the observed EC fluxes were dominated by semi-terrestrial polygonal tundra with only a low influence from small polygonal ponds. This paper aims to deepen the understanding of carbon emissions from thermokarst ponds and constrain their impact on the landscape carbon balance. We (1) examine the temporal and spatial patterns of net ecosystem exchange (NEE) and the spatial pattern of CH<sub>4</sub> flux from semi-terrestrial tun-

dra and thermokarst ponds and (2) investigate the influence of the thermokarst ponds on the landscape NEE of CO<sub>2</sub> during the months June to September 2019. To this end, we use a footprint model and model NEE of CO<sub>2</sub> using the footprint weights of semi-terrestrial tundra and thermokarst ponds.

### B.3 METHODS

#### B.3.1 *Study site*

Samoylov Island (72°22' N, 126°28' E) is located in the southern part of the Lena River delta (Fig. 11b). It is approximately 5 km<sup>2</sup> in size and consists of two geomorphologically different components. The western part of the island (~2 km<sup>2</sup>) is a floodplain, which is flooded annually during the spring. The eastern part of the island (~3 km<sup>2</sup>), a Late Holocene river terrace, is characterized by polygonal tundra. The partially degraded polygonal tundra at this study site features high spatial heterogeneity on a scale of a few meters in several aspects, including vegetation, water table height, and soil properties. Dry and wet vegetated parts of the semi-terrestrial tundra are interspersed with small and large thermokarst ponds (1 to 10 000 m<sup>2</sup>) and with larger lakes (up to 0.05 km<sup>2</sup>; Boike et al., 2015c; Kartoziia, 2019). The island is surrounded by the Lena River and sandy floodplains, creating additional spatial heterogeneity on a larger scale.

This study focuses on a merged polygonal pond (Figs. 11d and 17) on the eastern part of the island. This merged polygonal pond has a size of 0.024 km<sup>2</sup> with a maximum depth of 3.4 m and a mean depth of 1.2 m (Boike et al., 2015c; Rehder et al., 2021). In an aerial image of the pond, the polygonal structures are clearly visible under the water's surface (Boike et al., 2015b). The vegetated shoreline of this merged polygonal pond is dominated by *Carex aquatilis*, but it also features *Carex chordorrhiza*, *Potentilla palustris*, and *Aulacomnium* spp. These plants grow in the water near the shore, while the deeper parts of the merged polygonal pond are vegetation-free.

#### B.3.2 *Instruments*

We measured gas fluxes using an eddy covariance (EC) tower between 11 July and 10 September 2019. The EC tower was located on the eastern part of Samoylov Island, directly on the western shore of the merged polygonal pond (Fig. 11d). The EC instruments were mounted on a tripod at a height of 2.25 m (Fig. 17). The tower was equipped with an enclosed-path CO<sub>2</sub>-H<sub>2</sub>O sensor (LI-7200, LI-COR Biosciences, USA), an open-path CH<sub>4</sub> sensor (LI-7700, LI-COR Biosciences, USA), and a 3D ultrasonic anemometer (R3-50, Gill Instruments Limited, UK). All instruments had a sampling rate of 20 Hz. We also installed

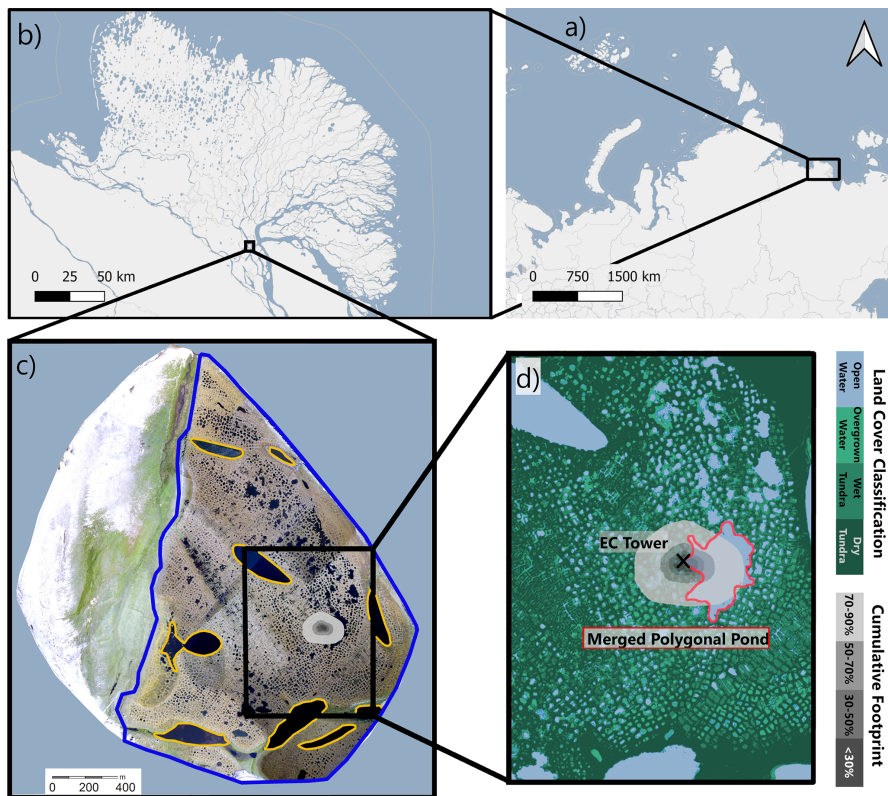


Figure 11: The location of the study site in Russia is shown in (a), and the location of Samoylov Island within the Lena River delta is shown in (b). Samoylov Island is shown in (c); the surrounding Lena River appears in light blue. The outline of the river terrace land-cover classification (Sect. B.3.4.1) is indicated by the blue line. We focus on the polygonal tundra; however, large lakes are excluded (circled in yellow). In (d), the land-cover classification is drawn in blue (open water) and green (dark green: dry tundra; medium green: wet tundra; light green: overgrown water) shades. The merged polygonal pond studied here is outlined in red. The location of the EC tower is marked by a black cross. The cumulative footprint (see Sect. B.3.4.2) is shown in gray shades. Of the flux, 30 % likely originated from within the dark gray area, 50 % from within the medium dark gray area, 70 % from within the medium light gray area, and 90 % from within the light gray area. Map data from © OpenStreetMap contributors 2020, distributed under the Open Data Commons Open Database License (ODbL) v1.0 (a, b) and modified based on Boike et al. (2012b) (c, d).

radiation-shielded temperature and humidity sensors at the EC tower (HMP155, Vaisala, Finland) and used data from a photosynthetically active radiation (PAR) sensor mounted on a tower approximately 500 m to the west of the EC tower (SKP 215, Skye Instruments, UK). Additional meteorological data for Samoylov Island were provided by Boike et al. (2019).

### B.3.3 Data processing

We performed the raw data processing and computation of half-hourly fluxes for open-path and enclosed-path fluxes ( $\text{CO}_2$ ,  $\text{CH}_4$ , and  $\text{H}_2\text{O}$ ) using EddyPro 7.0.6 (LI-COR, 2019). The convention of this software is that positive fluxes are fluxes from the surface to the atmosphere, while negative fluxes indicate a flux from the atmosphere downwards. Raw data screening included spike detection and removal according to Vickers and Mahrt (1997) (1 % maximum accepted spikes and a maximum of three consecutive outliers). Additionally, we applied statistical tests for raw data screening, including tests for amplitude resolution, skewness and kurtosis, discontinuities, angle of attack, and horizontal wind steadiness. All of these tests' parameters were set to EddyPro default values. We rotated the wind-speed axis to a zero-mean vertical wind speed using the "double rotation" method of Kaimal and Finnigan (1994). Further, we applied linear de-trending to the raw data following Gash and Culf (1996) before performing flux calculations. We compensated for time lags via automatic time lag optimization using a time lag assessment file from a previous EddyPro run. In this previous time lag assessment, the time lags for all gases were detected using covariance maximization (Fan et al., 1990), resulting in time lags between 0 and 0.4 s for  $\text{CO}_2$  and between  $-0.5$  and  $+0.5$  s for  $\text{CH}_4$ . For  $\text{H}_2\text{O}$ , the time lag was humidity-dependent and was calculated for 10 humidity classes. We compensated for air-density fluctuations due to thermal expansion and contraction and varying water-vapor concentrations, following Webb et al. (1980). This correction depends on accurate measurements of the latent and sensible heat flux and was applied to the open-path data of the LI-7700. For the LI-7700 in particular, the correction term can be larger than the flux itself, but the correction was derived from the underlying physical equations. Because we used well-calibrated instruments as well as EddyPro, which uses an up-to-date implementation of the correction, we were confident that the LI-7700 would provide accurate  $\text{CH}_4$  flux estimates. For enclosed-path data, we performed a sample-by-sample conversion into mixing ratios to account for air-density fluctuations (Burba et al., 2012; Ibrom et al., 2007b). Flux losses occurred in the low- and high-frequency spectral range due to different filtering effects. We compensated for flux losses in the low-frequency range in accordance with Moncrieff et al. (2004) and in the high-frequency range in accordance with Fratini et al. (2012). For the high-frequency range compensation method, a spectral assessment file was created using the method of Ibrom et al. (2007a). The spectral assessment resulted in cutoff frequencies of 3.05 and 1.67 Hz for  $\text{CO}_2$  and  $\text{CH}_4$ , respectively. For  $\text{H}_2\text{O}$ , we found a humidity-dependent cutoff frequency between 1.25 Hz (relative humidity, RH, of 5 %–45 %) and 0.21 Hz (RH 75 %–95 %). We performed a quality check on each half-hourly flux

following the 0–1–2 system proposed by Mauder and Foken (2004). In this quality check, flux intervals with the lowest quality received the flag “2” and were excluded from further analysis.

#### B.3.4 Data analysis

##### B.3.4.1 Land-cover classification

The land-cover classification covers the Late Holocene river terrace of Samoylov Island (3.0 km<sup>2</sup>, area within the blue line in Fig. 11c). It is based on high-resolution near-infrared (NIR) orthomosaic aerial imagery obtained in the summer of 2008 (Boike et al., 2015a). We used a subset of the existing classification of Muster et al. (2012) as a training dataset to perform semi-supervised land-cover classification using the *maximum likelihood algorithm* in ArcMap Version 10.8 (Esri Inc., USA). We then applied the ArcMap *majority filter* tool to the new classification. The land-cover classification has a resolution of 0.17 m × 0.17 m. It is projected onto WGS 84 UTM Zone 52N, and the land-cover classes include *open water* (15.7%), *overgrown water* (7.0%), *dry tundra* (65.1%), and *wet tundra* (12.1%), as defined by Muster et al. (2012). We summarize the classes overgrown water, dry tundra, and wet tundra in the land-cover type of semi-terrestrial tundra. The river terrace consists of this semi-terrestrial tundra, large lakes, and thermokarst ponds. Since small ponds are an integral part of the polygonal tundra, we use the term “polygonal tundra” to refer to the area of the river terrace covered by semi-terrestrial tundra and by thermokarst ponds.

##### B.3.4.2 Footprint model

In deploying an EC measurement tower, the tower’s location and sensor height are crucial parameters. A lower measurement height results in a smaller footprint. The tower’s footprint describes the source area of the flux within the surrounding landscape. As we installed sensors at a height of 2.25 m next to the merged polygonal pond, we expected to observe substantial flux signals from the adjacent water body as well as from the surrounding semi-terrestrial tundra. Each land-cover type’s contribution to the flux signal depended on the wind direction and turbulence characteristics. We implemented the analytical footprint model proposed by Kormann and Meixner (2001) in MATLAB (2019). We combined the footprint model with land-cover classification data described in Sect. B.3.4.1 to estimate the contribution of each land-cover type to each half-hourly flux (from now on referred to as the weighted footprint fraction). The model accounted for the stratification of the atmospheric boundary layer and required a height-independent crosswind distribution and horizontal

homogeneity of the surface. The input data required stationarity of atmospheric conditions during the flux intervals of 30 min.

We derived the vertical power-law profiles for the eddy diffusivity and the wind speed for each 30 min flux depending on the atmospheric stratification (see Eq. 6 in Kormann and Meixner, 2001). We used an analytical approach to find the closest Monin–Obukhov (M–O) similarity profile (see Eq. 36 in Kormann and Meixner, 2001). Next, we calculated a two-dimensional probability density function of the source area for each flux (from Eqs. 9 and 21 in Kormann and Meixner, 2001). We combined each probability density function with the land-cover classification of Samoylov Island’s river terrace with its four land-cover types (see Sect. B.3.4.1). The resolution of the footprint model was set to the land-cover classification resolution of  $0.17\text{ m} \times 0.17\text{ m}$ . Hence, we were able to estimate how much a given grid cell contributed to each 30 min flux. We also knew each grid cell’s dominant land-cover type from the land-cover classification. We combined both pieces of information for each grid cell and calculated the sum of the fraction fluxes within the source area for each of the four land-cover types (dry tundra, wet tundra, overgrown water, and open water) and determined the contribution of each land-cover type with respect to each 30 min flux ( $\alpha_{\text{dry tundra}}$ ,  $\alpha_{\text{wet tundra}}$ ,  $\alpha_{\text{overgrown water}}$ , and  $\alpha_{\text{open water}}$ ). We refer to this contribution of each land-cover type as the *weighted footprint fraction*.

We also summed all 30 min two-dimensional probability density functions over the entire deployment time. This sum is referred to as the cumulative footprint (gray-shaded area in Fig. 11c–d).

#### B.3.4.3 Gap-filling the $\text{CO}_2$ flux

To gap fill the net ecosystem exchange (NEE) fluxes of  $\text{CO}_2$ , we used the *bulk-NEE model* proposed by Runkle et al. (2013). The model is specifically designed to model NEE in Arctic regions: it takes impacts of the polar day into account by allowing both respiration and photosynthesis to occur simultaneously throughout the day. The bulk-NEE model uses the sum of total ecosystem respiration (TER) and gross primary production (GPP) to describe NEE, our target variable:

$$\text{NEE} = \text{TER} + \text{GPP}, \quad (1)$$

where TER and GPP are in units of  $\mu\text{mol m}^{-2} \text{s}^{-1}$ . TER is approximated as an exponential function of air temperature  $T_{\text{air}}$ :

$$\text{TER} = R_{\text{base}} \cdot Q_{10}^{\frac{T_{\text{air}} - T_{\text{ref}}}{10}}, \quad (2)$$

where  $T_{\text{ref}} = 15^\circ\text{C}$  and  $\gamma = 10^\circ\text{C}$  are constant, independent parameters.  $R_{\text{base}}$  ( $\mu\text{mol m}^{-2} \text{s}^{-1}$ ) describes the basal respiration at the reference temperature  $T_{\text{ref}}$ , and  $Q_{10}$  (dimensionless) describes the sensitivity of ecosystem respiration to air temperature changes.

GPP is described as a rectangular hyperbolic function of PAR ( $\mu\text{mol m}^{-2} \text{s}^{-1}$ ):

$$\text{GPP} = \frac{P_{\max} \cdot \alpha \cdot \text{PAR}}{P_{\max} + \alpha \cdot \text{PAR}} \quad (3)$$

where  $\alpha$  ( $\mu\text{mol } \mu\text{mol}^{-1}$ ) is the initial canopy quantum use efficiency (slope of the fitted curve at  $\text{PAR} = 0$ ) and  $P_{\max}$  ( $\mu\text{mol m}^{-2} \text{s}^{-1}$ ) is the maximum canopy photosynthetic potential for  $\text{PAR} \rightarrow \infty$ .

The parameters  $R_{\text{base}}$ ,  $Q_{10}$ ,  $P_{\max}$ , and  $\alpha$  were fitted simultaneously. To account for seasonal changes in plant physiology, we fitted the parameters for 5 d running windows as proposed in Holl et al. (2019a).

We split the datasets into training (70%) and validation (30%) datasets to test model performance. We implemented the bulk-NEE model in MATLAB 2019b (MATLAB, 2019) using the *fit* function with the *NonLinearLeastSquares* fitting method. We used the *coeffvalues* function to estimate the four parameters ( $R_{\text{base}}$ ,  $Q_{10}$ ,  $P_{\max}$ , and  $\alpha$ ) and the *confint* function to estimate their 95% confidence bounds. All partitioned fluxes were converted into  $\text{CO}_2\text{-C}$  fluxes in units of  $\text{g m}^{-2} \text{d}^{-1}$  before data analysis.

#### B.3.4.4 Separating $\text{CO}_2$ fluxes from semi-terrestrial tundra and water bodies

We wanted to extract fluxes from thermokarst ponds and semi-terrestrial tundra to analyze the influence of thermokarst ponds on the carbon balance of a polygonal tundra landscape. However, due to the strong heterogeneity of the landscape and the relatively small size of the merged polygonal pond compared to the EC footprint, we measured a mixed signal from all wind directions. In other words, each flux that was measured with the EC method contained information from different land-cover types. We divided the footprint into two classes – semi-terrestrial tundra and thermokarst ponds – to assess the impact of thermokarst ponds on the carbon balance.

Similar approaches of analyzing heterogeneous eddy covariance fluxes in Arctic environments have been conducted for  $\text{CO}_2$  and  $\text{CH}_4$  (e.g., Rößger et al., 2019a,b; Tuovinen et al., 2019). Rößger et al. (2019a,b) extracted  $\text{CO}_2$  and  $\text{CH}_4$  fluxes from two different land-cover classes on a floodplain, while Tuovinen et al. (2019) separated  $\text{CH}_4$  fluxes from nine individual land-cover classes, including water, and combined them into four source classes (with no separate class for water). All three studies differentiate between fluxes from different vegetation types. Our method is dedicated to distinguishing between fluxes from semi-terrestrial tundra and water bodies.

To estimate  $\text{CO}_2$  fluxes from the merged polygonal pond ( $F_{\text{pond}}$ ), we first fitted the bulk-NEE model to training data, excluding fluxes from the direction of the merged polygonal pond ( $30^\circ < \text{WD} < 150^\circ$ , where WD denotes wind direction). We obtained a dataset consisting

of information about as much semi-terrestrial tundra as possible. We performed this step since we expected little to no photosynthetic activity in the open-water part of the merged polygonal pond. This gap-filled CO<sub>2</sub> flux (hereinafter  $F_{\text{modeled,mix}}$ ) represents the polygonal tundra surrounding the EC tower, meaning the flux is dominated by semi-terrestrial tundra, but also includes polygonal ponds from the wind directions of north, west, and south. In the model input, we excluded 30 min CO<sub>2</sub> fluxes with an absolute value of more than  $4 \text{ g m}^{-2} \text{ d}^{-1}$ . In 38 windows of 5 d duration, we found an  $R^2$  above 0.9 between the model output and the validation set. In 18 cases, we obtained an  $R^2$  between 0.8–0.9; in six instances, we obtained an  $R^2$  below 0.7. The final RMSE between the model input and the gap-filled NEE had a value of  $0.29 \text{ g m}^{-2} \text{ d}^{-1}$ .

We assumed that the total observed flux was a linear combination of the fluxes from the land-cover types weighted by their respective contribution to the footprint. Thus, we postulated that the observed CO<sub>2</sub> flux ( $F_{\text{obs,mix}}$ , not gap-filled) was the sum of the individual land-cover type fluxes ( $F_{\text{modeled,mix}}$  and the merged polygonal pond  $F_{\text{pond}}$ ) each multiplied with their weighted footprint fraction ( $\alpha_{\text{mix}}$  and  $\alpha_{\text{pond}}$ ), with  $\alpha_{\text{open water}} = \alpha_{\text{pond}}$ ,  $\alpha_{\text{mix}} = \alpha_{\text{sum}} - \alpha_{\text{pond}}$ , and  $\alpha_{\text{sum}}$  being the sum over all land-cover classes:

$$\begin{aligned} F_{\text{obs,mix}} &= \alpha_{\text{pond}} \cdot F_{\text{pond}} + \alpha_{\text{mix}} \cdot F_{\text{modeled,mix}} \\ \Leftrightarrow F_{\text{pond}} &= \frac{F_{\text{obs,mix}} - \alpha_{\text{mix}} \cdot F_{\text{modeled,mix}}}{\alpha_{\text{pond}}}. \end{aligned} \quad (4)$$

To improve data quality, we excluded 30 min fluxes of  $F_{\text{pond}}$  when  $\alpha_{\text{pond}} < 50\%$ . Then, we used the median of  $F_{\text{pond}}$  for further calculations, and we assumed that all thermokarst ponds in the EC footprint emitted the same amount of CO<sub>2</sub>.

As mentioned above, the observed CO<sub>2</sub> flux from the wind directions of north, west, and south ( $F_{\text{obs,mix}}$ ) was influenced by polygonal ponds to a small degree. Since our aim was to assess the impact of thermokarst ponds (both polygonal ponds and merged polygonal ponds) on NEE, we needed to eliminate the influence of polygonal ponds from our NEE estimate. To extract uncontaminated CO<sub>2</sub> flux data from the semi-terrestrial tundra ( $F_{\text{modeled,tundra}}$ ), we subtracted the previously estimated pond CO<sub>2</sub> flux  $F_{\text{pond}}$  from the observed CO<sub>2</sub> flux  $F_{\text{obs,mix}}$ :

$$F_{\text{modeled,tundra}} = \frac{F_{\text{obs,mix}} - \alpha_{\text{pond}} \cdot F_{\text{pond}}}{\alpha_{\text{mix}}}. \quad (5)$$

We then used this estimated CO<sub>2</sub> flux from the semi-terrestrial tundra  $F_{\text{modeled,tundra}}$  as the regressand variable for the bulk-NEE model to obtain a gap-filled dataset regarding CO<sub>2</sub> flux from the semi-terrestrial tundra. This gap-filling modeling of CO<sub>2</sub>-C flux had an RMSE of  $0.31 \text{ g m}^{-2} \text{ d}^{-1}$ .

To evaluate the impact of thermokarst ponds on landscape CO<sub>2</sub> flux, we estimated a polygonal tundra landscape–CO<sub>2</sub> flux from the Late Holocene river terrace of Samoylov Island ( $F_{\text{landscape}}$ ) by combining thermokarst ponds and semi-terrestrial tundra linearly:

$$F_{\text{landscape}} = A_{\text{pond}} \cdot F_{\text{pond}} + A_{\text{tundra}} \cdot F_{\text{modeled,tundra}},$$

where  $F_{\text{pond}}$  describes the CO<sub>2</sub> emissions from the open-water areas of thermokarst ponds (Eq. 4),  $F_{\text{modeled,tundra}}$  describes the modeled CO<sub>2</sub> flux from the semi-terrestrial tundra (Eq. 5),  $A_{\text{pond}} = 0.07$  is the fraction of the river terrace area of Samoylov Island that is covered by thermokarst ponds (from the land-cover classification; see Sect. B.3.4.1), and  $A_{\text{tundra}} = 1 - 0.07$  is the fraction of the entire river terrace area that consists of other land-cover types. We did not account for larger or deeper lakes in this upscaling approach as we expected different greenhouse gas emission dynamics from these lakes and there were no lakes in our footprint and therefore within our observation range. Thus, we scaled the above numbers to  $A_{\text{tundra}} + A_{\text{pond}} = 1$ , which results in  $A_{\text{pond}} = 0.076$  and  $A_{\text{tundra}} = 0.924$ .

#### B.3.4.5 CH<sub>4</sub> flux partitioning

The data show that the CH<sub>4</sub> emissions from the heterogeneous landscape around the tower were less spatially uniform than the CO<sub>2</sub> emissions. Therefore, we could not use a gap-filling model for CH<sub>4</sub> that was similar to the bulk model we used for CO<sub>2</sub>, so we investigated CH<sub>4</sub> emissions in a different way. Based on preliminary results from our analysis and the aerial image of the study site, we focused on four wind sectors instead of extracting the fluxes from the land-cover types:

- *Tundra*. At least half of the footprint consisted of dry tundra, and the wind direction was larger than 170°.
- *Shore 50° (denoted shore<sub>50°</sub>)*. Less than 40% of the footprint consisted of dry tundra, and water comprised at least 30% of the footprint. The wind direction range was 30° < WD < 65°.
- *Pond*. At least half of the footprint consisted of open water, and the wind direction range was 65° < WD < 110°.
- *Shore 120° (denoted shore<sub>120°</sub>)*. Less than 40% of the footprint consisted of dry tundra, and water comprised at least 30% of the footprint. The wind direction range was 110° < WD < 130°.

#### B.3.4.6 CH<sub>4</sub> permutation test

To evaluate whether the differences in flux medians between the four wind sectors were significant, we applied a permutation test (Edgington and Onghena, 2007). In this test, we randomly assigned each

30 min flux to one of two groups and calculated both groups' medians and the differences between the group's medians. We conducted six tests in total, using all possible combinations of pairs with the four wind sectors. After repeating this step 10 000 times, we plotted the resulting differences in medians in a histogram and performed a one-sample t test to evaluate whether the observed difference in medians differed significantly ( $p < 0.01$ ) from the randomly generated differences.

## B.4 RESULTS

### B.4.1 Meteorological conditions

During the measurement period between 11 July and 10 September 2019, half-hourly air temperatures range from  $-0.5$  to  $27.6$  °C with a mean temperature of  $8.7$  °C (Fig. 18a). The maximum wind speed measured at the EC tower at a height of  $2.25$  m is  $8.9$   $\text{m s}^{-1}$  (Fig. 18b). PAR reaches values of up to  $1419$   $\mu\text{mol m}^{-2} \text{s}^{-1}$  with decreasing maximum values during the measurement period (Fig. 18c). Throughout the measurement period, there are 28 cloudy days, determined by identifying days with low PAR values (maximum values below  $\sim 500$   $\mu\text{mol m}^{-2} \text{s}^{-1}$ ).

### B.4.2 CO<sub>2</sub> fluxes

When inspecting the relation between observed CO<sub>2</sub> fluxes and wind direction (Fig. 12), we find that CO<sub>2</sub> fluxes exhibit high temporal variability between positive and negative CO<sub>2</sub> fluxes from most wind directions. In the wind sector between  $60$ – $120$ °, the flux source area is dominated by the merged polygonal pond. The CO<sub>2</sub>–C fluxes from this pond sector show smaller absolute variability ( $0.09^{0.38}_{-0.33}$   $\text{g m}^{-2} \text{d}^{-1}$ , median<sub>5th percentile</sub><sup>95th percentile</sup>) than the fluxes from all other wind directions ( $-0.08^{0.87}_{-1.56}$   $\text{g m}^{-2} \text{d}^{-1}$ , median<sub>5th percentile</sub><sup>95th percentile</sup>). Additionally, we observe a lower respiration rate from the merged polygonal pond than from the semi-terrestrial tundra. Figure 13 shows the observed nighttime CO<sub>2</sub> fluxes plotted against the respective weighted footprint fraction of open water. We define nighttime as having PAR  $< 20$   $\mu\text{mol m}^{-2} \text{s}^{-1}$ ; we expect that there would only be respiration and no photosynthesis during the nighttime. We find that the fluxes decrease as the pond area contribution increases. Thus, the strength of CO<sub>2</sub> respiration shows a dependence on the contribution of open water. We also find that low air temperatures are mostly associated with low respiration rates.

Another aspect of CO<sub>2</sub> flux variability stems from the diurnal cycle. We compare the diurnal cycle of the CO<sub>2</sub> fluxes from the merged polygonal pond (estimated in accordance with Eq. 4) and the semi-

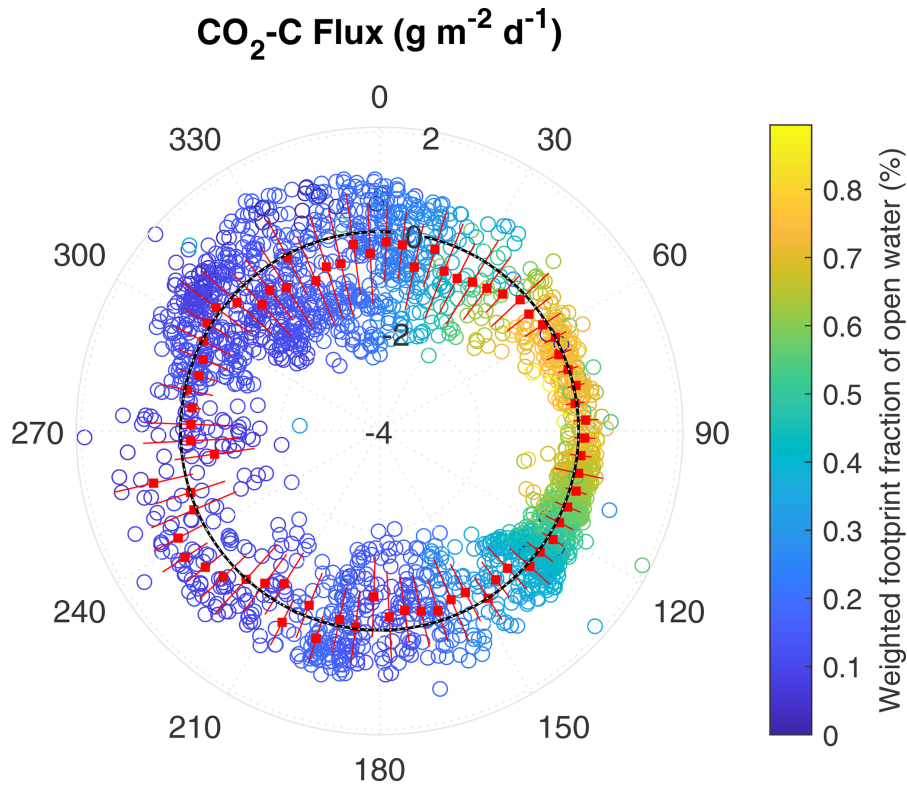


Figure 12: Polar plot of observed 30 min CO<sub>2</sub>-C fluxes with respect to the wind direction. Negative values (inside of the dashed black line) represent CO<sub>2</sub> uptake, while positive values (outside of the dashed black line) represent CO<sub>2</sub> emissions. The values  $-4$ ,  $-2$ ,  $0$ , and  $2$  indicate the magnitude of the CO<sub>2</sub>-C flux in g m<sup>-2</sup> d<sup>-1</sup>. The color of each point on the plot represents the percentage the point comprises of the total open-water weighted footprint fraction in each 30 min flux. The red boxes indicate the mean CO<sub>2</sub> flux of 5° wind direction intervals during the 2-month observation period (red lines indicate the first standard deviation).

terrestrial tundra (Eq. 5, Fig. 14). The results show a less pronounced diurnal CO<sub>2</sub> cycle from the direction of the merged polygonal pond (blue) compared to the diurnal CO<sub>2</sub> cycle from the semi-terrestrial tundra (green). We combine all data from the merged polygonal pond ( $F_{\text{pond}}$  in Eq. 4), which results in a CO<sub>2</sub>-C flux of  $0.13_{0.00}^{0.24}$  g m<sup>-2</sup> d<sup>-1</sup> (median<sub>25th percentile</sub><sup>75th percentile</sup>).

#### B.4.3 CH<sub>4</sub> fluxes

We plot the observed CH<sub>4</sub> fluxes against wind direction (Fig. 15). The results show that the CH<sub>4</sub> emissions peak at  $\sim 120^\circ$ , where fluxes from one shoreline of the merged polygonal pond contribute to the observed flux (Fig. 11d, from now on shore<sub>120°</sub>). We do not observe a similar peak of CH<sub>4</sub> emissions in the direction of the second shoreline towards

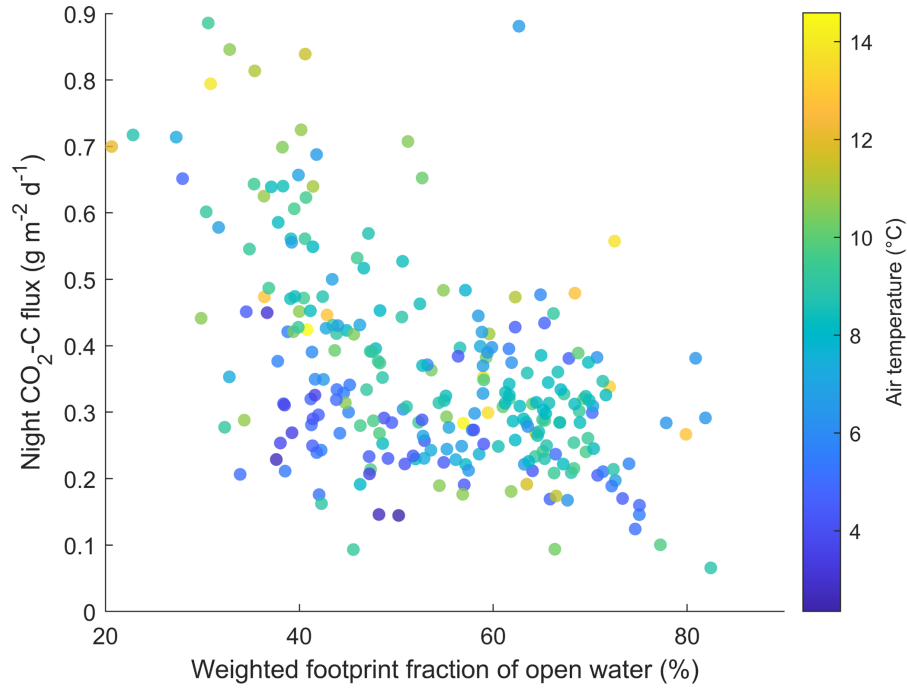


Figure 13: Scatterplot of observed CO<sub>2</sub> fluxes against the weighted footprint fraction of open water during each 30 min flux. The air temperature is represented through color. Only fluxes observed in the nighttime ( $\text{PAR} < 20 \mu\text{mol m}^{-2} \text{s}^{-1}$ ) are shown.

$\sim 50^\circ$  ( $\text{shore}_{50^\circ}$ ). These peaks did not correlate with a specifically large contribution of one of the land-cover classes to the footprint.

To further investigate the peak at  $\text{shore}_{120^\circ}$ , we compare the CH<sub>4</sub> emissions from the different wind sectors ( $\text{shore}_{120^\circ}$ ,  $\text{shore}_{50^\circ}$ , pond, and tundra; Sect. B.3.4.5). We find the following fluxes from the wind sectors:  $19.18^{24.47}_{14.26}$  ( $\text{shore}_{120^\circ}$ ),  $12.96^{15.11}_{10.34}$  ( $\text{shore}_{50^\circ}$ ),  $13.90^{18.46}_{11.02}$  (pond), and  $12.55^{16.07}_{9.65}$  mg m<sup>-2</sup> d<sup>-1</sup> (tundra, median<sub>25th percentile</sub><sup>75th percentile</sup>). Fluxes from  $\text{shore}_{120^\circ}$  have a higher median than fluxes from the other three wind sectors (Fig. 16).

We investigated the impact of wind speed and air temperature on the CH<sub>4</sub> fluxes by excluding flux intervals with high wind speed (greater than  $5 \text{ m s}^{-1}$ ) and high air temperature (warmer than  $12^\circ \text{C}$ ). The randomization test (Sect. B.3.4.6) provided evidence of a significant difference between CH<sub>4</sub> emissions from  $\text{shore}_{120^\circ}$  and the other three wind sector classes at low wind speeds (top row in Fig. 20) and no significant difference between the CH<sub>4</sub> emissions from the classes pond–tundra and  $\text{shore}_{50^\circ}$ –tundra. The difference between the classes pond and  $\text{shore}_{50^\circ}$  is significant; however, it is much smaller than the previously described differences (see central graph in Fig. 20). Note that the CH<sub>4</sub> emissions from pond and tundra have a similar magnitude under moderate wind-speed conditions. The results are very similar for moderate temperatures: we find evidence of a significant difference between the CH<sub>4</sub> emissions from  $\text{shore}_{120^\circ}$  and the CH<sub>4</sub>

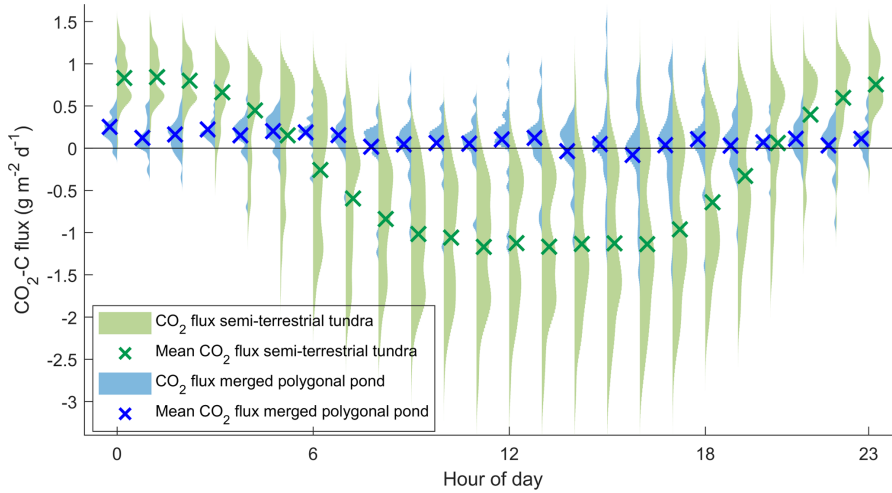


Figure 14: Diurnal cycle of modeled  $\text{CO}_2\text{-C}$  based on observations flux from the merged polygonal pond (blue, Eq. 4) and the semi-terrestrial tundra (green, Eq. 5) as violin plots for each half-hour flux. Blue and green crosses mark the mean  $\text{CO}_2\text{-C}$  flux during each half-hour flux. A violin plot shows the distribution of measurements along the y axis – the width of the curves indicates how frequently a certain y value occurred.

emissions from the other three wind sector classes (top row in Fig. 21). The differences in medians between the pond and shore<sub>50°</sub> and between the pond and tundra are significant. However, this difference is much smaller (second row in Fig. 21). In summary, neither high wind speed nor high temperatures act as a driver for the high  $\text{CH}_4$  emissions from shore<sub>120°</sub>. In contrast, the peak at 180–190° can be explained reasonably well using air temperature and friction velocity in multiple linear regression ( $R^2 = 0.44$ ). Using the same predictors results in an  $R^2$  of 0.20 for the peak at shore<sub>120°</sub>.

The ratio of  $\text{CO}_2\text{-C}$  to  $\text{CH}_4\text{-C}$  emissions at night ( $\text{PAR} < 20 \mu\text{mol m}^{-2} \text{s}^{-1}$ ) has a value of  $\text{CH}_4 / \text{CO}_2 = 0.060_{0.049}^{0.076}$  for fluxes with an open-water weighted footprint fraction of more than 60%, whereas the ratio amounts to  $\text{CH}_4 / \text{CO}_2 = 0.020_{0.015}^{0.024}$  (median<sub>75th percentile</sub> / 25th percentile) for fluxes with an open-water weighted footprint fraction of less than 20%.

#### B.4.4 Upscaled $\text{CO}_2$ flux

We use the estimated open-water  $\text{CO}_2$  flux from the merged polygonal pond and the modeled  $\text{CO}_2$  flux from the semi-terrestrial tundra to linearly upscale the  $\text{CO}_2$  flux for the polygonal tundra of Samoylov Island (excluding larger lakes, the method described in Sect. B.3.4.4). As we have not obtained estimates for the  $\text{CH}_4$  fluxes from tundra and pond land-cover types, we only upscale  $\text{CO}_2$ .

We estimate that when one includes the  $\text{CO}_2$  flux from thermokarst ponds, the river terrace landscape's  $\text{CO}_2$  uptake is  $\sim 11\%$  lower than

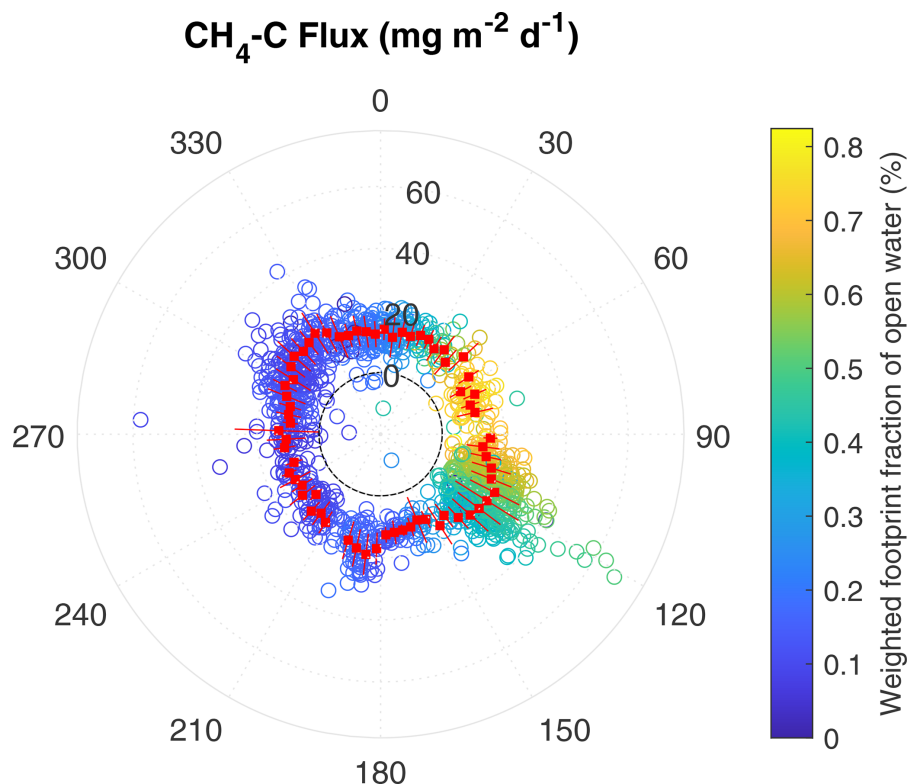


Figure 15: Polar plot of 30 min observed CH<sub>4</sub>-C flux with respect to the wind direction at the EC tower. Positive values outside the dashed black line represent CH<sub>4</sub> emissions, while values inside the line represent CH<sub>4</sub> uptake during one half-hour period. The values 0, 20, 40, and 60 indicate the magnitude of the CH<sub>4</sub>-C flux in mg m<sup>-2</sup> d<sup>-1</sup>. The color of each point on the plot represents the percentage the point comprises of the total open-water weighted footprint fraction in each 30 min flux. The red boxes indicate the mean CH<sub>4</sub> flux of 5° wind direction intervals during the 2-month observation period (red lines indicate the first standard deviation).

the uptake of semi-terrestrial tundra without ponds. The modeled CO<sub>2</sub>-C flux from the semi-terrestrial tundra (without consideration of thermokarst pond fluxes) accumulated to  $-16.29 \pm 0.43$  g m<sup>-2</sup> during the observation period (60.5 d). If separated into months, the modeled CO<sub>2</sub>-C flux from the semi-terrestrial tundra amounts to  $-15.01 \pm 0.26$ ,  $-3.56 \pm 0.33$ , and  $+2.35 \pm 0.11$  g m<sup>-2</sup> in July (19.8 d), August (31 d), and September (9.7 d), respectively. When one includes the CO<sub>2</sub> flux from the merged polygonal pond to represent all thermokarst ponds on Samoylov Island, the resulting estimate of the landscape CO<sub>2</sub> flux amounts to  $-14.47 \pm 0.40$  g m<sup>-2</sup> (60.5 d), with monthly fluxes of  $-13.75 \pm 0.24$ ,  $-2.99 \pm 0.31$ , and  $+2.27 \pm 0.10$  g m<sup>-2</sup> in July (19.8 d), August (31 d), and September (9.7 d), respectively. Thus, the results show that thermokarst ponds have the largest impact on the landscape's CO<sub>2</sub> flux in August. In September, accounting for thermokarst ponds leads to a 3.5% lower estimate of landscape CO<sub>2</sub> emissions.

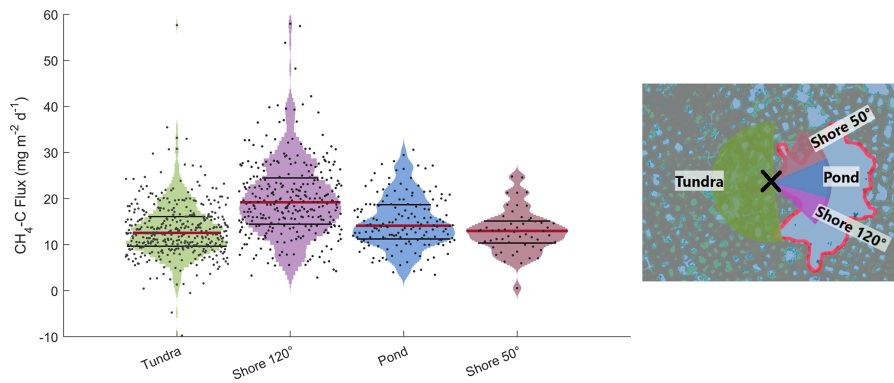


Figure 16: Violin plots of observed  $\text{CH}_4$  emissions at the EC tower separated into four different wind sector classes. A violin plot shows the distribution of measurements along the y axis – the width of the shapes indicates how frequently a certain y value occurred. Medians of  $\text{CH}_4$  emission distributions are shown as red lines, and 75th and 25th percentile are shown as black lines. On the right, the wind sectors with the eddy covariance tower in the center (black cross) are shown.

## B.5 DISCUSSION

### B.5.1 $\text{CO}_2$ flux

Only a limited number of EC  $\text{CO}_2$  flux studies from permafrost-affected ponds and lakes are available (studies with “EC” in Table B.5.1). Estimates of open-water EC  $\text{CO}_2$ -C flux range from 0.059 (Jammet et al., 2017) to 0.11 (Eugster et al., 2003) to  $0.22 \text{ g m}^{-2} \text{ d}^{-1}$  (Jonsson et al., 2008). Our estimate of  $0.12_{0.0014}^{0.24} \text{ g m}^{-2} \text{ d}^{-1}$  is, therefore, well within the range of open-water  $\text{CO}_2$ -C fluxes observed with the EC method. Other studies using different methods report a wider range of open-water  $\text{CO}_2$  fluxes in Arctic regions. These fluxes range from a minor  $\text{CO}_2$ -C uptake ( $-0.14 \text{ g m}^{-2} \text{ d}^{-1}$ ; Bouchard et al., 2015) to substantial emissions of  $\text{CO}_2$ -C (up to  $2.2 \text{ g m}^{-2} \text{ d}^{-1}$ ; Abnizova et al., 2012). A modeling study involving multiple lakes in north-east European Russia found that they produce almost zero emissions ( $0.028 \text{ g m}^{-2} \text{ d}^{-1}$ ; Treat et al., 2018).

Table 2: Daily mean water–atmosphere CO<sub>2</sub> and CH<sub>4</sub> fluxes from different study sites. TBL is the abbreviation for thin boundary layer model, EC for eddy covariance, CH for chamber measurement, MOD for modelled fluxes, STO for storage fluxes, and NEW for the method used in this study. All fluxes are given ± standard deviation, except fluxes from this study are given as median<sup>75th percentile</sup>/<sub>25th percentile</sub>.

Study	Location	Period/time	Study site	Method	CO <sub>2</sub> –C flux (g m <sup>-2</sup> d <sup>-1</sup> )	CH <sub>4</sub> –C flux (mg m <sup>-2</sup> d <sup>-1</sup> )
This study	Lena River delta, northern Siberia	11 Jul–10 Sep 2019	merged polygonal pond	EC/NEW	0.13 <sup>0.24</sup> <sub>0.00</sub>	14.10 <sup>18.67</sup> <sub>11.23</sub>
			merged polygonal pond shore	EC	–	12.96 <sup>15.11</sup> <sub>10.34</sub> – 19.18 <sup>24.47</sup> <sub>14.26</sub>
Abnizova et al. (2012)	Lena River delta, northern Siberia	1 Aug–21 Sep 2008	Samoylov Pond	TBL	1.50–2.20	–
			Samoylov Lake	TBL	1.40–2.10	–
Jammet et al. (2017)	Northern Sweden	2012–2013	Villasjön	EC	0.059	13.42 ± 1.64
Jonsson et al. (2008)	Northern Sweden	17 Jun–15 Oct 2005	Merasjärvi	EC	0.22 ± 0.002	–
				TBL	0.30 ± 0.01	
Eugster et al. (2003)	Alaska	27–31 Jul 1995	Toolik Lake	EC	0.11 ± 0.033	–
				TBL	0.13 ± 0.003	
				CH	0.37 ± 0.060	

Jansen et al. (2019)	Northern Sweden	Year round, 2010–2017	Villasjön Inre Harrsjön Mellersta Harrsjön	CH	0.22 ± 0.047 0.25 ± 0.05 0.73 ± 0.067	14.04 ± 2.25 10.39 ± 1.40 13.76 ± 2.81
Bouchard et al. (2015)	NE Canada	Jul 2013 and 2014	Bylot Island, polygon ponds Lakes	TBL	−0.14–0.74 −0.085– 0.062	0.50–6432 0.70–74.5
Sepulveda-Jauregui et al. (2015)	Alaska	Jun–Jul 2011 and 2012	8 lakes, Yedoma 32 lakes, non-Yedoma	TBL & STO	0.60 ± 0.58 0.10 ± 0.10	92.86 ± 35.72 16.80 ± 8.61
Treat et al. (2018)	NE European Russia	2006–2015	Multiple lakes	MOD	0.028 ± 0.00011	0.84 ± 0.0
Sieczko et al. (2020)	Northern Sweden	Jul–Aug 2017	Ljusvatterntjärn	CH	–	2.95 ± 0.75
Ducharme-Riel et al. (2015)	NE Canada	Summer 2008	15 lakes	TBL	0.20 ± 0.093	–
Repo et al. (2007)	Western Siberia	3 Jul–6 Sep 2005	MTlake FTlake MTpond	TBL TBL TBL	0.14 ± 0.11 0.41 ± 0.25 0.44 ± 0.25	–
Lundin et al. (2013)	Northern Sweden	2009 (only ice-free season)	27 lakes	TBL	0.18 ± 0.11	–
Kling et al. (1992)	Alaska	1975–1989	25 lakes	TBL	0.25 ± 0.040	5.16 ± 0.96

Strikingly, our estimates of open-water CO<sub>2</sub> emissions are approximately 12–18 times smaller than those that have been previously reported for open-water CO<sub>2</sub> emissions at the same study site (Abnizova et al., 2012). One reason for the divergent results might be the different methods used. In Abnizova et al. (2012), the thin boundary layer (TBL) model, following Liss and Slater (1974), was applied to estimate CO<sub>2</sub> emissions from CO<sub>2</sub> concentrations. However, one other study found good agreement between the EC method and the TBL one (Eugster et al., 2003). In addition, in contrast to the larger merged polygonal pond we focus on, Abnizova et al. (2012) measured two polygonal ponds (they took 46 water samples in August and September 2008). These two ponds might have had exceptionally high CO<sub>2</sub> concentrations and might not be representative of polygonal ponds in our study area. If the polygonal ponds in the footprint of our EC measurements emitted CO<sub>2</sub> in the quantities suggested by Abnizova et al. (2012), we would expect to see their signal more clearly in our measurements.

Our approach of combining a footprint model with land-cover classification to extract fluxes from different land-cover classes allows us to determine the thermokarst pond CO<sub>2</sub> flux. We report an uncertainty range with respect to the thermokarst pond CO<sub>2</sub> flux; however, identifying the full uncertainty in this flux is not possible using this approach due to the footprint analysis' unknown degree of uncertainty. Still, the results with respect to the thermokarst pond CO<sub>2</sub> flux are plausible and on the expected order of magnitude for two reasons. First, reduced diurnal variability is observed when the merged polygonal pond influences the flux signal (Fig. 14). This reduction indicates that the respiration rate from the merged polygonal pond is lower than the respiration rate from the semi-terrestrial tundra, where ample oxygen is available in the upper soil layer. Additionally, since the thermokarst ponds have a lower vegetation density than the tundra, there is less photosynthesis. Second, when focusing on nighttime fluxes, when only respiration occurs (i.e., no carbon is taken up), there is a decrease in CO<sub>2</sub> emissions with an increasing weighted footprint fraction of open water (Fig. 13); this also indicates that there is reduced decomposition in the merged polygonal pond. Overall, based on the data, the finding that thermokarst ponds have lower CO<sub>2</sub> emissions than the semi-terrestrial tundra is reasonable.

### B.5.2 CH<sub>4</sub> flux

We observe large differences in CH<sub>4</sub> emissions from the four wind sectors. CH<sub>4</sub> emissions from shore<sub>120°</sub> are significantly higher than from shore<sub>50°</sub>, pond, and tundra (Sect. B.4.3). Notably, we tested the dependence of these higher fluxes on wind speed and air temperature. We expect high wind speeds to enhance turbulent mixing of the

water column and diffusive CH<sub>4</sub> outgassing at the water–atmosphere interface. High wind speeds are also associated with pressure pumping, which potentially fosters the ebullition of CH<sub>4</sub>. On the other hand, peak temperatures can lead to peak CH<sub>4</sub> production and emissions due to enhanced biological activity. However, the high emissions from shore<sub>120°</sub> do not coincide with either of two key meteorological conditions, high wind speeds and high temperatures, which would especially favor high emissions. Thus, the difference in methane flux dynamics between shore<sub>120°</sub> and shore<sub>50°</sub> is astounding since the shorelines share many other characteristics.

Both shorelines extend radially (in a fairly straight line) from the EC tower (Fig. 11), thus contributing similarly to the EC flux. The underwater topography does not vary significantly between the two shorelines. Meters away from the shore, both shorelines have a water depth of a few centimeters and a few decimeters (see data from Boike et al., 2015c). As previously described in Sect. B.3.1, both shorelines are dominated by *Carex aquatilis*, and from visual inspection, we could not identify differences in shoot density. We, therefore, assume that the characteristics of the emergent vegetation do not play a major role in explaining the differences between the CH<sub>4</sub> emissions from shore<sub>120°</sub> and shore<sub>50°</sub>. We also examine the evolution of the shorelines at the merged polygonal pond to check whether erosion along the shoreline could cause the high CH<sub>4</sub> emissions. We compare an image from 1965 (U.S. Geological Survey, EROS Center, 1965) with the current (2019) shoreline, yet we cannot identify signs of recent erosion. Furthermore, high-resolution aerial images of this pond from 2008 (Boike et al., 2015a, resolution > 0.33 m) and 2015 (Boike et al., 2015b, resolution > 0.33 m) show no signs of erosion. We therefore assume that past erosion is unlikely to have been a factor that caused the high levels of CH<sub>4</sub> emissions we observed in 2019.

Local ebullition of the merged polygonal pond could lead to high CH<sub>4</sub> emissions from shore<sub>120°</sub>. We applied the method proposed by Iwata et al. (2018) to check for signs of ebullition events. This method uses the 20 Hz raw CH<sub>4</sub> concentration data to detect short-term peaks in CH<sub>4</sub> that originate from ebullition events. However, we cannot detect ebullition events in the 20 Hz raw data.

In summary, meteorological conditions (wind speed and temperature), characteristics of emergent vegetation, coastal erosion, and intense ebullition events are unlikely to be the main driving factors of the increased CH<sub>4</sub> emissions we observed. Another possible driver of higher CH<sub>4</sub> emissions from shore<sub>120°</sub> is a small but steady seep ebullition hot spot close to this shoreline (such as ebullition class *kotenok* in Walter et al., 2006). Seep ebullition hot spots have been reported to occur heterogeneously in clusters in Alaskan lakes (Walter Anthony and Anthony, 2013). Unfortunately, seep ebullition has not previously been reported in water bodies in our study area, so we did not include

measurements targeting this process in our measurement campaign. In future studies, visual inspection of trapped CH<sub>4</sub> bubbles in the ice column during wintertime, as proposed by Vonk et al. (2015), could reveal more information about the cause of the higher CH<sub>4</sub> emissions from shore<sub>120°</sub>, as could funnel or chamber measurements with high spatial coverage.

The results show that the merged polygonal pond emits a similar magnitude of CH<sub>4</sub> to the polygonal tundra surface under similar meteorological conditions and when excluding the high emissions from shore<sub>120°</sub>. However, substrate availability and temperature dynamics differ substantially. Additionally, in dense soils, methane diffuses slowly enough through soil layers containing oxygen for the methane to be oxidized before reaching the surface. In contrast, methane emitted in ponds can reach the surface quickly through ebullition or plant-mediated transport in addition to diffusion. Therefore, we expect to see larger differences between the CH<sub>4</sub> emissions from the merged polygonal pond and the polygonal tundra, more akin to the differences that have been detected in a subarctic lake and fen by Jammet et al. (2017). However, we see no significant difference in the CH<sub>4</sub> emissions from the open-water areas of the merged polygonal pond and the polygonal tundra surface (Figs. 16 and 20).

Since many other thermokarst ponds in our study area are smaller than the merged polygonal pond (making them unsuitable to study using the EC method) and since smaller ponds tend to be greater emitters of methane (Holgerson and Raymond, 2016; Wik et al., 2016), our measurements might provide a lower limit of overall thermokarst pond CH<sub>4</sub> emissions.

We estimate a CH<sub>4</sub>-C flux of  $13.38^{15.92}_{10.55}$  mg m<sup>-2</sup> d<sup>-1</sup> (median<sup>75th percentile</sup>/<sub>25th percentile</sub>) from the merged polygonal pond and  $12.96^{15.11}_{10.34}$ – $19.18^{24.47}_{14.26}$  mg m<sup>-2</sup> d<sup>-1</sup> from the shores of this pond. This is higher than the fluxes measured by Jammet et al. (2017) from a subarctic lake (Table B.5.1). The authors report a mean annual CH<sub>4</sub>-C flux of  $13.42 \pm 1.64$  mg m<sup>-2</sup> d<sup>-1</sup> and a mean ice-free-season CH<sub>4</sub>-C flux of  $7.58 \pm 0.69$  mg m<sup>-2</sup> d<sup>-1</sup>. A study focusing on 32 non-Yedoma thermokarst lakes in Alaska found CH<sub>4</sub>-C emissions similar to our results ( $16.80 \pm 8.61$  mg m<sup>-2</sup> d<sup>-1</sup>; Sepulveda-Jauregui et al., 2015). Also, a synthesis of 149 thermokarst water bodies north of ~ 50° N reports CH<sub>4</sub>-C emissions on the same order of magnitude ( $27.57 \pm 14.77$  mg m<sup>-2</sup> d<sup>-1</sup>; Wik et al., 2016). However, other recent studies have reported considerably lower CH<sub>4</sub>-C emissions of  $2.95 \pm 0.75$  mg m<sup>-2</sup> d<sup>-1</sup> in northern Sweden (Sieczko et al., 2020), and, in contrast, a study found CH<sub>4</sub>-C emissions of up to 6432 mg m<sup>-2</sup> d<sup>-1</sup> in northeast Canada (Bouchard et al., 2015). The wide range of water-body methane emissions militates in favor of caution when generalizing our results, even for Samoylov Island, especially since the emissions within the merged polygonal pond have been shown to be heterogeneous. Instead, after finding a hot spot in

CH<sub>4</sub> emissions at the pond shore, we would like to highlight that the gathering of additional measurements – for example employing funnel traps or counting bubbles in ice – will help to better constrain thermokarst pond CH<sub>4</sub> dynamics in their full complexity. Nevertheless, our measurements provide a robust lower limit of thermokarst pond CH<sub>4</sub> emissions.

## B.6 UPSCALING THE CO<sub>2</sub> FLUX

We upscale the CO<sub>2</sub> emissions for the river terrace on Samoylov, an area for which we have access to high-resolution land-cover classification. We find that we overestimate the carbon dioxide uptake of the polygonal tundra by 11 % when we do not account for the thermokarst ponds' CO<sub>2</sub> emissions. A similar approach by Abnizova et al. (2012) found a potential increase of 35 %–62 % in the estimate of CO<sub>2</sub> emissions from the Lena River delta when including small ponds and lakes in the landscape CO<sub>2</sub> emission calculation. If we were to follow the upscaling approach by Abnizova et al. (2012) and consider overgrown water as part of the thermokarst ponds, the estimate of the landscape CO<sub>2</sub> uptake would decrease by 19 %. Kuhn et al. (2018) also found water bodies in Arctic regions to be an important source of carbon, which could outbalance the carbon dioxide uptake of the semi-terrestrial tundra in a future climate. In summary, our results demonstrate that open-water CO<sub>2</sub> emissions can substantially influence the summer carbon balance of the polygonal tundra. With respect to the night time emissions, we find that per gram CO<sub>2</sub>-C thermokarst ponds emit 0.06 g CH<sub>4</sub>-C whereas the semi-terrestrial tundra only emits 0.02 g CH<sub>4</sub>-C. This finding underlines again that, especially when considering thermokarst ponds, CH<sub>4</sub> emissions are of significant interest. Even though mean CH<sub>4</sub> emissions from the semi-terrestrial tundra and open water are of similar magnitude, we expect that the impact of thermokarst ponds on the carbon balance would be even greater when accounting for CH<sub>4</sub> due to locally high emissions.

Our results suggest that future studies that aim to capture a representative landscape flux should pay extra attention to the water bodies in their footprint. The CO<sub>2</sub> flux from thermokarst ponds has the opposite sign (CO<sub>2</sub> emissions) to the semi-terrestrial tundra (CO<sub>2</sub> uptake) during the observation period. Consequently, thermokarst ponds should cover about as much area in the measurement as they do in the landscape area of interest. In this way, the chances of capturing CH<sub>4</sub> hot spots, which can be investigated more closely, are also greater.

## B.7 CONCLUSIONS

We find that thermokarst ponds are a carbon source. At the same time, the surrounding semi-terrestrial tundra in our study area acts as a carbon sink during the summer period (July–September), which is in agreement with prior studies (Abnizova et al., 2012; Jammet et al., 2017), despite us observing much lower open-water CO<sub>2</sub> fluxes compared to previous work at the same study site (Abnizova et al., 2012). Using our approach to disentangle the EC fluxes from different land-cover classes, we posit that during the measurement period, we would overestimate the carbon dioxide uptake of the polygonal tundra by 11 % if thermokarst ponds were not accounted for. We expect lakes to have a similar effect on the carbon budget, though a smaller one, since lakes (a) cover a similar amount of surface area as the thermokarst ponds in our study site (Abnizova et al., 2012; Muster et al., 2012) and (b) are weaker emitters of greenhouse gases than ponds (Holgerson and Raymond, 2016; Wik et al., 2016).

In contrast to CO<sub>2</sub> emissions, which are spatially more homogeneous, small-scale heterogeneity in CH<sub>4</sub> emissions makes it difficult to find drivers of CH<sub>4</sub> emissions. We cannot pinpoint the drivers behind the high emissions along parts of the coastline, which we surmise were potentially caused by seep ebullition. Thus, we cannot estimate the impact of this heterogeneity on the landscape scale and, therefore, refrain from upscaling CH<sub>4</sub> emissions. Additionally, the open-water fluxes presented in this paper originate from a single merged polygonal pond since the other polygonal ponds surrounding the EC tower are too small to extract their fluxes using the footprint method applied here. Thus, we do not account for the spatial variability in CH<sub>4</sub> emissions between thermokarst ponds, which can be substantial (Rehder et al., 2021; Wik et al., 2016). However, we note that open-water fluxes were of a similar magnitude to the polygonal tundra fluxes. Consequently, the main impact that thermokarst ponds have on the landscape CH<sub>4</sub> budget might occur through plant-mediated transport and local ebullition.

While being ill-suited for the study of smaller ponds, we underline that the EC method is appropriate for observing greenhouse gas fluxes from thermokarst ponds as small as 0.024 km<sup>2</sup>. The EC method has a higher temporal resolution than the TBL method. It does not disturb exchange processes like the chamber flux method, which eliminates the wind at the water surface. Especially when combining an EC footprint with land-cover classification, one can distinguish between the contribution of different land-cover classes effectively and also study the fluxes from thermokarst ponds.

We conclude that thermokarst ponds contribute significantly to the landscape carbon budget. Changes in Arctic hydrology and the concomitant changes in the water-body distribution in permafrost

landscapes may cause these landscapes to change from being overall carbon sinks to overall carbon sources.

## B.8 APPENDIX



Figure 17: Picture of the eddy covariance tower with the merged polygonal pond in the background. Picture taken on 11 July 2019 by Zoé Rehder.

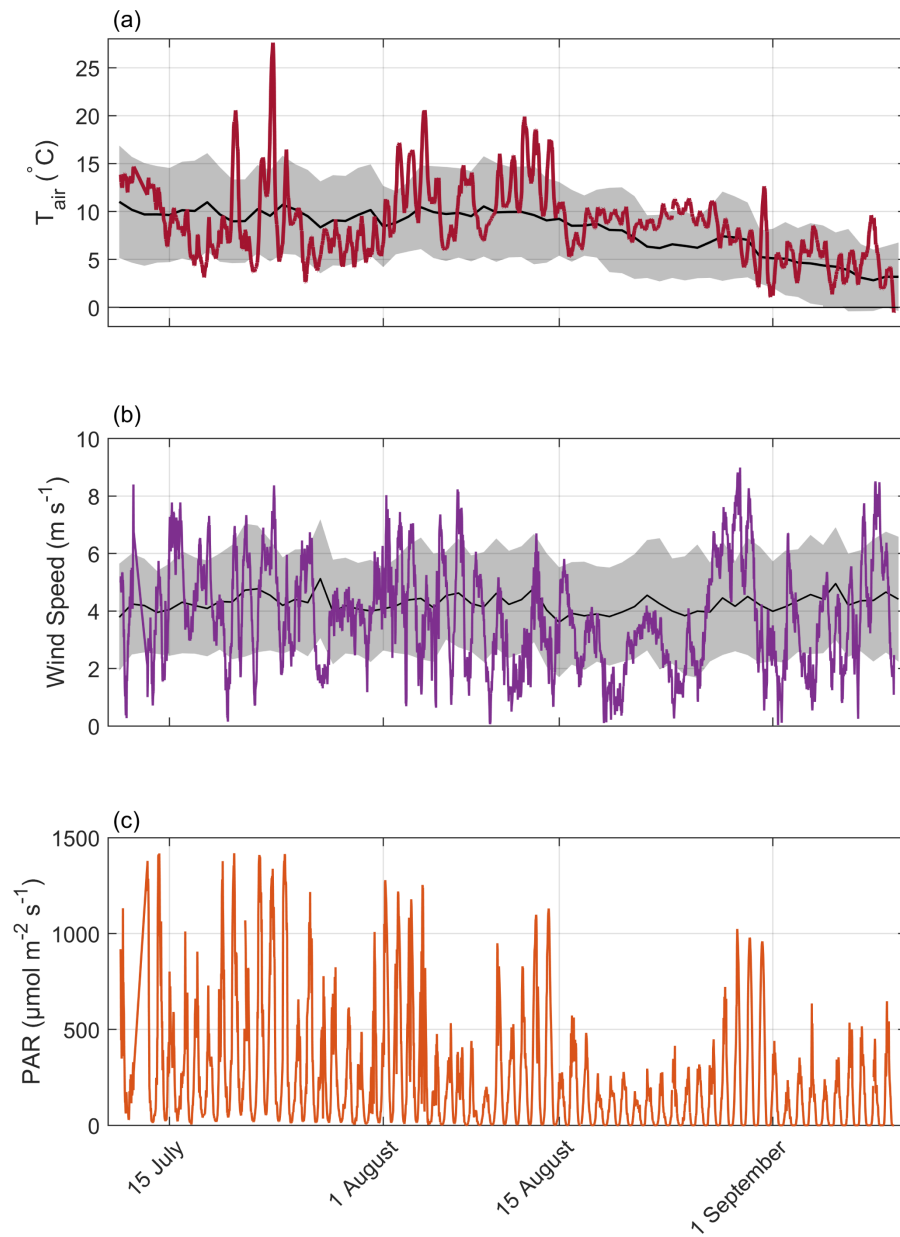


Figure 18: Timeline of observed meteorological conditions during the observation period (2019) with air temperature at 2 m height **(a)**, wind speed at 3 m height **(b)**, and photosynthetically active radiation (PAR) **(c)**. Mean values and standard deviation of observations during the past 16 years are plotted as black lines and gray areas.

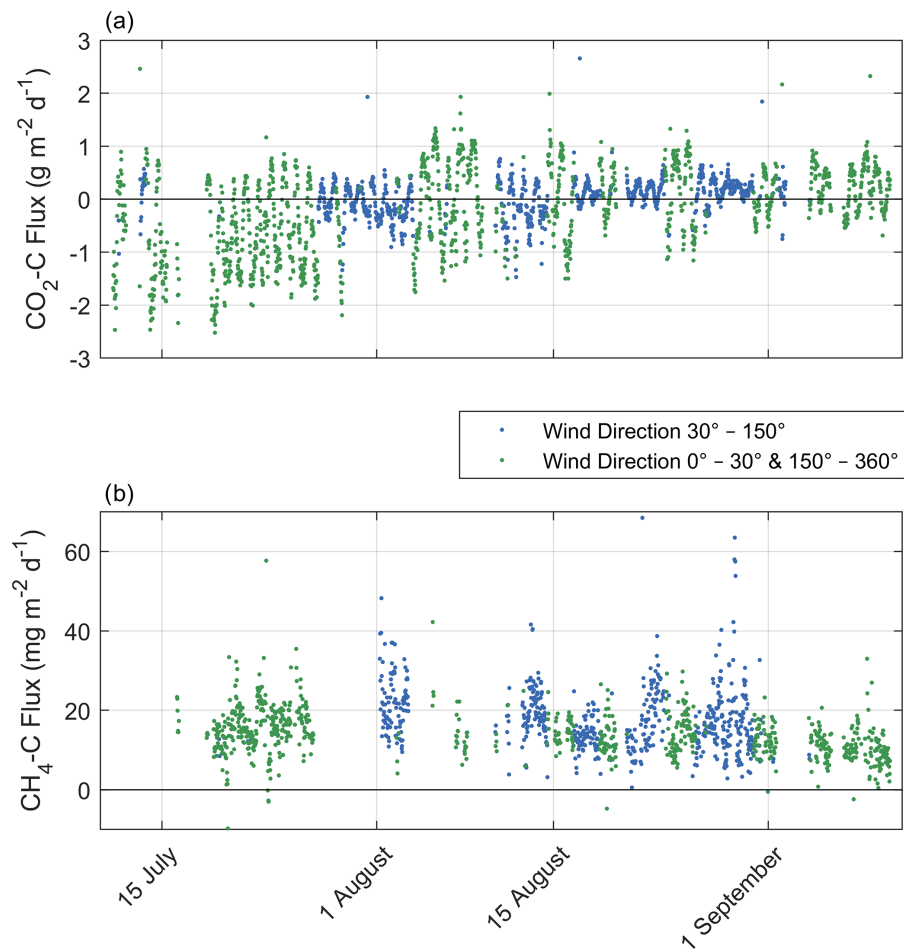


Figure 19: Time series of 30 min observed CO<sub>2</sub>-C flux intervals **(a)** and CH<sub>4</sub>-C flux **(b)** with a quality flag of 0 or 1. The blue color represents fluxes originating from the wind direction of the merged polygonal pond (30–150° wind direction, mostly mixed signals from semi-terrestrial tundra and the surface of the merged polygonal pond), and the green color represents fluxes originating from all other wind directions.

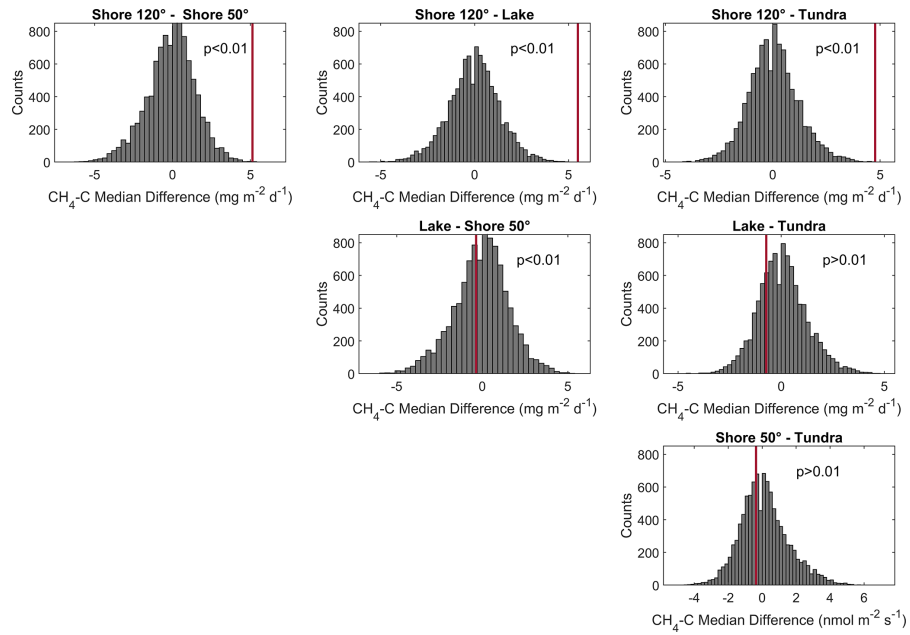


Figure 20: Histogram of permutation tests between the medians of  $\text{CH}_4$  emissions from different wind direction classes in Fig. 16. All medians from flux observations during moderate wind-speed conditions. The observed differences in medians between the different wind direction classes are shown in red vertical bars in each plot.

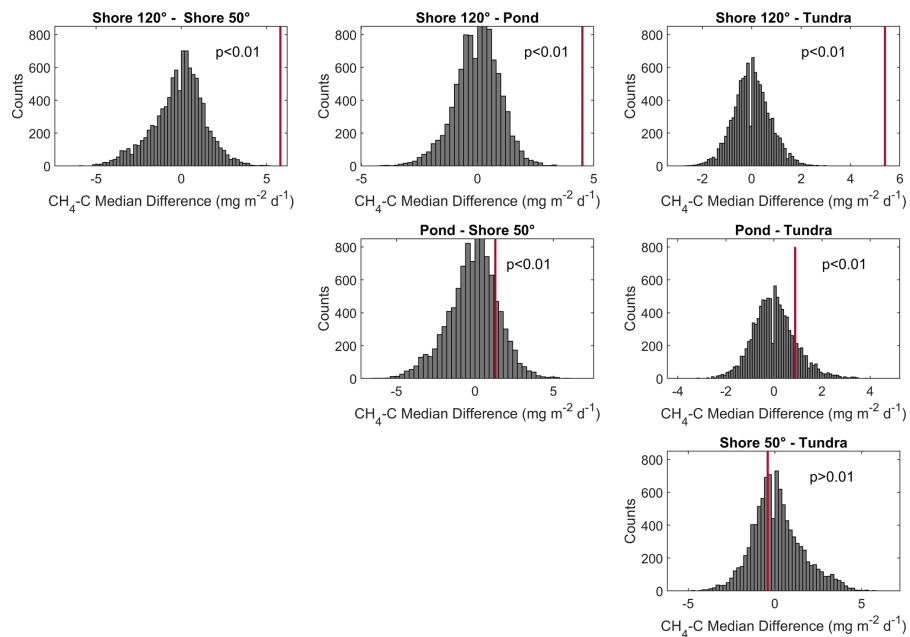


Figure 21: Histogram of permutation tests between the medians of  $\text{CH}_4$  emissions from different wind direction classes in Fig. 16. All medians from flux observations during moderate air temperature conditions. The observed differences in medians between the different wind direction classes are shown in red vertical bars in each plot.

## B.9 MANUSCRIPT INFORMATION

### *Code and data availability*

The data have been published at PANGAEA (Beckebanze et al., 2021). Code can be requested from the authors.

### *Authors contribution*

ZR and LK designed the experiments; ZR and LB carried out the fieldwork. ZR, LB, and LK developed the idea for the analysis, and CW and LB prepared the data. The formal analysis and data visualization were performed by LB and ZR with supervision by DH and LK. Resources (land-cover classification) have been provided by CM. LB and ZR prepared the manuscript with contributions from all co-authors.

### *Competing interests*

The contact author has declared that neither they nor their co-authors have any competing interests.

### *Disclaimer*

Publisher's note: Copernicus Publications remains neutral with regard to jurisdictional claims in published maps and institutional affiliations.

### *Acknowledgements*

The authors thank Norman Rüggen for his tireless support before and remotely during the fieldwork; Anna Zaplavnova, Andrei Astapov, and Waldemar Schneider for their equally tireless support in the field; Andrei Astapov and Katya Abramova for additional pictures in the field; Volkmar Assmann and the station crew of Samoylov Island for their logistical support; and Sarah Wiesner, Leonardo Galera, and Tim Eckhardt for fruitful discussions during the data analysis. Also, the authors thank the reviewers.

### *Financial support*

This study was funded by the Deutsche Forschungsgemeinschaft (DFG, German Research Foundation) under Germany's Excellence Strategy – EXC 2037 “CLICCS – Climate, Climatic Change, and Society” – Project Number: 390683824, contribution to the Center for Earth System Research and Sustainability (CEN) of Universität Hamburg,

and by the Bundesministerium für Bildung und Forschung KoPf project (grant 03Fo764A).

*Review statement*

This paper was edited by Andreas Ibrom and reviewed by two anonymous referees.

PARTITIONING CARBON FLUXES FROM A  
LANDSCAPE WITH SMALL SCALE HETEROGENEITY  
USING PARALLEL OBSERVATIONS FROM TWO  
EDDY COVARIANCE TOWERS

---

Lutz Beckebanze<sup>1,2</sup>, Zoé Rehder<sup>3,4</sup> David Holl<sup>1,2</sup>, Lars Kutzbach<sup>1,2</sup>

<sup>1</sup>Institute of Soil Science, Universität Hamburg, Germany

<sup>2</sup>Center for Earth System Research and Sustainability (CEN), Universität Hamburg, Germany

<sup>3</sup>Department of the Land in the Earth System, Max Planck Institute for Meteorology, Hamburg, Germany

<sup>4</sup>International Max Planck Research School on Earth System Modeling, Hamburg, Germany

#### C.1 ABSTRACT

The eddy covariance (EC) method represents the state-of-the-art method to observe land-atmosphere fluxes. When observing a flux from a heterogeneous landscape with varying fluxes from different landscape components, partitioning each flux from each component remains challenging. Without additional modeling approaches, the observed EC flux represents a spatially averaged flux from the surrounding landscape. However, in many cases, the partitioned flux of each landscape component is also of interest, for example, for in-depth process understanding or up-scaling approaches.

This study presents a method to source-partition EC CO<sub>2</sub> fluxes from a permafrost-affected, heterogeneous polygonal tundra landscape by using parallel observation from two EC towers. For this method, we use a footprint model in combination with two land cover classifications.

The results show that the method provides accurate CO<sub>2</sub> flux estimations from the landscape components of open water and vegetated tundra compared to a previous study. We also aimed to source-partition the CO<sub>2</sub> flux from vegetated tundra into the surface components of dry and wet tundra. This step did not provide reliable results for CO<sub>2</sub> flux estimations for the two landscape components since the results highly depended on the chosen land cover classification. Nevertheless, the presented method could function as a useful tool for future source-partitioning approaches of heterogeneous landscapes, not only in the polygonal tundra landscape.

## C.2 INTRODUCTION

The eddy covariance (EC) method is used to observe the exchange of gases and energy between the ground and the atmosphere (Baldocchi, 2003). This measurement technique requires a homogeneous surface surrounding the observation site, e.g., continuous grassland or tundra. Gaining flux information of more than one surface class is challenging and only possible when a clear boundary between the surface classes is present (Rößger et al., 2019b). The polygonal tundra, a landscape type in the Arctic with a small-scale heterogeneity, lacks clear boundaries between the surface classes. It is not possible to estimate the flux from a single surface component using the EC method. This study presents a method to analyze the individual fluxes from two different surface components within the polygonal tundra using two nearby EC towers. This universal method can be applied to other sites where two distinct surface components occur throughout the landscape.

The polygonal tundra features dry and wet patches, areas with open water, and overgrown water (Muster et al., 2012). The area of polygonal tundra has acted historically as a sink for atmospheric carbon and has accumulated large amounts of carbon (Zubrzycki et al., 2014). Small-scale variability of CO<sub>2</sub> exchange between dry and wet areas within the polygonal tundra and the atmosphere has been studied by Eckhardt et al. (2019). This study focused on the pedon scale and observed the CO<sub>2</sub> exchange using a manual chamber method. The authors found that the wet areas within one polygon act as stronger growing season sinks for atmospheric CO<sub>2</sub> compared to the dry areas of the same polygon. Other studies in Arctic environments have partitioned observed gas fluxes into different surface components. Rößger et al. (2019a,b) separated the CO<sub>2</sub> and CH<sub>4</sub> fluxes from a fluvial floodplain into the single component fluxes originating from areas dominated by sedges and shrubs, respectively. Juutinen et al. (2022) separated fluxes from a tundra site into multiple different flux components using the chamber flux method, and Beckebanze et al. (2022a) partitioned EC flux into flux components from the open water and the vegetated tundra.

This study presents a new method which allows to partition the CO<sub>2</sub> fluxes from a heterogeneous landscape into the landscape components' fluxes. We use data from two EC towers that ran parallel between 11 July and 10 September 2019. One EC tower is a long-term observatory and has been in operation since 2002 (Holl et al., 2019b). The other EC tower was a temporary tower next to a lake and was located approximately 500 meters east of the long-term observatory. For our study site, two different land cover classifications are available (Mirbach et al., 2022; Muster et al., 2012). For the new method to identify the single flux components, we combine the data from the two EC towers with a footprint model (Kormann and Meixner, 2001) and both land

cover classifications. In a first step, we apply this new method on the surface classes of water and vegetated tundra. In a second step, we apply the method on the two components of the vegetated tundra, namely dry and wet tundra and estimate each components' CO<sub>2</sub> exchange. We compare the results from the estimation with each land cover classification.

### C.3 METHODS

#### C.3.1 Study site and instruments

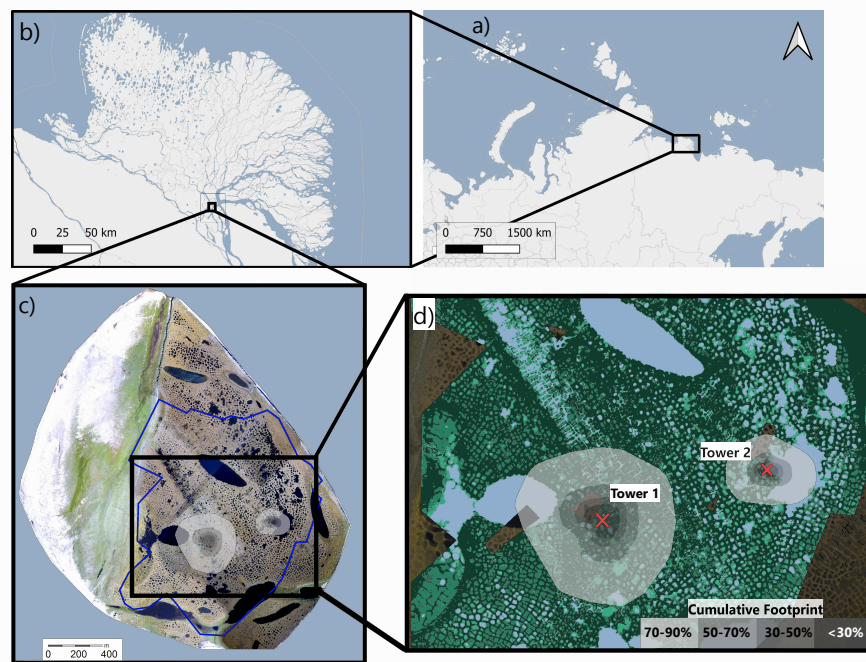


Figure 22: The location of the study site in Russia is shown in (a), and the location of Samoylov Island within the Lena River Delta is shown in (b). Samoylov Island is shown in (c); the surrounding Lena River appears in light blue. The blue line indicates the outline of the river-terrace land-cover classification (Sect. B.3.4.1). In (d), the land-cover classification is shown in blue (open water) and green shades (dark green: dry tundra; medium green: wet tundra; and light green: overgrown water). The location of the EC towers 1 and 2 are marked by red crosses. The cumulative footprints of both towers (see Sect. B.3.4.2) are shown in gray shades in (c) and (d). 30 % of the cumulated flux likely originated from within the dark gray area, 50 % from within the medium-dark gray area, 70 % from within the medium-light gray area and 90 % from within the light gray area. Map data from © OpenStreetMap contributors 2020, distributed under the Open Data Commons Open Database License (ODbL) v1.0 (a & b) and modified based on Boike et al. (2012b) (c & d).

The study site Samoylov island (Fig. 22, c) is located in the southern part of the Lena River Delta, Russia and has been described in detail in section B.3.1. We used flux observation data from two eddy covariance (EC) towers: Tower 1, a long-term observatory tower, and Tower 2, a temporary tower. Tower 1 is located in the western part of the river terrace on Samoylov Island and is mainly surrounded by dry and wet polygonal tundra and a few polygonal ponds (Figure 22, d). The closest thermokarst lake is located about 165 meters northwest of the tower. EC instruments at this 10-m-tower are installed at the height of 4.15 meters. The tower is equipped with a CO<sub>2</sub>/H<sub>2</sub>O open-path sensor (Licor 7500A and Licor 7700, LI-COR Biosciences, USA), a CO<sub>2</sub>/H<sub>2</sub>O closed-path sensor (Licor 7000 and LGR FMA, Los Gatos Research, USA), as well as a 3D-ultrasonic anemometer (CSAT3, Campbell Scientific, UK). All instruments have a sampling rate of 20 Hz. More details on the instrumentation can be found in Holl et al. (2019b).

Tower 2 is located in the eastern part of Samoylov Island, directly at the western shore of a large thermokarst lake (Figure 22, d). EC instruments are mounted on a tripod at the height of 2.25 meters. The tower has a closed-path CO<sub>2</sub>/H<sub>2</sub>O sensor (Licor 7200) and a 3D-ultrasonic anemometer (R3-50, Gill Instruments Limited, UK). These instruments also have a sampling rate of 20 Hz. This tower is already described in chapter B (Beckebanze et al., 2022a).

For this study, we use observational data from 11 July to 10 September 2019, when all instruments at both towers ran simultaneously. We also installed radiation-shielded temperature and humidity sensors at the EC tower (HMP155, Vaisala, Finland). We used data from a photosynthetically active radiation (PAR) sensor mounted on a tower approximately 500 m to the west of the EC tower (SKP 215, Skye Instruments, UK). Additional meteorological data for Samoylov Island were provided by Boike et al. (2019).

### c.3.2 *Data Analysis*

#### c.3.2.1 *Land-cover classification*

The new land cover classification in this analysis was provided by Mirbach et al. (2022). It contains four land-cover classes (dry tundra, wet tundra, overgrown water, and open water) and covers the river terrace (eastern part) of Samoylov Island. A detailed description of this land-cover classification can be found in Beckebanze et al. (2022a), section 2.4.1. The old land-cover classification was provided by Muster et al. (2012) and contained the same four land-cover classes as the new land-cover classification.

### c.3.2.2 Footprint model

The tower's footprint describes the source area of the flux within the surrounding landscape. We implemented the analytical footprint model proposed by Kormann and Meixner (2001) in Matlab 2019b. We combined the footprint model with land-cover classification data described in Sect. C.3.2.1 to estimate the contribution of each land-cover type to the source area of each half-hourly flux (from now on referred to as the *weighted footprint fraction*). We received a two-dimensional probability density function of the source area for each flux from the model. The resolution of the footprint model was set to the land-cover classification resolution of  $0.17 \text{ m} \times 0.17 \text{ m}$ . We estimated each grid cell's dominant land-cover type from the land-cover classification. We combined both pieces of information for each grid cell and calculated the sum of the fraction fluxes within the source area for each of the four land-cover types (dry tundra, wet tundra, overgrown water, and open water) and determined each weighted footprint fraction for each 30-min flux estimate ( $a_{\text{dry tundra}}$ ,  $a_{\text{wet tundra}}$ ,  $a_{\text{overgrown water}}$ , and  $a_{\text{open water}}$ ). We processed data from both towers in this way. A more detailed description of the footprint model application can be found in Beckebanze et al. (2022a).

### c.3.2.3 Separating CO<sub>2</sub> fluxes from dry and wet tundra

With this new method, a 2-step data analysis, we aimed to separate the CO<sub>2</sub> flux components of dry tundra and wet tundra from the mixed signal observed at EC towers 1 and 2. This analysis is based on assumptions about land cover classifications and the C fluxes in the study area. These assumptions will be discussed in section and are as followed:

1. An accurate land cover classification must be given for the area of interest
2. A mixed signal of EC measurement is a linear combination of each flux type in the footprint weighted by their respective contribution to the footprint
3. Waterbody emissions of CO<sub>2</sub> have a low spatial and temporal variation at this study site (as shown in Beckebanze et al. 2022a).

In this first step, we combine the four land cover classes (described in section B.3.4.2) into two classes of water and vegetation ( $a_{\text{water}1} = a_{\text{wat}}$ ,  $a_{\text{veg}} = a_{\text{dry}} + a_{\text{wet}} + a_{\text{ove}}$ ). Especially the assumption (1) and (2) allow us to write the observed flux from both EC towers as a linear combination of the flux components, and each multiplied with their weighted footprint fraction:

$$F_1 = a_{\text{veg}1} \cdot F_{\text{veg}} + a_{\text{water}1} \cdot F_{\text{water}} \quad (6)$$

$$F_2 = a_{\text{veg}2} \cdot F_{\text{veg}} + a_{\text{water}2} \cdot F_{\text{water}} \quad (7)$$

where  $F_1$  and  $F_2$  represent the observed  $\text{CO}_2$  flux at towers 1 and 2,  $F_{\text{veg}}$  and  $F_{\text{water}}$  the  $\text{CO}_2$  fluxes from the vegetated tundra and water, respectively, and  $a_{\text{veg}1}$ ,  $a_{\text{veg}2}$ ,  $a_{\text{water}1}$ , and  $a_{\text{water}2}$  the weighted footprint fraction of vegetated tundra and water at tower 1 and 2. Rearranging these two equations gives:

$$F_{\text{veg}} = \frac{F_1 \cdot a_{\text{water}2} - F_2 \cdot a_{\text{water}1}}{a_{\text{veg}1} \cdot a_{\text{water}2} - a_{\text{water}1} \cdot a_{\text{veg}2}} \quad (8)$$

$$F_{\text{water}} = \frac{F_2 \cdot a_{\text{veg}1} - F_1 \cdot a_{\text{veg}2}}{a_{\text{veg}1} \cdot a_{\text{water}2} - a_{\text{water}1} \cdot a_{\text{veg}2}}. \quad (9)$$

In this way, we estimate a time series of  $\text{CO}_2$  fluxes from vegetated tundra and water. We only use data points when  $a_{\text{water}2} > 35\%$  to have a large difference in footprint weighted fraction between towers 1 and 2. With small differences in the footprint weighted fraction of one class, the denominator of equation 8 and 9 approaches zero. It, therefore, increases the mathematical uncertainty in this estimation.

In the second step, we subtract the previously estimated average water  $\text{CO}_2$  flux ( $\overline{F_{\text{water}}}$ ) multiplied by the footprint weighted fraction of open water ( $a_{\text{water}1}$  and  $a_{\text{water}2}$ ) from the observed flux to receive a dataset purely from the vegetated tundra. We then use assumptions 1 and 2 to write the estimated flux from both EC towers as a linear combination of the flux components  $F_{\text{dry}}$  and  $F_{\text{wet}}$  (*dry* contains the information from the dry tundra and *wet* the information of the wet tundra) each multiplied with their footprint weighted fraction (Eq. 10 and 11). We use, in this case, the 21-day median of  $F_{\text{water}}$  due to the low spatial and temporal variability of this value (assumption 3). Additionally, we only use data points in this step that have not been used in step one (thus  $a_{\text{water}2} < 35\%$ ) to have two independent datasets.

$$(F_1 - a_{\text{water}1} \cdot \overline{F_{\text{water}}}) = a_{\text{wet}1} \cdot F_{\text{wet}} + a_{\text{dry}1} \cdot F_{\text{dry}} \quad (10)$$

$$(F_2 - a_{\text{water}2} \cdot \overline{F_{\text{water}}}) = a_{\text{wet}2} \cdot F_{\text{wet}} + a_{\text{dry}2} \cdot F_{\text{dry}} \quad (11)$$

where  $a_{\text{wet}1}$  and  $a_{\text{wet}2}$  represent the weighted footprint fraction of wet tundra at towers 1 and 2, and  $a_{\text{dry}1}$ , and  $a_{\text{dry}2}$  represent the weighted footprint fraction of dry tundra at tower 1 and 2. After rearranging these two equations, we received the following:

$$F_{\text{wet}} = \frac{(F_1 - a_{\text{water}1} \cdot \overline{F_{\text{water}}}) \cdot a_{\text{dry}2} - (F_2 - a_{\text{water}2} \cdot \overline{F_{\text{water}}}) \cdot a_{\text{dry}1}}{a_{\text{wet}1} \cdot a_{\text{dry}2} - a_{\text{dry}1} \cdot a_{\text{wet}2}} \quad (12)$$

$$F_{\text{dry}} = \frac{(F_2 - a_{\text{water}2} \cdot \overline{F_{\text{water}}}) \cdot a_{\text{wet}1} - (F_1 - a_{\text{water}1} \cdot \overline{F_{\text{water}}}) \cdot a_{\text{wet}2}}{a_{\text{wet}1} \cdot a_{\text{dry}2} - a_{\text{dry}1} \cdot a_{\text{wet}2}} \quad (13)$$

For the final analysis, we cut off the first and last 21 days since only a few data points of the water  $\text{CO}_2$  dominated the 21-day median in these periods.

## C.4 RESULTS AND DISCUSSION

In the first step of the method, we separate the fluxes into the water CO<sub>2</sub> flux and the flux from the semi-terrestrial tundra. We find a water CO<sub>2</sub>-C flux of  $0.10_{0.02}^{0.19}$  g m<sup>-2</sup> d<sup>-1</sup> (median<sub>25th percentile</sub><sup>75th percentile</sup>) and  $0.11_{-0.01}^{0.26}$  g m<sup>-2</sup> d<sup>-1</sup> (median<sub>25th percentile</sub><sup>75th percentile</sup>) using the old and new land cover classification, respectively. This good agreement most likely comes from the fact that water and semi-terrestrial tundra have contrasting spectral properties in both the visible and infrared bands. Both types of images function as the base for the land cover classifications. With easterly winds, only about 15% of each flux signal at the large tower originates from open water, whereas this value rises to 70–80% at the small tower under the same easterly winds. These differences in the weighted footprint fraction are independent of the chosen land cover classification (Figure 24b, 24a, 23b, and 23a). The large differences of open water and semi-terrestrial tundra in different directions from each tower allow a robust estimation of the two landscape components' CO<sub>2</sub> fluxes, thus, agreeing with the first assumption from section C.3.2.3. The water CO<sub>2</sub> flux estimations are also in good agreement with a previous study from this same site, where a water CO<sub>2</sub> flux of  $0.13_{0.00}^{0.24}$  g m<sup>-2</sup> d<sup>-1</sup> (median<sub>25th percentile</sub><sup>75th percentile</sup>) was reported (Beckebanze et al., 2022a).

The results from the second analysis step are more ambiguous. We see a clear diurnal cycle for dry and wet tundra with a stronger amplitude for wet tundra when using the new land cover classification (Figure 27b). However, when using the old land cover classification, the diurnal cycle for wet tundra is a mirror image of the diurnal cycle for dry tundra (Figure 27a). This difference in the estimations likely originates from the different footprint weighted fractions for dry and wet tundra west of the small tower, where the old land cover classification classifies more area as dry tundra. In contrast, the new land cover classification shows a similar amount of dry and wet tundra (Figure 23a and 23b).

Both land cover types, dry and wet tundra, are part of the semi-terrestrial tundra. They differ in the soil water content and partially also in the dominant vegetation type. These differences are challenging to distinguish in the land cover classification since the boundary between the two classes is less clear-cut than for open water and semi-terrestrial tundra. Small differences in the input images for the land cover classifications and the chosen classification algorithms can therefore lead to a different interpretation of the given surface type. We cannot say which land cover classification is more reliable and provides values closer to the field's reality. From field survey, we can confirm that the tundra in the area west of the small tower is wetter than other regions on Samoylov Island. A previous study from the same study site found mean NEE (CO<sub>2</sub>-C) from a polygon rim

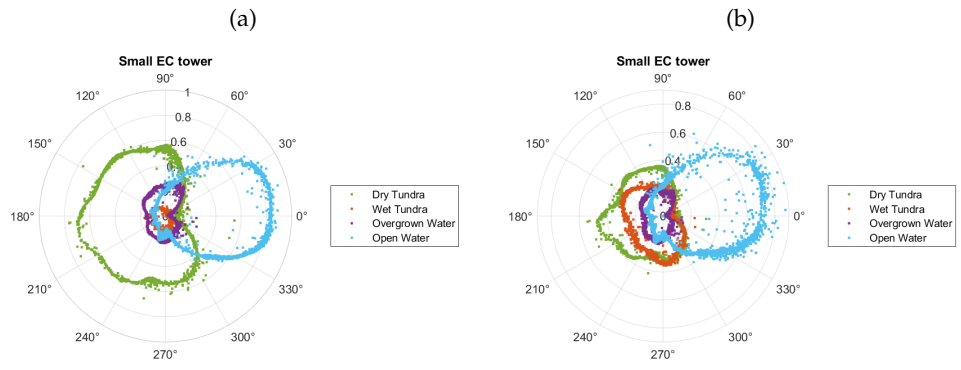


Figure 23: Footprint weighted land surface contribution at small tower with (a) old land cover classification and (b) new land cover classification

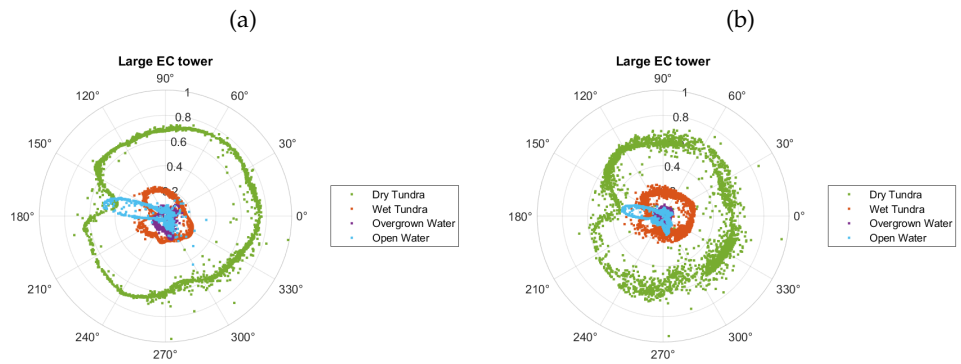


Figure 24: Footprint weighted land surface contribution at large tower with (a) old land cover classification and (b) new land cover classification

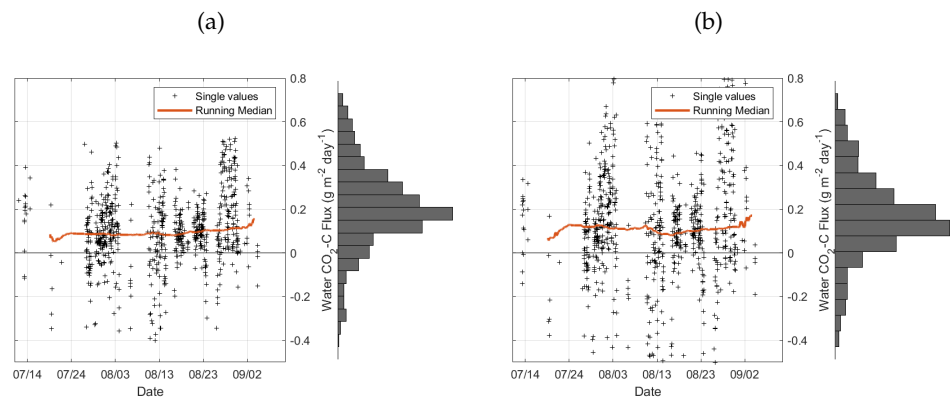


Figure 25: Time series of water  $\text{CO}_2$  flux with (a) old land cover classification and (b) new land cover classification

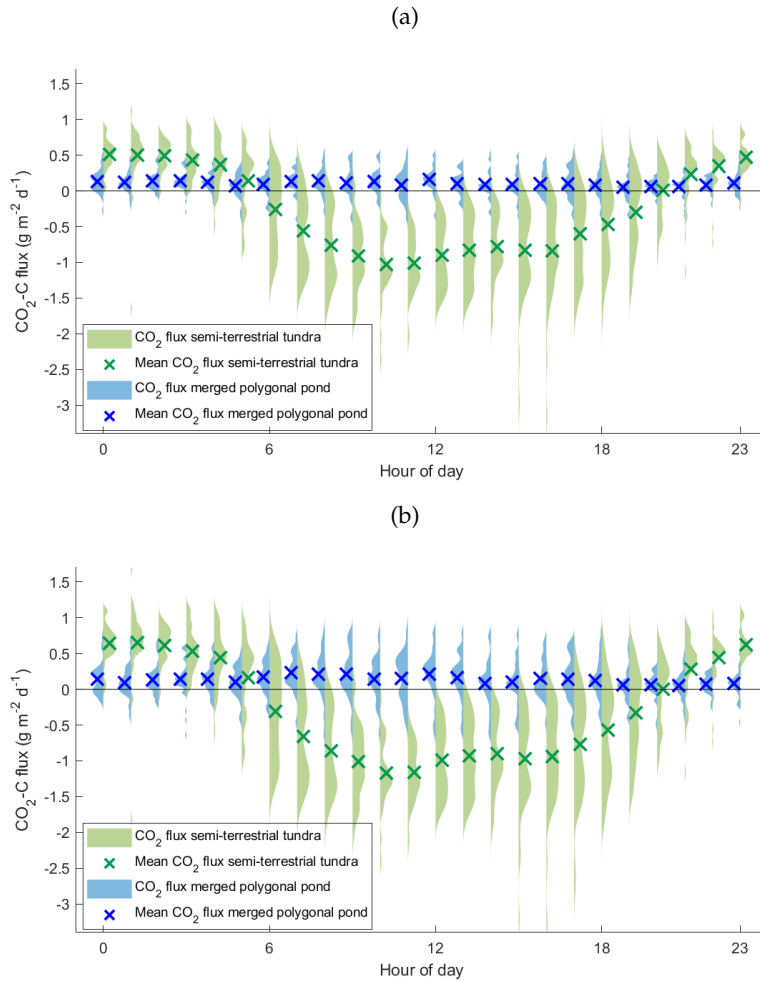


Figure 26: Diurnal cycle of water CO<sub>2</sub> flux and vegetated tundra CO<sub>2</sub> flux with (a) old land cover classification and (b) new land cover classification

(dry tundra) and polygon center (wet tundra, both 11 July until 22 September 2015) of  $-0.61$  and  $-1.60$  g m<sup>-2</sup> d<sup>-1</sup>, respectively (Eckhardt et al., 2019). During the observation period of this study, the CO<sub>2</sub>-C fluxes from dry and wet tundra (estimated using the new land cover classification) have mean values of  $-0.23$  and  $-0.41$  g m<sup>-2</sup> d<sup>-1</sup> for dry and wet tundra, respectively. Thus, the results of this study are 3.8 and 2.6 fold higher than the results from Eckhardt et al. (2019), yet, in the same order of magnitude and in a similar proportion of dry to wet tundra. The field survey, in combination with the previous results, increases our confidence in the new land cover classification by Mirbach et al. (2022) representing the area west of the small tower better than the old land cover classification.

Especially the importance of the first assumption from section C.3.2.3 (*An accurate land cover classification must be given for the area of interest*) has been discussed in depth in the sections above. We now discuss

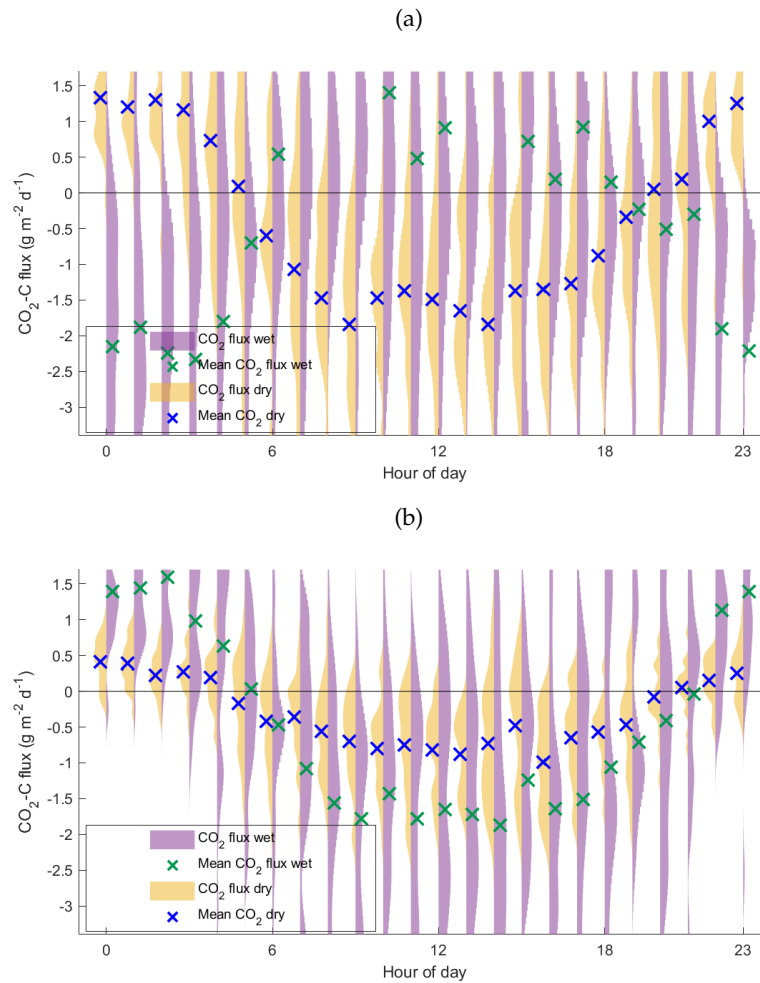


Figure 27: Diurnal cycle of wet and dry tundra  $\text{CO}_2$  flux estimated with (a) old land cover classification and (b) new land cover classification

the plausibility of the other three assumptions on which this method is based. The second assumption (*a mixed signal of EC measurement is a linear combination of each flux type*) has been used in an analysis from a nearby study site (Rößger et al., 2019a). The authors reported conclusive results for the linear combination of fluxes from different land cover classes. However, a possible heterogeneity within one surface class could counter the assumption in case the heterogeneity within one surface class would result in heterogeneous  $\text{CO}_2$  fluxes. Yet, we should not forget that it is the nature of a classification that slightly different, but similar objects or surfaces are grouped into one class. Therefore variability within one class can be assumed. Only the question remains unknown, whether the variability within one class would also lead to diverging processes that drive  $\text{CO}_2$  fluxes. In the third assumption, we state that waterbody emissions of  $\text{CO}_2$  have a low spatial and temporal variability. Figures 26a and 26b show no diurnal cycle for the water  $\text{CO}_2$  fluxes. Nevertheless, figures 25a

and 25b show a large spread of values for water CO<sub>2</sub> fluxes, which could hint towards a spatial heterogeneity of water CO<sub>2</sub> fluxes. An analysis of the surface CO<sub>2</sub> concentration from multiple waterbodies would be useful to identify the cause of the spread in water CO<sub>2</sub> fluxes. A spatial heterogeneity has been shown for the waterbody concentration of CH<sub>4</sub> at this study site (Rehder et al., 2021). A similar heterogeneity of CO<sub>2</sub> concentration in the waterbodies would likely lead to heterogeneous CO<sub>2</sub> fluxes.



## BIBLIOGRAPHY

---

- Abnizova, A, J Siemens, M Langer, and J Boike (2012). "Small ponds with major impact: The relevance of ponds and lakes in permafrost landscapes to carbon dioxide emissions." In: *Global Biogeochemical Cycles* 26. ISSN: 0886-6236. DOI: [10.1029/2011gb004237](https://doi.org/10.1029/2011gb004237).
- Andresen, C. G. and V. L. Lougheed (2015). "Disappearing Arctic tundra ponds: Fine-scale analysis of surface hydrology in drained thaw lake basins over a 65 year period (1948–2013)." In: *Journal of Geophysical Research-Biogeosciences* 120.3, pp. 466–479. ISSN: 2169-8953. DOI: [10.1002/2014jg002778](https://doi.org/10.1002/2014jg002778).
- Andresen, Christian G., Mark J. Lara, Craig E. Tweedie, and Vanessa L. Lougheed (2017). "Rising plant-mediated methane emissions from arctic wetlands." In: *Global Change Biology*. ISSN: 13652486. DOI: [10.1111/gcb.13469](https://doi.org/10.1111/gcb.13469).
- Are, Feliks and Erk Reimnitz (2000). "An Overview of the Lena River Delta Setting: Geology, Tectonics, Geomorphology, and Hydrology." In: *Journal of Coastal Research* 16.4, pp. 1083–1093.
- Avagyan, Armine, Benjamin R.K. Runkle, and Lars Kutzbach (2014). "Application of high-resolution spectral absorbance measurements to determine dissolved organic carbon concentration in remote areas." In: *Journal of Hydrology* 517, pp. 435–446. ISSN: 0022-1694. DOI: [10.1016/j.jhydrol.2014.05.060](https://doi.org/10.1016/j.jhydrol.2014.05.060).
- Baldocchi, Dennis D (2003). "Assessing the eddy covariance technique for evaluating carbon dioxide exchange rates of ecosystems: past, present and future." In: *Global change biology* 9.4, pp. 479–492. DOI: [10.1046/j.1365-2486.2003.00629.x](https://doi.org/10.1046/j.1365-2486.2003.00629.x).
- Beckebanze, L., Z. Rehder, D. Holl, C. Wille, C. Mirbach, and L. Kutzbach (2022a). "Ignoring carbon emissions from thermokarst ponds results in overestimation of tundra net carbon uptake." In: *Biogeosciences* 19.4, pp. 1225–1244. DOI: [10.5194/bg-19-1225-2022](https://doi.org/10.5194/bg-19-1225-2022).
- Beckebanze, Lutz, Zoé Rehder, Rüggen Norman, David Holl, Charlotta Mirbach, Christian Wille, and Lars Kutzbach (2021). *Eddy-covariance and meteorological measurements of large pond and polygonal tundra in Lena River Delta, Siberia (summer 2019)*. data set. DOI: [10.1594/PANGAEA.937594](https://doi.org/10.1594/PANGAEA.937594).
- Beckebanze, Lutz, Benjamin RK Runkle, Josefine Walz, Christian Wille, David Holl, Manuel Helbig, Julia Boike, Torsten Sachs, and Lars Kutzbach (2022b). *Lateral and vertical carbon fluxes from the polygonal tundra in the Lena River Delta, Siberia (summer 2014)*. DOI: [10.1594/PANGAEA.944186](https://doi.org/10.1594/PANGAEA.944186).
- Bogard, Matthew J., Paul A. del Giorgio, Lennie Boutet, Maria Carolina Garcia Chaves, Yves T. Prairie, Anthony Merante, and Alison M.

- Derry (2014). "Oxic water column methanogenesis as a major component of aquatic CH<sub>4</sub> fluxes." In: *Nature Communications* 5.1, p. 5350. ISSN: 2041-1723. DOI: [10.1038/ncomms6350](https://doi.org/10.1038/ncomms6350).
- Boike, J et al. (2013). "Baseline characteristics of climate, permafrost and land cover from a new permafrost observatory in the Lena River Delta, Siberia (1998-2011)." In: *Biogeosciences* 10.3, pp. 2105–2128. DOI: [10.5194/bg-10-2105-2013](https://doi.org/10.5194/bg-10-2105-2013).
- Boike, J. et al. (2019). "A 16-year record (2002–2017) of permafrost, active-layer, and meteorological conditions at the Samoylov Island Arctic permafrost research site, Lena River delta, northern Siberia: an opportunity to validate remote-sensing data and land surface, snow, and permafrost models." In: *Earth System Science Data* 11.1, pp. 261–299. DOI: [10.5194/essd-11-261-2019](https://doi.org/10.5194/essd-11-261-2019).
- Boike, Julia, Reinhard Dietrich, Frank Günther, Moritz Langer, Konstanze Piel, Steffen Scheller, Marita Scheritz, and Waldemar Schneider (2012a). *Digital Elevation Model of Samoylov Island, Lena River Delta, Siberia, Russia, with link to ArcGIS files*. DOI: [10.1594/PANGAEA.802255](https://doi.org/10.1594/PANGAEA.802255).
- Boike, Julia, Maren Grüber, Moritz Langer, Konstanze Piel, and Marita Scheritz (2012b). *Orthomosaic of Samoylov Island, Lena Delta, Siberia*. data set. Alfred Wegener Institute - Research Unit Potsdam. DOI: [10.1594/PANGAEA.786073](https://doi.org/10.1594/PANGAEA.786073).
- Boike, Julia, Georg Veh, Günter Stoof, Maren Grüber, Moritz Langer, and Sina Muster (2015a). "Visible and near-infrared orthomosaic and orthophotos of Samoylov Island, Siberia, summer 2008, with links to data files." In: DOI: [10.1594/PANGAEA.847343](https://doi.org/10.1594/PANGAEA.847343).
- Boike, Julia, Georg Veh, Leena-Kaisa Viitanen, Niko Bornemann, Günter Stoof, and Sina Muster (2015b). *Visible and near-infrared orthomosaic of Samoylov Island, Siberia, summer 2015 (5.3 GB)*. data set. Alfred Wegener Institute - Research Unit Potsdam. DOI: [10.1594/PANGAEA.845724](https://doi.org/10.1594/PANGAEA.845724).
- Boike, Julia et al. (2015c). "Temperature, water level and bathymetry of thermokarst lakes in the continuous permafrost zone of northern Siberia - Lena River Delta, Siberia." In: DOI: [10.1594/PANGAEA.846525](https://doi.org/10.1594/PANGAEA.846525).
- Boike, Julia et al. (2019). "Meteorologic data at station Samoylov (2002-2018, level 2, version 201908), link to archive." In: PANGAEA. DOI: [10.1594/PANGAEA.905232](https://doi.org/10.1594/PANGAEA.905232).
- Borrel, Guillaume, Didier Jézéquel, Corinne Biderre-Petit, Nicole Morel-Desrosiers, Jean-Pierre Morel, Pierre Peyret, Gérard Fonty, and Anne-Catherine Lehours (2011). "Production and consumption of methane in freshwater lake ecosystems." In: *Research in Microbiology* 162.9, pp. 832–847. ISSN: 0923-2508. DOI: [10.1016/j.resmic.2011.06.004](https://doi.org/10.1016/j.resmic.2011.06.004).
- Bouchard, F., I. Laurion, V. Preskienis, D. Fortier, X. Xu, and M. J. Whiticar (2015). "Modern to millennium-old greenhouse gases

- emitted from ponds and lakes of the Eastern Canadian Arctic (Bylot Island, Nunavut)." In: *Biogeosciences* 12.23, pp. 7279–7298. ISSN: 17264189. DOI: [10.5194/bg-12-7279-2015](https://doi.org/10.5194/bg-12-7279-2015).
- Boucher, Olivier, Pierre Friedlingstein, Bill Collins, and Keith P Shine (2009). "The indirect global warming potential and global temperature change potential due to methane oxidation." In: *Environmental Research Letters* 4.4, p. 044007. DOI: [10.1088/1748-9326/4/4/044007](https://doi.org/10.1088/1748-9326/4/4/044007).
- Bring, A. et al. (2016). "Arctic terrestrial hydrology: A synthesis of processes, regional effects, and research challenges." In: *Journal of Geophysical Research-Biogeosciences* 121.3, pp. 621–649. ISSN: 2169-8953. DOI: [10.1002/2015jg003131](https://doi.org/10.1002/2015jg003131).
- Burba, George (2021). *Eddy Covariance Method for Scientific, Regulatory, and Commercial Applications*. LI-COR Biosciences.
- Burba, George et al. (2012). "Calculating CO<sub>2</sub> and H<sub>2</sub>O eddy covariance fluxes from an enclosed gas analyzer using an instantaneous mixing ratio." In: *Global Change Biology* 18.1, pp. 385–399. ISSN: 13541013. DOI: [10.1111/j.1365-2486.2011.02536.x](https://doi.org/10.1111/j.1365-2486.2011.02536.x).
- Campeau, Audrey, Kevin H. Bishop, Michael F. Billett, Mark H. Garnett, Hjalmar Laudon, Jason A. Leach, Mats B. Nilsson, Mats G. Öquist, and Marcus B. Wallin (2017). "Aquatic export of young dissolved and gaseous carbon from a pristine boreal fen: Implications for peat carbon stock stability." In: *Global Change Biology* 23.12, pp. 5523–5536. ISSN: 13652486. DOI: [10.1111/gcb.13815](https://doi.org/10.1111/gcb.13815).
- Canadell, J.G. et al. (2021). "Global Carbon and other Biogeochemical Cycles and Feedbacks." In: *Climate Change 2021: The Physical Science Basis. Contribution of Working Group I to the Sixth Assessment Report of the Intergovernmental Panel on Climate Change*. Ed. by V. Masson-Delmotte et al. Cambridge, United Kingdom and New York, NY, USA: Cambridge University Press, 673–816.
- Chapin, F SIII et al. (2006). "Reconciling carbon-cycle concepts, terminology, and methods." In: *Ecosystems* 9.7, pp. 1041–1050. DOI: [10.1007/s10021-005-0105-7](https://doi.org/10.1007/s10021-005-0105-7).
- Chi, Jinshu et al. (2020). "The Net Landscape Carbon Balance—Integrating terrestrial and aquatic carbon fluxes in a managed boreal forest landscape in Sweden." In: *Global Change Biology* 26.4, pp. 2353–2367. DOI: [10.1111/gcb.14983](https://doi.org/10.1111/gcb.14983).
- Cicerone, R. J. and R. S. Oremland (1988). "Biogeochemical aspects of atmospheric methane." In: *Global Biogeochemical Cycles* 2.4, pp. 299–327. DOI: [10.1029/GB002i004p00299](https://doi.org/10.1029/GB002i004p00299).
- Clark, Peter U., Arthur S. Dyke, Jeremy D. Shakun, Anders E. Carlson, Jorie Clark, Barbara Wohlfarth, Jerry X. Mitrovica, Steven W. Hostetler, and A. Marshall McCabe (2009). "The Last Glacial Maximum." In: *Science* 325.5941, pp. 710–714. DOI: [10.1126/science.1172873](https://doi.org/10.1126/science.1172873).

- Conrad, R. (1999). "Contribution of hydrogen to methane production and control of hydrogen concentrations in methanogenic soils and sediments." In: *FEMS Microbiology Ecology* 28.3, pp. 193–202. DOI: [10.1016/S0168-6496\(98\)00086-5](https://doi.org/10.1016/S0168-6496(98)00086-5).
- Cory, RM, KH Harrold, BT Neilson, and GW Kling (2015). "Controls on dissolved organic matter (DOM) degradation in a headwater stream: the influence of photochemical and hydrological conditions in determining light-limitation or substrate-limitation of photo-degradation." In: *Biogeosciences* 12.22, pp. 6669–6685. DOI: [10.5194/bg-12-6669-2015](https://doi.org/10.5194/bg-12-6669-2015).
- Cory, Rose M, Collin P Ward, Byron C Crump, and George W Kling (2014). "Sunlight controls water column processing of carbon in arctic fresh waters." In: *Science* 345.6199, pp. 925–928. DOI: [10.1126/science.1253119](https://doi.org/10.1126/science.1253119).
- Dodds, Walter K. and Matt R. Whiles (2010). "Chapter 13 - Carbon." In: *Freshwater Ecology (Second Edition)*. Ed. by Walter K. Dodds and Matt R. Whiles. Second Edition. Aquatic Ecology. London: Academic Press, pp. 323–343. ISBN: 978-0-12-374724-2. DOI: [10.1016/B978-0-12-374724-2.00013-1](https://doi.org/10.1016/B978-0-12-374724-2.00013-1).
- Donis, D., S. Flury, A. Stöckli, J. E. Spangenberg, D. Vachon, and D. F. McGinnis (2017). "Full-scale evaluation of methane production under oxic conditions in a mesotrophic lake." In: *Nature Communications* 8.1, p. 1661. ISSN: 2041-1723. DOI: [10.1038/s41467-017-01648-4](https://doi.org/10.1038/s41467-017-01648-4).
- Drake, Travis W, Kimberly P Wickland, Robert GM Spencer, Diane M McKnight, and Robert G Striegl (2015). "Ancient low-molecular-weight organic acids in permafrost fuel rapid carbon dioxide production upon thaw." In: *Proceedings of the National Academy of Sciences* 112.45, pp. 13946–13951. DOI: [10.1073/pnas.1511705112](https://doi.org/10.1073/pnas.1511705112).
- Draper, Norman R and Harry Smith (2014). *Applied regression analysis*. Vol. 326. John Wiley & Sons.
- Ducharme-Riel, Véronique, Dominic Vachon, Paul A. del Giorgio, and Yves T. Prairie (2015). "The relative contribution of winter under-ice and summer hypolimnetic CO<sub>2</sub> accumulation to the annual CO<sub>2</sub> emissions from northern lakes." In: *Ecosystems* 18.4, pp. 547–559. ISSN: 14350629. DOI: [10.1007/s10021-015-9846-0](https://doi.org/10.1007/s10021-015-9846-0).
- Eckhardt, Tim, Christian Knoblauch, Lars Kutzbach, David Holl, Gillian Simpson, Evgeny Abakumov, and Eva Maria Pfeiffer (2019). "Partitioning net ecosystem exchange of CO<sub>2</sub> on the pedon scale in the Lena River Delta, Siberia." In: *Biogeosciences* 16.7, pp. 1543–1562. ISSN: 17264189. DOI: [10.5194/bg-16-1543-2019](https://doi.org/10.5194/bg-16-1543-2019).
- Edgington, Eugene and Patrick Onghena (2007). *Randomization tests*. CRC Press.
- Ellis, Christopher J., Line Rochefort, Gilles Gauthier, and Reinhard Pienitz (2008). "Paleoecological evidence for transitions between contrasting landforms in a polygon-patterned high arctic wet-

- land." In: *Arctic, Antarctic, and Alpine Research* 40.4, pp. 624–637. DOI: [10.1657/1523-0430\(07-059\)\[ELLIS\]2.0.CO;2](https://doi.org/10.1657/1523-0430(07-059)[ELLIS]2.0.CO;2).
- Encinas Fernández, Jorge, Frank Peeters, and Hilmar Hofmann (2016). "On the methane paradox: Transport from shallow water zones rather than in situ methanogenesis is the major source of CH<sub>4</sub> in the open surface water of lakes." In: *Journal of Geophysical Research: Biogeosciences* 121.10, pp. 2717–2726. ISSN: 2169-8953. DOI: [10.1002/2016JG003586](https://doi.org/10.1002/2016JG003586).
- Environmental Systems Research Institute (ESRI) Redlands, CA (2012). *ARC GIS Release 10.1*.
- Eugster, Werner, George Kling, Tobias Jonas, Joseph P. McFadden, Alfred Wüest, Sally MacIntyre, and F. Stuart Chapin (2003). "CO<sub>2</sub> exchange between air and water in an Arctic Alaskan and mid-latitude Swiss lake: Importance of convective mixing." In: *Journal of Geophysical Research Atmospheres* 108.12. ISSN: 01480227. DOI: [10.1029/2002JD002653](https://doi.org/10.1029/2002JD002653).
- Fan, Song-Miao, Steven C. Wofsy, Peter S. Bakwin, Daniel J. Jacob, and David R. Fitzjarrald (1990). "Atmosphere-biosphere exchange of CO<sub>2</sub> and O<sub>3</sub> in the central Amazon Forest." In: *Journal of Geophysical Research: Atmospheres* 95.D10, pp. 16851–16864. DOI: [10.1029/JD095iD10p16851](https://doi.org/10.1029/JD095iD10p16851).
- Finkelstein, Peter L. and Pamela F. Sims (2001). "Sampling error in eddy correlation flux measurements." In: *Journal of Geophysical Research: Atmospheres* 106.D4, pp. 3503–3509. DOI: [10.1029/2000JD900731](https://doi.org/10.1029/2000JD900731).
- Forster, P. et al. (2021). "The Earth's Energy Budget, Climate Feedbacks, and Climate Sensitivity." In: *Climate Change 2021: The Physical Science Basis. Contribution of Working Group I to the Sixth Assessment Report of the Intergovernmental Panel on Climate Change*. Ed. by V. Masson-Delmotte et al. Cambridge, United Kingdom and New York, NY, USA: Cambridge University Press, 923–1054.
- Fouché, Julien, Melissa J Lafrenière, Krysten Rutherford, and Scott Lamoureux (2017). "Seasonal hydrology and permafrost disturbance impacts on dissolved organic matter composition in High Arctic headwater catchments." In: *Arctic Science* 3.2, pp. 378–405. DOI: [10.1139/as-2016-0031](https://doi.org/10.1139/as-2016-0031).
- Fratini, Gerardo, Andreas Ibrom, Nicola Arriga, George Burba, and Dario Papale (2012). "Relative humidity effects on water vapour fluxes measured with closed-path eddy-covariance systems with short sampling lines." In: *Agricultural and forest meteorology* 165, pp. 53–63. DOI: [10.1016/j.agrformet.2012.05.018](https://doi.org/10.1016/j.agrformet.2012.05.018).
- Friedlingstein, P. et al. (2022). "Global Carbon Budget 2022." In: *Earth System Science Data* 14.11, pp. 4811–4900. DOI: [10.5194/essd-14-4811-2022](https://doi.org/10.5194/essd-14-4811-2022).

- Fuchs, Matthias et al. (2020). "Rapid Fluvio-Thermal Erosion of a Yedoma Permafrost Cliff in the Lena River Delta." In: *Frontiers in Earth Science* 8. ISSN: 2296-6463. DOI: [10.3389/feart.2020.00336](https://doi.org/10.3389/feart.2020.00336).
- GTNP Database (2019). <https://gtnp.arcticportal.org/>, access in February 2019.
- Gash, J. H. C. and A. D. Culf (1996). "Applying a linear detrend to eddy correlation data in realtime." In: *Boundary-Layer Meteorology* 79.3, pp. 301–306. ISSN: 0006-8314. DOI: [10.1007/bf00119443](https://doi.org/10.1007/bf00119443).
- Günthel, Marco et al. (2020). "Photosynthesis-driven methane production in oxic lake water as an important contributor to methane emission." In: *Limnology and Oceanography* 65.12, pp. 2853–2865. ISSN: 0024-3590. DOI: [10.1002/lno.11557](https://doi.org/10.1002/lno.11557).
- Harris, S.A., H.M. French, J.A. Heginbottom, G.H. Johnston B., Ladanyi, D.C. Sego, and R.O. van Everdingen (1988). "Glossary of permafrost and related ground-ice terms." In: *Associate Committee on Geotechnical Research, National Research Council of Canada, Ottawa* 156.
- Hedderich, Reiner and William B. Whitman (2006). "Physiology and biochemistry of the methane-producing Archaea." In: *The Prokaryotes: Volume 2: Ecophysiology and Biochemistry*. Ed. by Martin Dworkin, Stanley Falkow, Eugene Rosenberg, Karl-Heinz Schleifer, and Erko Stackebrandt. New York, NY: Springer New York, pp. 1050–1079. ISBN: 978-0-387-30742-8. DOI: [10.1007/0-387-30742-7\\_34](https://doi.org/10.1007/0-387-30742-7_34).
- Helbig, Manuel, Julia Boike, Moritz Langer, Peter Schreiber, Benjamin R. K. Runkle, and Lars Kutzbach (2013). "Spatial and seasonal variability of polygonal tundra water balance: Lena River Delta, northern Siberia (Russia)." In: *Hydrogeology Journal* 21.1, pp. 133–147. DOI: [10.1007/s10040-012-0933-4](https://doi.org/10.1007/s10040-012-0933-4).
- Holgerson, Meredith A and Peter A Raymond (2016). "Large contribution to inland water CO<sub>2</sub> and CH<sub>4</sub> emissions from very small ponds." In: *Nature Geoscience* 9.3, pp. 222–226. ISSN: 1752-0894. DOI: [10.1038/ngeo2654](https://doi.org/10.1038/ngeo2654).
- Holl, D., V. Pancotto, A. Heger, S. J. Camargo, and L. Kutzbach (2019a). "Cushion bogs are stronger carbon dioxide net sinks than moss-dominated bogs as revealed by eddy covariance measurements on Tierra del Fuego, Argentina." In: *Biogeosciences* 16.17, pp. 3397–3423. DOI: [10.5194/bg-16-3397-2019](https://doi.org/10.5194/bg-16-3397-2019).
- Holl, D. et al. (2019b). "A long-term (2002 to 2017) record of closed-path and open-path eddy covariance CO<sub>2</sub> net ecosystem exchange fluxes from the Siberian Arctic." In: *Earth System Science Data* 11.1. ISSN: 18663516. DOI: [10.5194/essd-11-221-2019](https://doi.org/10.5194/essd-11-221-2019).
- Holl, David, Eva-Maria Pfeiffer, and Lars Kutzbach (2020). "Comparison of eddy covariance CO<sub>2</sub> and CH<sub>4</sub> fluxes from mined and recently rewetted sections in a northwestern German cutover bog." In: *Biogeosciences* 17.10, pp. 2853–2874. DOI: [10.5194/bg-17-2853-2020](https://doi.org/10.5194/bg-17-2853-2020).

- Holl, David et al. (2018). *A long-term (2002 to 2017) record of closed path and open path eddy covariance CO<sub>2</sub> net ecosystem exchange fluxes from the Siberian Arctic*. DOI: [10.1594/PANGAEA.892751](https://doi.org/10.1594/PANGAEA.892751).
- Hugelius, G. et al. (2014). "Estimated stocks of circumpolar permafrost carbon with quantified uncertainty ranges and identified data gaps." In: *Biogeosciences* 11.23, pp. 6573–6593. DOI: [10.5194/bg-11-6573-2014](https://doi.org/10.5194/bg-11-6573-2014).
- Hutchins, Ryan H.S., Yves T. Prairie, and Paul A. del Giorgio (2019). "Large-Scale Landscape Drivers of CO<sub>2</sub>, CH<sub>4</sub>, DOC, and DIC in Boreal River Networks." In: *Global Biogeochemical Cycles* 33.2, pp. 125–142. ISSN: 19449224. DOI: [10.1029/2018GB006106](https://doi.org/10.1029/2018GB006106).
- ICOS (2022). *ICOS - Standardised Greenhouse Gas Measurements throughout Europe*. URL: <https://www.icos-cp.eu/> (visited on 11/14/2022).
- IPCC (2021). "Summary for Policymakers." In: *Climate Change 2021: The Physical Science Basis. Contribution of Working Group I to the Sixth Assessment Report of the Intergovernmental Panel on Climate Change*. Ed. by V. Masson-Delmotte et al. Cambridge, United Kingdom and New York, NY, USA: Cambridge University Press, pp. 3–32.
- Ibrom, Andreas, Ebba Dellwik, Henrik Flyvbjerg, Niels Otto Jensen, and Kim Pilegaard (2007a). "Strong low-pass filtering effects on water vapour flux measurements with closed-path eddy correlation systems." In: *Agricultural and Forest Meteorology* 147.3, pp. 140–156. ISSN: 0168-1923. DOI: [10.1016/j.agrformet.2007.07.007](https://doi.org/10.1016/j.agrformet.2007.07.007).
- Ibrom, Andreas, Ebba Dellwik, Søren Ejling Larsen, and Kim Pilegaard (2007b). "On the use of the Webb-Pearman-Leuning theory for closed-path eddy correlation measurements." In: *Tellus, Series B: Chemical and Physical Meteorology* 59.5, pp. 937–946. ISSN: 02806509. DOI: [10.1111/j.1600-0889.2007.00311.x](https://doi.org/10.1111/j.1600-0889.2007.00311.x).
- Iwata, Hiroki, Ryuichi Hirata, Yoshiyuki Takahashi, Yuichi Miyabara, Masayuki Itoh, and Kotaro Iizuka (2018). "Partitioning eddy-covariance methane fluxes from a shallow lake into diffusive and ebullitive fluxes." In: *Boundary-Layer Meteorology* 169.3, pp. 413–428. ISSN: 15731472. DOI: [10.1007/s10546-018-0383-1](https://doi.org/10.1007/s10546-018-0383-1).
- Jammet, Mathilde, Sigrid Dengel, Ernesto Kettner, Frans-Jan W. Parmentier, Martin Wik, Patrick Crill, and Thomas Friborg (2017). "Year-round CH<sub>2</sub> and CO<sub>2</sub> flux dynamics in two contrasting freshwater ecosystems of the subarctic." In: *Biogeosciences* 14.22, pp. 5189–5216. ISSN: 1726-4189. DOI: [10.5194/bg-14-5189-2017](https://doi.org/10.5194/bg-14-5189-2017).
- Jansen, J., B. F. Thornton, M. M. Jammet, M. Wik, A. Cortés, T. Friborg, S. MacIntyre, and P. M. Crill (2019). "Climate-sensitive controls on large spring emissions of CH<sub>4</sub> and CO<sub>2</sub> from northern lakes." In: *Journal of Geophysical Research: Biogeosciences* 124.7, pp. 2379–2399. ISSN: 21698961. DOI: [10.1029/2019JG005094](https://doi.org/10.1029/2019JG005094).
- Jonsson, Anders, J. Åberg, A. Lindroth, and M. Jansson (2008). "Gas transfer rate and CO<sub>2</sub> flux between an unproductive lake and the atmosphere in northern Sweden." In: *Journal of Geophysical*

- Research: Biogeosciences* 113.4, pp. 1–13. ISSN: 01480227. DOI: [10.1029/2008JG000688](https://doi.org/10.1029/2008JG000688).
- Juutinen, S. et al. (2022). "Variation in CO<sub>2</sub> and CH<sub>4</sub> fluxes among land cover types in heterogeneous Arctic tundra in northeastern Siberia." In: *Biogeosciences* 19.13, pp. 3151–3167. DOI: [10.5194/bg-19-3151-2022](https://doi.org/10.5194/bg-19-3151-2022).
- Kaimal, Jagadish Chandran and John J Finnigan (1994). *Atmospheric boundary layer flows: their structure and measurement*. Oxford university press.
- Kanevskiy, Mikhail, Yuri Shur, Jens Strauss, Torre Jorgenson, Daniel Fortier, Eva Stephani, and Alexander Vasiliev (2016). "Patterns and rates of riverbank erosion involving ice-rich permafrost (yedoma) in northern Alaska." In: *Geomorphology* 253, pp. 370–384. ISSN: 0169-555X. DOI: [10.1016/j.geomorph.2015.10.023](https://doi.org/10.1016/j.geomorph.2015.10.023).
- Kartoziia, Andrei (2019). "Assessment of the ice wedge polygon current state by means of UAV imagery analysis (Samoylov Island, the Lena Delta)." In: *Remote Sensing* 11.13, p. 1627. DOI: [10.3390/rs11131627](https://doi.org/10.3390/rs11131627).
- Kling, George W., George W. Kipphut, and Michael C. Miller (1992). "The flux of CO<sub>2</sub> and CH<sub>4</sub> from lakes and rivers in arctic Alaska." In: *Hydrobiologia* 240.1-3, pp. 23–36. ISSN: 00188158. DOI: [10.1007/BF00013449](https://doi.org/10.1007/BF00013449).
- Kling, George W, George W Kipphut, Michael M Miller, and John O'Brien W (2000). "Integration of lakes and streams in a landscape perspective: the importance of material processing on spatial patterns and temporal coherence." In: *Freshwater Biology* 43.3, pp. 477–497. ISSN: 0046-5070. DOI: [10.1046/j.1365-2427.2000.00515.x](https://doi.org/10.1046/j.1365-2427.2000.00515.x).
- Knoblauch, C, O Spott, S Evgrafova, L Kutzbach, and E M Pfeiffer (2015). "Regulation of methane production, oxidation, and emission by vascular plants and bryophytes in ponds of the northeast Siberian polygonal tundra." In: *Journal of Geophysical Research-Biogeosciences* 120.12, pp. 2525–2541. ISSN: 2169-8953. DOI: [10.1002/2015jg003053](https://doi.org/10.1002/2015jg003053).
- Kormann, Robert and Franz X Meixner (2001). "An analytical footprint model for non-neutral stratification." In: *Boundary-Layer Meteorology* 99.2, pp. 207–224. DOI: [10.1023/A:1018991015119](https://doi.org/10.1023/A:1018991015119).
- Koven, Charles D et al. (2015). "A simplified, data-constrained approach to estimate the permafrost carbon–climate feedback." In: *Philos. Trans. Royal Soc. A* 373.2054, p. 20140423. DOI: [10.1098/rsta.2014.0423](https://doi.org/10.1098/rsta.2014.0423).
- Kuhn, McKenzie, Erik J. Lundin, Reiner Giesler, Margareta Johansson, and Jan Karlsson (2018). "Emissions from thaw ponds largely offset the carbon sink of northern permafrost wetlands." In: *Scientific Reports* 8.1, pp. 1–7. ISSN: 20452322. DOI: [10.1038/s41598-018-27770-x](https://doi.org/10.1038/s41598-018-27770-x).

- Kulin, Gershon and Philip R Compton (1975). *A guide to methods and standards for the measurement of water flow*. 421. US Dept. of Commerce, National Bureau of Standards.
- Kutzbach, L., C. Wille, and E. M. Pfeiffer (2007). "The exchange of carbon dioxide between wet arctic tundra and the atmosphere at the Lena River Delta, Northern Siberia." In: *Biogeosciences* 4.5, pp. 869–890. ISSN: 17264189. DOI: [10.5194/bg-4-869-2007](https://doi.org/10.5194/bg-4-869-2007).
- Kutzbach, Lars (2006). "The exchange of energy, water and carbon dioxide between wet arctic tundra and the atmosphere at the Lena River Delta, Northern Siberia = Der Austausch von Energie, Wasser und Kohlendioxid zwischen arktischer Feuchtgebiets-Trundra und der Atmosphäre im nordsibirischen Lena Delta." PhD thesis. Universität Hamburg.
- LI-COR (2019). *EddyPro Version 7.0.6*.
- Lara, MJ, AD McGuire, ES Euskirchen, H Genet, S Yi, R Rutter, C Iversen, V Sloan, and SD Wullschleger (2020). "Local-scale Arctic tundra heterogeneity affects regional-scale carbon dynamics." In: *Nature communications* 11.1, pp. 1–10. DOI: [10.1038/s41467-020-18768-z](https://doi.org/10.1038/s41467-020-18768-z).
- Lee, Xuhui, William Massman, and Beverly Law (2006). *Handbook of micrometeorology: a guide for surface flux measurement and analysis*. Vol. 29. Springer Science & Business Media.
- Liljedahl, Anna K et al. (2016). "Pan-Arctic ice-wedge degradation in warming permafrost and its influence on tundra hydrology." In: *Nature Geoscience* 9.4, pp. 312–318. DOI: [10.1038/ngeo2674](https://doi.org/10.1038/ngeo2674).
- Liss, P. S. and P. G. Slater (1974). "Flux of gases across the Air-Sea interface." In: *Nature* 247.5438, pp. 181–184. ISSN: 00280836. DOI: [10.1038/247181a0](https://doi.org/10.1038/247181a0).
- Lougheed, V. L., C. E. Tweedie, C. G. Andresen, A. M. Armendariz, S. M. Escarzaga, and G. Tarin (2020). "Patterns and Drivers of Carbon Dioxide Concentrations in Aquatic Ecosystems of the Arctic Coastal Tundra." In: *Global Biogeochemical Cycles* 34.3, pp. 1–13. ISSN: 19449224. DOI: [10.1029/2020GB006552](https://doi.org/10.1029/2020GB006552).
- Lundin, Erik J., Reiner Giesler, Andreas Persson, Megan S. Thompson, and Jan Karlsson (2013). "Integrating carbon emissions from lakes and streams in a subarctic catchment." In: *Journal of Geophysical Research: Biogeosciences* 118.3, pp. 1200–1207. ISSN: 21698961. DOI: [10.1002/jgrg.20092](https://doi.org/10.1002/jgrg.20092).
- Lundin, Erik J., Jonatan Klaminder, Reiner Giesler, Andreas Persson, David Olefeldt, Michal Heliasz, Torben R. Christensen, and Jan Karlsson (2016). "Is the subarctic landscape still a carbon sink? Evidence from a detailed catchment balance." In: *Geophysical Research Letters* 43.5, pp. 1988–1995. DOI: [10.1002/2015GL066970](https://doi.org/10.1002/2015GL066970).
- MATLAB Deep Learning Toolbox* (2019b). The MathWorks, Natick, MA, USA.

- MATLAB (2019). *MATLAB Software 2019b*. The MathWorks, Natick, MA, USA.
- Magnússon, Rúna Í., Juul Limpens, David Kleijn, Ko van Huissteden, Trofim C. Maximov, Sylvain Lobry, and Monique M.P.D. Heijmans (2021). "Shrub decline and expansion of wetland vegetation revealed by very high resolution land cover change detection in the Siberian lowland tundra." In: *Science of The Total Environment* 782, p. 146877. ISSN: 0048-9697. DOI: [10.1016/j.scitotenv.2021.146877](https://doi.org/10.1016/j.scitotenv.2021.146877).
- Mann, Paul J, Timothy I Eglinton, Cameron P McIntyre, Nikita Zimov, Anna Davydova, Jorien E Vonk, Robert M Holmes, and Robert GM Spencer (2015). "Utilization of ancient permafrost carbon in headwaters of Arctic fluvial networks." In: *Nature Communications* 6.1, pp. 1–7. DOI: [10.1038/ncomms8856](https://doi.org/10.1038/ncomms8856).
- Mastepanov, M., C. Sigsgaard, T. Tagesson, L. Ström, M. P. Tamstorf, M. Lund, and T. R. Christensen (2013). "Revisiting factors controlling methane emissions from high-Arctic tundra." In: *Biogeosciences* 10.7, pp. 5139–5158. DOI: [10.5194/bg-10-5139-2013](https://doi.org/10.5194/bg-10-5139-2013).
- Mauder, M and T Foken (2004). "Documentation and instruction manual of the eddy covariance software package TK2, Univ." In: *Bayreuth, Abt. Mikrometeorol., ISSN 161489166*, pp. 26–42.
- McGuire, A. D. et al. (2012). "An assessment of the carbon balance of Arctic tundra: Comparisons among observations, process models, and atmospheric inversions." In: *Biogeosciences* 9.8, pp. 3185–3204. ISSN: 17264170. DOI: [10.5194/bg-9-3185-2012](https://doi.org/10.5194/bg-9-3185-2012).
- Mekonnen, Zelalem A et al. (2021). "Arctic tundra shrubification: a review of mechanisms and impacts on ecosystem carbon balance." In: *Environmental Research Letters* 16.5, p. 053001. DOI: [10.1088/1748-9326/abf28b](https://doi.org/10.1088/1748-9326/abf28b).
- Meredith, M. et al. (2019). "Polar Regions. In: IPCC Special Report on the Ocean and Cryosphere in a Changing Climate." In: ed. by H.-O. Pörtner et al. Cambridge, United Kingdom and New York, NY, USA: Cambridge University Press, pp. 203–320. DOI: [10.1017/9781009157964.005](https://doi.org/10.1017/9781009157964.005).
- Mirbach, Charlotta, Zoé Rehder, Lars Kutzbach, and Julia Boike (2022). *Land cover and polygonal pond classification of the Holocene Terrace on Samoylov Island*. data set. DOI: [10.1594/PANGAEA.944071](https://doi.org/10.1594/PANGAEA.944071).
- Mishra, Umakant et al. (2021). "Spatial heterogeneity and environmental predictors of permafrost region soil organic carbon stocks." In: *Science Advances* 7.9, eaaz5236. DOI: [10.1126/sciadv.aaz5236](https://doi.org/10.1126/sciadv.aaz5236).
- Moncrieff, John, Robert Clement, John Finnigan, and Tilden Meyers (2004). "Averaging, detrending, and filtering of eddy covariance time series." In: *Handbook of micrometeorology*. Springer, pp. 7–31. DOI: [10.1007/1-4020-2265-4\\_2](https://doi.org/10.1007/1-4020-2265-4_2).
- Muster, Sina, Moritz Langer, Birgit Heim, Sebastian Westermann, and Julia Boike (2012). "Subpixel heterogeneity of ice-wedge polygonal

- tundra: a multi-scale analysis of land cover and evapotranspiration in the Lena River Delta, Siberia." In: *Tellus B: Chemical and Physical Meteorology* 64.1, p. 17301. DOI: [10.3402/tellusb.v64i0.17301](https://doi.org/10.3402/tellusb.v64i0.17301).
- Muster, Sina et al. (2017). "PeRL: a circum-Arctic Permafrost Region Pond and Lake database." In: *Earth System Science Data* 9.1, pp. 317–348. ISSN: 1866-3516. DOI: [10.5194/essd-9-317-2017](https://doi.org/10.5194/essd-9-317-2017).
- Neff, Jason C. and Gregory P. Asner (2001). "Dissolved organic carbon in terrestrial ecosystems: Synthesis and a model." In: *Ecosystems* 4.1, pp. 29–48. ISSN: 14329840. DOI: [10.1007/s100210000058](https://doi.org/10.1007/s100210000058).
- Nitzbon, J., M. Langer, S. Westermann, L. Martin, K. S. Aas, and J. Boike (2019). "Pathways of ice-wedge degradation in polygonal tundra under different hydrological conditions." In: *The Cryosphere* 13.4, pp. 1089–1123. DOI: [10.5194/tc-13-1089-2019](https://doi.org/10.5194/tc-13-1089-2019).
- O'Donnell, Jonathan A., Michael P. Carey, Joshua C. Koch, Xiaomei Xu, Brett A. Poulin, Jennifer Walker, and Christian E. Zimmerman (2019). "Permafrost Hydrology Drives the Assimilation of Old Carbon by Stream Food Webs in the Arctic." In: *Ecosystems* 23.2, pp. 435–453. ISSN: 14350629. DOI: [10.1007/s10021-019-00413-6](https://doi.org/10.1007/s10021-019-00413-6).
- Obu, J. (2021). "How Much of the Earth's Surface is Underlain by Permafrost?" In: *Journal of Geophysical Research: Earth Surface* 126.5, e2021JF006123. DOI: [10.1029/2021JF006123](https://doi.org/10.1029/2021JF006123).
- Olefeldt, David and Nigel T Roulet (2012). "Effects of permafrost and hydrology on the composition and transport of dissolved organic carbon in a subarctic peatland complex." In: *Journal of Geophysical Research: Biogeosciences* 117.G1, G01005. DOI: [10.1029/2011JG001819](https://doi.org/10.1029/2011JG001819).
- Olefeldt, David and Nigel T. Roulet (2014). "Permafrost conditions in peatlands regulate magnitude, timing, and chemical composition of catchment dissolved organic carbon export." In: *Global Change Biology* 20.10, pp. 3122–3136. DOI: [10.1111/gcb.12607](https://doi.org/10.1111/gcb.12607).
- Öquist, M. G. et al. (2014). "The Full Annual Carbon Balance of Boreal Forests Is Highly Sensitive to Precipitation." In: *Environmental Science & Technology Letters* 1.7, pp. 315–319. DOI: [10.1021/ez500169j](https://doi.org/10.1021/ez500169j).
- Pastorello, Gilberto, Carlo Trotta, Eleonora Canfora, Housen Chu, Danielle Christianson, You-Wei Cheah, Cristina Poindexter, Jiquan Chen, and Abdelrahman et al. Elbashandy (July 2020). "The FLUXNET2015 dataset and the ONEFlux processing pipeline for eddy covariance data." In: *Scientific Data* 7.1, p. 225. ISSN: 2052-4463. DOI: [10.1038/s41597-020-0534-3](https://doi.org/10.1038/s41597-020-0534-3).
- Peeters, Frank, Jorge Encinas Fernandez, and Hilmar Hofmann (2019). "Sediment fluxes rather than oxic methanogenesis explain diffusive CH<sub>4</sub> emissions from lakes and reservoirs." In: *Scientific Reports* 9.1, p. 243. ISSN: 2045-2322. DOI: [10.1038/s41598-018-36530-w](https://doi.org/10.1038/s41598-018-36530-w).
- Pfeiffer, Eva-Maria and Mikhail N Grigoriev (2002). "Russian-German Cooperation SYSTEM LAPTEV-SEA 2000: The Expedition LENA

- 2001." In: *Berichte zur Polar-und Meeresforschung (Reports on Polar and Marine Research)* 426.
- Ramsar Convention Secretariat (2016). *An introduction to the Ramsar convention on wetlands (previously The Ramsar Convention Manual)*. Ramsar Convention Secretariat, Gland, Switzerland.
- Rehder, Zoé, Anna Zaplavnova, and Lars Kutzbach (2021). "Identifying drivers behind spatial variability of methane concentrations in East Siberian ponds." In: *Frontiers in Earth Science* 9, p. 183. DOI: [10.3389/feart.2021.617662](https://doi.org/10.3389/feart.2021.617662).
- Rehder, Zoé (2022). "Measuring and modeling of methane emissions from ponds in high latitudes." PhD thesis. Universität Hamburg. DOI: [10.17617/2.3384362](https://doi.org/10.17617/2.3384362).
- Repo, Maija E., J. T. Huttunen, A. V. Naumov, A. V. Chichulin, E. D. Lapshina, W. Bleuten, and P. J. Martikainen (2007). "Release of CO<sub>2</sub> and CH<sub>4</sub> from small wetland lakes in western Siberia." In: *Tellus, Series B: Chemical and Physical Meteorology* 59.5, pp. 788–796. ISSN: 02806509. DOI: [10.1111/j.1600-0889.2007.00301.x](https://doi.org/10.1111/j.1600-0889.2007.00301.x).
- Rodenhizer, Heidi, Fay Belshe, Gerardo Celis, Justin Ledman, Marguerite Mauritz, Scott Goetz, Temuulen Sankey, and Edward A.G. Schuur (2022). "Abrupt permafrost thaw accelerates carbon dioxide and methane release at a tussock tundra site." In: *Arctic, Antarctic, and Alpine Research* 54.1, pp. 443–464. DOI: [10.1080/15230430.2022.2118639](https://doi.org/10.1080/15230430.2022.2118639).
- Rößger, Norman, Torsten Sachs, Christian Wille, Julia Boike, and Lars Kutzbach (2022). "Seasonal increase of methane emissions linked to warming in Siberian tundra." In: *Nature Climate Change*, pp. 1–6. DOI: [10.1038/s41558-022-01512-4](https://doi.org/10.1038/s41558-022-01512-4).
- Rößger, Norman, Christian Wille, David Holl, Mathias Göckede, and Lars Kutzbach (2019a). "Scaling and balancing carbon dioxide fluxes in a heterogeneous tundra ecosystem of the Lena River Delta." In: *Biogeosciences* 16.13, pp. 2591–2615. ISSN: 17264189. DOI: [10.5194/bg-16-2591-2019](https://doi.org/10.5194/bg-16-2591-2019).
- Rößger, Norman, Christian Wille, Georg Veh, Julia Boike, and Lars Kutzbach (2019b). "Scaling and balancing methane fluxes in a heterogeneous tundra ecosystem of the Lena River Delta." In: *Agricultural and Forest Meteorology* 266-267. August 2017, pp. 243–255. ISSN: 01681923. DOI: [10.1016/j.agrformet.2018.06.026](https://doi.org/10.1016/j.agrformet.2018.06.026).
- Runkle, B. R.K., T. Sachs, C. Wille, E. M. Pfeiffer, and L. Kutzbach (2013). "Bulk partitioning the growing season net ecosystem exchange of CO<sub>2</sub> in Siberian tundra reveals the seasonality of its carbon sequestration strength." In: *Biogeosciences* 10.3, pp. 1337–1349. ISSN: 17264189. DOI: [10.5194/bg-10-1337-2013](https://doi.org/10.5194/bg-10-1337-2013).
- Sachs, Torsten, Christian Wille, Julia Boike, and Lars Kutzbach (2008). "Environmental controls on ecosystem-scale CH<sub>4</sub> emission from polygonal tundra in the Lena River Delta, Siberia." In: *Journal of Geophysical Research: Biogeosciences* 113.G3. DOI: [10.1029/2007JG000505](https://doi.org/10.1029/2007JG000505).

- Saunois, M. et al. (2020). "The Global Methane Budget 2000–2017." In: *Earth System Science Data* 12.3, pp. 1561–1623. DOI: [10.5194/essd-12-1561-2020](https://doi.org/10.5194/essd-12-1561-2020).
- Schneider, Julia, Guido Grosse, and Dirk Wagner (2009). "Land cover classification of tundra environments in the Arctic Lena Delta based on Landsat 7 ETM+ data and its application for upscaling of methane emissions." In: *Remote Sensing of Environment* 113.2, pp. 380–391. DOI: [10.1016/j.rse.2008.10.013](https://doi.org/10.1016/j.rse.2008.10.013).
- Schuur, Edward AG et al. (2015). "Climate change and the permafrost carbon feedback." In: DOI: [10.1038/nature14338](https://doi.org/10.1038/nature14338).
- Schuur, Edward A.G. et al. (2022). "Permafrost and Climate Change: Carbon Cycle Feedbacks From the Warming Arctic." In: *Annual Review of Environment and Resources* 47.1, pp. 343–371. DOI: [10.1146/annurev-environ-012220-011847](https://doi.org/10.1146/annurev-environ-012220-011847).
- Schwamborn, Georg, Volker Rachold, and Mikhail N Grigoriev (2002). "Late Quaternary sedimentation history of the Lena Delta." In: *Quaternary International* 89.1, pp. 119–134. DOI: [10.1016/S1040-6182\(01\)00084-2](https://doi.org/10.1016/S1040-6182(01)00084-2).
- Sepulveda-Jauregui, A., K. M. Walter Anthony, K. Martinez-Cruz, S. Greene, and F. Thalasso (2015). "Methane and carbon dioxide emissions from 40 lakes along a north-south latitudinal transect in Alaska." In: *Biogeosciences* 12.11, pp. 3197–3223. ISSN: 17264189. DOI: [10.5194/bg-12-3197-2015](https://doi.org/10.5194/bg-12-3197-2015).
- Sieczko, Anna K., Nguyen Thanh Duc, Jonathan Schenk, Gustav Pajala, David Rudberg, Henrique O. Sawakuchi, and David Bastviken (2020). "Diel variability of methane emissions from lakes." In: *Proceedings of the National Academy of Sciences* 117.35, pp. 21488–21494. ISSN: 0027-8424. DOI: [10.1073/pnas.2006024117](https://doi.org/10.1073/pnas.2006024117).
- Spencer, Robert GM, Paul J Mann, Thorsten Dittmar, Timothy I Eglinton, Cameron McIntyre, R Max Holmes, Nikita Zimov, and Aron Stubbins (2015). "Detecting the signature of permafrost thaw in Arctic rivers." In: *Geophysical Research Letters* 42.8, pp. 2830–2835. DOI: [10.1002/2015GL063498](https://doi.org/10.1002/2015GL063498).
- Squires, Margaret M. and Lance F.W. Lesack (2003). "The relation between sediment nutrient content and macrophyte biomass and community structure along a water transparency gradient among lakes of the Mackenzie Delta." In: *Canadian Journal of Fisheries and Aquatic Sciences* 60.3, pp. 333–343. ISSN: 0706652X. DOI: [10.1139/f03-027](https://doi.org/10.1139/f03-027).
- Stolpmann, Lydia, Gesine Mollenhauer, Anne Morgenstern, Jens S. Hammes, Julia Boike, Pier Paul Overduin, and Guido Grosse (2022). "Origin and Pathways of Dissolved Organic Carbon in a Small Catchment in the Lena River Delta." In: *Frontiers in Earth Science* 9. ISSN: 2296-6463. DOI: [10.3389/feart.2021.759085](https://doi.org/10.3389/feart.2021.759085).
- Treat, Claire C. et al. (2018). "Tundra landscape heterogeneity, not interannual variability, controls the decadal regional carbon balance

- in the Western Russian Arctic." In: *Global Change Biology* 24.11, pp. 5188–5204. ISSN: 13652486. DOI: [10.1111/gcb.14421](https://doi.org/10.1111/gcb.14421).
- Tuovinen, J.-P., M. Aurela, J. Hatakka, A. Räsänen, T. Virtanen, J. Mikola, V. Ivakhov, V. Kondratyev, and T. Laurila (2019). "Interpreting eddy covariance data from heterogeneous Siberian tundra: land-cover-specific methane fluxes and spatial representativeness." In: *Biogeosciences* 16.2, pp. 255–274. DOI: [10.5194/bg-16-255-2019](https://doi.org/10.5194/bg-16-255-2019).
- Turetsky, Merritt R et al. (2020). "Carbon release through abrupt permafrost thaw." In: *Nature Geoscience* 13.2, pp. 138–143. DOI: [10.1038/s41561-019-0526-0](https://doi.org/10.1038/s41561-019-0526-0).
- U.S. Geological Survey, EROS Center (1965). *CORONA Satellite Photographs*.
- Van Huissteden, J (2020). *Thawing permafrost*. Springer. DOI: [10.1007/978-3-030-31379-1](https://doi.org/10.1007/978-3-030-31379-1).
- Vickers, Dean and L. Mahrt (1997). "Quality control and flux sampling problems for tower and aircraft data." In: *Journal of Atmospheric and Oceanic Technology* 14.3, pp. 512–526. ISSN: 07390572. DOI: [10.1175/1520-0426\(1997\)014<0512:QCAFSP>2.0.CO;2](https://doi.org/10.1175/1520-0426(1997)014<0512:QCAFSP>2.0.CO;2).
- Vonk, J. E. et al. (2015). "Reviews and syntheses: Effects of permafrost thaw on Arctic aquatic ecosystems." In: *Biogeosciences* 12.23, pp. 7129–7167. ISSN: 17264189. DOI: [10.5194/bg-12-7129-2015](https://doi.org/10.5194/bg-12-7129-2015).
- Vrese, Philipp de, Lutz Beckebanze, Leonardo Galera, David Holl, Thomas Kleinen, Lars Kutzbach, Zoé Rehder, and Victor Brovkin (2022). *Higher Arctic CH<sub>4</sub> emissions under dry than under wet conditions? (In review)*.
- WRB, IUSS Working Group (2014). "International soil classification system for naming soils and creating legends for soil maps." In: *World Soil Resources Reports* 106, p. 2014.
- Walter Anthony, Katey M. and Peter Anthony (2013). "Constraining spatial variability of methane ebullition seeps in thermokarst lakes using point process models." In: *Journal of Geophysical Research: Biogeosciences* 118.3, pp. 1015–1034. ISSN: 21698961. DOI: [10.1002/jgrg.20087](https://doi.org/10.1002/jgrg.20087).
- Walter, K. M., S. A. Zimov, J. P. Chanton, D. Verbyla, and F. S. Chapin (2006). "Methane bubbling from Siberian thaw lakes as a positive feedback to climate warming." In: *Nature* 443.7107, pp. 71–75. ISSN: 14764687. DOI: [10.1038/nature05040](https://doi.org/10.1038/nature05040).
- Webb, E. K., G. I. Pearman, and R. Leuning (1980). "Correction of flux measurements for density effects due to heat and water vapour transfer." In: *Quarterly Journal of the Royal Meteorological Society* 106.447, pp. 85–100. ISSN: 1477870X. DOI: [10.1002/qj.49710644707](https://doi.org/10.1002/qj.49710644707).
- Wik, Martin, Ruth K. Varner, Katey Walter Anthony, Sally MacIntyre, and David Bastviken (2016). "Climate-sensitive northern lakes

- and ponds are critical components of methane release." In: *Nature Geoscience* 9.2, pp. 99–105. ISSN: 17520908. DOI: [10.1038/ngeo2578](https://doi.org/10.1038/ngeo2578).
- Wille, Christian, Lars Kutzbach, Torsten Sachs, Dirk Wagner, and Eva-Maria Pfeiffer (2008). "Methane emission from Siberian arctic polygonal tundra: eddy covariance measurements and modeling." In: *Global Change Biology* 14.6, pp. 1395–1408. DOI: [10.1111/j.1365-2486.2008.01586.x](https://doi.org/10.1111/j.1365-2486.2008.01586.x).
- Wong, George T.F. and Ching-Hui Hsu (1991). "The first apparent dissociation constant of carbonic acid in marine waters from 0 to 20‰ and 0 to 30 °C." In: *Estuarine, Coastal and Shelf Science* 32.3, pp. 257–265. ISSN: 0272-7714. DOI: [10.1016/0272-7714\(91\)90019-8](https://doi.org/10.1016/0272-7714(91)90019-8).
- Zhang, Hui, Sanna R. Piilo, Matthew J. Amesbury, Dan J. Charman, Angela V. Gallego-Sala, and Minna M. Väliranta (2018). "The role of climate change in regulating Arctic permafrost peatland hydrological and vegetation change over the last millennium." In: *Quaternary Science Reviews* 182, pp. 121–130. ISSN: 0277-3791. DOI: [10.1016/j.quascirev.2018.01.003](https://doi.org/10.1016/j.quascirev.2018.01.003).
- Zhang, Xiaowen, Jack A. Hutchings, Thomas S. Bianchi, Yina Liu, Ana R. Arellano, and Edward A.G. Schuur (2017). "Importance of lateral flux and its percolation depth on organic carbon export in Arctic tundra soil: Implications from a soil leaching experiment." In: *Journal of Geophysical Research: Biogeosciences* 122.4, pp. 796–810. ISSN: 21698961. DOI: [10.1002/2016JG003754](https://doi.org/10.1002/2016JG003754).
- Zubrzycki, S., L. Kutzbach, and E.-M. Pfeiffer (2014). "Permafrost-affected soils and their carbon pools with a focus on the Russian Arctic." In: *Solid Earth* 5.2, pp. 595–609. DOI: [10.5194/se-5-595-2014](https://doi.org/10.5194/se-5-595-2014).
- de Aro Galera, Leonardo, Tim Eckhardt, Christian Beer, Eva-Maria Pfeiffer, and Christian Knoblauch<sup>1</sup> (2022). *Ratio of in situ CO<sub>2</sub> to CH<sub>4</sub> production and its environmental controls in polygonal tundra soils of Samoylov Island, Northeastern Siberia (In review)*.



## COLOPHON

This document was typeset using the typographical look-and-feel classicthesis developed by André Miede and Ivo Pletikosić. The style was inspired by Robert Bringhurst's seminal book on typography "*The Elements of Typographic Style*".